UNIVERSIDAD **NACIONAL** DE COLOMBIA

Structure and Charge Transfer Processes at the Pt(111)/Solid Polymer Electrolyte Interface: A Mesoscopic Approach

Ana María Gómez Marín

Universidad Nacional de Colombia

Facultad de Minas

Departamento de Procesos y Energía

Medellín, Colombia

2014

Structure and Charge Transfer Processes at the Pt(111)/Solid Polymer Electrolyte Interface: A Mesoscopic Approach

Ana María Gómez Marín

Doctoral Thesis:

Doctorate in Engineering – Energetic Systems

Advisor:

Ph.D. Juan Pablo Hernández Ortíz

Universidad Nacional de Colombia

Facultad de Minas

Departamento Procesos y Energía

Medellín, Colombia

2014

A mi familia

Acknowledgements

Resumen

Los electrodos modificados son un área muy active en electroquímica, con muchas y variadas aplicaciones. Ellos son el componente central de numerosos dispositivos electrónicos, en los cuales usualmente el electrodo se encuentra recubierto por una delgada capa de una membrana, como en el caso de celdas de combustibles de intercambio protónico. Por lo tanto, entender la estructura y los procesos moleculares en las interfaces electrodo/membrana es un importante asunto para un desarrollo eficiente de estos aparatos. En este trabajo, se estudian electrodos de Pt(111) recubiertos con Nafion® y los resultados experimentales son explicados con base en dos aproximaciones teóricas. Inicialmente, la estructura y la dinámica de la interface se describen en términos del equilibrio ácido/base y la diferente movilidad de los grupos iónicos en la membrana. Luego, la cinética de reacción de una reacción electroquímica fundamental, como la oxidación de CO, es analizada con base en la segregación superficial inducida por la naturaleza bifásica de la membrana.

Los resultados muestran una interacción fuerte entre el electrodo y la membrana, que da origen a una orientación preferente de las regiones hidrofílicas del polímero, impulsada por el campo eléctrico. Aparentemente, la membrana induce un nuevo proceso de transferencia de carga, dependiente del pH, alrededor de 0.5 V en el voltamograma cíclico (CV). Sin embargo, la carencia de un corrimiento al azul en la longitud de onda de los grupos sulfónicos de la membrana, protonados o no, sugiere que estos aniones no están adsorbidos específicamente, sino acumulados en la doble capa. Análogamente, el modelo propuesto para la interface predice mínimos y máximos locales en la capacitancia, debido bien sea al cambio en la energía total de interacción de los iones que penetran en la membrana con el potencial aplicado, o a la disociación acido/base y la diferente movilidad iónica al interior de la membrana. El modelo propuesto amplia el marco conceptual para la interpretación de los CVs para estos sistemas y en general la teoría para las interfaces electrificadas. Adicionalmente, es una herramienta para la comprensión de la actividad electrocatalítica de electrodos modificados.

En general, la presencia de la membrana cerca al electrodo puede inhibir la transferencia electrónica de aquellas reacciones electroquímicas que dependen fuertemente de la estructura de la doble capa, bien porque bloquee sitios superficiales o por una menor caída de potencial en el plano externo de Helmholtz. Sin embargo, en algunos casos, la transferencia electrónica puede ser mejorada. Experimentalmente, el Nafion® bloquea la adsorción de hidrógeno y la disociación del agua, probablemente porque una fracción de la superficie está recubierta con regiones hidrofóbicas del polímero. Adicionalmente, experimentos de despojamiento de CO revelan modificaciones en la estructura de la capa adsorbida y una menor velocidad de reacción, la cual ocurre en un pico de corriente más agudo y desplazado hacia potenciales más positivos que en electrodos no recubiertos. Simulaciones empleando la teoría de campo medio y Monte Carlo Dinámico sugieren que la membrana modifica las interacciones netas entre las moléculas

adsorbidas: CO, OH y agua, haciéndolas más atractivas. Por lo tanto, la presencia de la membrana promueve la segregación superficial y la formación de islas.

Palabras clave: Electrodos modificados, Membranas electrolíticas, Doble capa eléctrica, Interface Pt(111)/Nafion®, Oxidación de CO, Mecanismo Langmuir-Hinshelwood.

Abstract

Modified electrodes are a very active area of electrochemistry, with multiple and widespread uses. They are a central component in many electrochemical devices, in which usually a thin membrane covers the electrode, as in Proton Exchange Fuel cells. Thus, understanding the structure and molecular processes at electrode/membrane interfaces constitutes an important issue for an efficient development of these devices. In this work, Nafion® coated Pt(111) electrodes were studied and experimental results were explained in light of two different theoretical approaches. Initially, the structure and dynamics of the electrode/SPE interface was described in terms of the acid/base equilibrium and the different mobility of membrane ionic groups. Later, the reaction kinetics of a fundamental electrochemical surface reaction, such as the CO oxidation, was analyzed on basis of the effect of the adsorbed species segregation induced by the membrane's two-phase nature.

Results showed a strong interaction between Pt(111) and Nafion® membrane, giving rise to a preferential orientation, electric field driven, of polymer hydrophilic regions. The membrane apparently introduces a new charge transfer process, *pH*-dependent, around 0.50 V in the cyclic voltammogram (CV). However, the lack of a wavenumber blue-shift of both protonated and dissociated Nafion®'s sulfonic groups with increasing the electrode potential would suggest that sulfonate anions are not specifically adsorbed but populate the double layer (DL). In agreement, proposed model predicts local maxima and minima in the capacitance, as consequence of either the change in the total interaction energy experienced by an ion inside the membrane with the applied potential or the acid/base dissociation process and the different ion mobility inside the membrane. The model extends the conceptual framework for the interpretation of CVs for these systems and the general theory for electrified interfaces. Additionally, it provides a tool towards the understanding of the electrocatalytic activity on modified electrodes.

In general, the membrane close to the electrode surface may inhibit the electron transfer rate (ETR) of electrochemical reactions that strongly depend on the structure of the DL, well because blocks surface sites or because of the smaller potential drop at the Outer Helmholtz Plane. However, in some cases, the ETR can be enhanced. Experimentally, hydrogen and OH adsorption/desorption regions on Nafion® coated electrodes are significantly blocked, probably because a fraction of the Pt(111) surface is covered by the membrane backbone and becomes electrochemically inactive. Additionally, CO stripping experiments revealed a modification on the CO-adlayer structure and a slower reaction rate, which occurs in a sharper peak, and shifted to higher potential values, than on bare Pt(111) electrodes. Mean Field Approximate theory and Dynamic Monte Carlo Simulations suggest that Nafion® membrane modifies the "*effective*" interactions between adsorbed molecules: CO_{ads}, OH_{ads} and water, turning them into a more "attractive" character than in the case of a bare electrode and so, promoting surface segregation.

Keywords: Modified electrodes, Solid Polymer Electrolyte Membranes, Electrical double layer, Pt(111)/Nafion® Interface, CO oxidation, Langmuir-Hinshelwood mechanism.

Table of Contents

List of Figures

List of Tables

Abbreviation List

Latin symbols

Symbol	Name	SI units
$a(x)_i^{\alpha}$	Activity of species i, in medium α, at a distance x from the electrode surface	
$C_0(0, t)$	Concentration of the reacting species outside the diffuse layer	$\dfrac{mol}{m^3}$
$c(x)_i^M \Delta X$	Surface concentrations per plane	$\dfrac{mol}{m^2}$
C	Capacitance	$\dfrac{\mu F}{cm^2}$
d_{OHP}	Distance of the OHP	m
D	Rate of surface diffusion	s^{-1}
e	Charge of an electron	C
$E[i\text{-}\Delta X, i]$	Electric field between planes i and i-1	
$E^{0'}$	Reaction formal potential	V
$E_{p, CO/OH}$	CO oxidation peak potential	V
E_a	Activation energy	$\dfrac{kJ}{mol}$
$E_{p,OH}$	OH adsorption/desorption peak potential	V
E_f	Final step potential	V
F	Faraday´s constant	$\dfrac{C}{mol}$
$f(x)$	Fraction of ionizable groups which are dissociate per plane	
$f_i(\theta)$	Function to describe the variation of the heat of adsorption of the species with the total coverage	
I	Current density	$\dfrac{\mu A}{cm^2}$
i_{max}	Maximum current	$\dfrac{\mu A}{cm^2}$
Ka	Membrane acid dissociation constant in absence of an interfacial electric field	mol^{-1}
k_B	Boltzmann´s constant	$\dfrac{J}{K}$
k_0	Standard rate constant	s^{-1}
k_1^0	OH adsorption reaction rate constant at low-coverage limit	s^{-1}
k_{-1}^0	OH desorption reaction rate constant at low-coverage limit	s^{-1}
k_2^0	OH oxidation reaction rate constant at low-coverage limit	s^{-1}
k_2	CO oxidation reaction constant	s^{-1}
M	Uniform density of ionizable acid/base membrane groups	$\dfrac{mol}{m^3}$
n	Electrolyte solution of concentration	$\dfrac{mol}{m^3}$
R	Universal gas constant	$\dfrac{J}{K\,mol}$
r_i	Stokes radius of specie i	m
r_p	Characteristic pore size	m

Symbol	Name	SI units
r_{ionic}	Ionic radius of the ion i	m
T	Absolute temperature	K
t_{max}	Current maximum time	s
v	Scan rate	$\frac{V}{s^1}$
v_j	Rate of the j-th reaction	$\frac{cm^2}{s^1}$
x	Distance from the electrode surface	m
z	Ion valence	
ΔX	Lattice plane separation	m
$\Delta W_i(x)^M$	Interaction free energy, including all interactions of the ion with the medium.	$\frac{kJ}{mol}$
$\Delta W_{Ion-solvent}^M(x)$	Change in the ion-solvent interactions	$\frac{kJ}{mol}$
$\Delta W_{Ion-dipole}^M(x)$	Change in the ion-dipole interactions	$\frac{kJ}{mol}$
$\Delta W_{Neutral}^M(x)$	Change in other contributions to the free energy, i.e. hydrophobic and Van der Waals interactions, steric exclusion.	$\frac{kJ}{mol}$

Greek symbols

Symbol	Name	SI Unit
α_i	Global transfer coefficient for reaction i	
$\sigma(x)$	Charge density	$\frac{\mu A}{m^2}$
β_i	Symmetry factor for electron-transfer reactions	
γ_i	Brønsted factor for the reaction i	
ε	Dielectric constant	
λ	Number of water molecules per sulfonic acid group	
θ_i	Average coverage of the species i	
$\epsilon_{i/j}$	Interaction energy between molecule *i* and molecule *j* when they occupy neighboring sites on the surface	
Γ_s	Number of surface sites per cm^2	
ϵ_{CO-CO}	"*Effective*" lateral interactions	
δ	Membrane thickness	M
μ	Ionic strength	
μ_i^0	Standard chemical potential of species i	
$\bar{\mu}_i^\alpha(x)$	Electrochemical potential of species i in medium α, at a distance x from the electrode surface	
κ	Debye–Hückel parameter	m^{-1}
$\gamma(x)_i^\alpha$	Activity coefficient of species i, in medium α, at a distance x from the electrode surface	
φ_i	Steric partitioning coefficient for ion i.	
$\phi(x)^\alpha$	Local electrostatic potential at x in medium α.	V

Subindex

Subindex	Name
ads	adsorbed
E	Electrode

Subindex	Name
EQ	Equilibrium
M	Membrane
P	Membrane pore
S	Solution
UPD	Underpotential deposition
W	Water
+	Positive charges
-	Negative charges

Abbreviation list

Abbreviation	Name
ATM	Atomic Force Microscopy
ATR	Attenuated Total Reflection
BFT	Bewick, Fleischmann and Thirsk
CL	Catalyst Layers
CV	Cyclic Voltammogram
DAFC	Direct Alcohol Fuel Cell
DFT	Density Functional Theory
DL	Double Layer
DMC	Dynamic Monte Carlo
DMCS	Dynamic Monte Carlo Simulations
EC–NMR	Electrochemical Nuclear Magnetic Resonance
ECR	Electrochemical Reactions
EDL	Electrical Double Layer
EIS	Electrochemical Impedance Spectroscopy
ER	Eley–Rideal
ET	Electron Transfer
ETR	Electron Transfer Rate
FTIR	Fourier Transform Infrared
FTIR–ERS	Fourier Transform InfraRed External Reflection
FTIRS	Fourier Transform Infrared Spectroscopy
FWHM	Full–Width Half–Maximum
GCS	Gouy-Chapman-Stern
HMRE	Hanging Meniscus Rotating Electrode
IHP	Inner Helmholtz Plane
IPD	Interfacial Potential Distribution
IR	Infrared
IRRAS	InfraRed Reflection Absorption Spectroscopy
LEED	Low Energy Electron Diffraction
LB	Langmuir–Blodgett
LH	Langmuir–Hinshelwood
MEA	Membrane Electrode Assembly
MFA	Mean Field Approximation
ML	Monolayer
MC	Monte Carlo
MS	Mott-Schottky
N&G	Nucleation and Growth
nn	Nearest Neighbour

NSTF	Nanostructured Thin-Film
OHP	Outer Helmholtz Plane
ORR	Oxygen Reduction Reaction
PEFC	Proton Electrolyte Fuel Cell
PFA	Perfluoroalkyl
PFSA	Perfluorosulfonic Acid
PFSI	Perfluorosulfonated Ionomer
PEM	Proton Electrolyte Membrane
PEMFC	Proton Electrolyte Membrane Fuel Cell
PTFE	Poly-Tetrafluoroethylene
PZC	Potential of Zero Charge
PZTC	Potential of Zero Total Charge
RDS	Rate Determining Step
RHE	Reversible Hydrogen Electrode
RT	Room Temperature
SAM	Self–Assembled Monolayers
SEIRAS	Surface-Enhanced Infrared Absorption Spectroscopy
SERS	Surface Enhanced Raman Scattering Spectroscopy
SHG	Óptical Second Harmonic Generation
SNIFTIRS	Subtractively Normalized Interfacial Fourier Transform Infrared Reflection Spectroscopy
SPE	Solid Polymer Electrolyte
SPEM	Solid Polymer Electrolyte Membrane
STM	Scanning Tunneling Microscopy
SV	Stripping Voltammogram
TFMSA	Trifluoromethanesulfonic Acid
TPD	Temperature Programmed Desorption
UHV	Ultra High Vacuum

Introduction

Modification of electrode surfaces by coating them with a film of a selected chemical moiety to introduce desired physical, chemical, electrochemical and/or optical properties to the unmodified substrate is a very active area of electrochemistry in recent years [1,2]. The film can be an irreversible adsorbed, or covalent attached, monomolecular layer, a polymeric, or inorganic, multilayer coating or a spatially defined, molecularly heterogeneous layer. Therefore, it is important to distinguish between physical adsorption, where the film is attracted to the surface via electrostatic or non–electrostatic interactions, and chemical adsorption, where a part of the molecule is chemically bound (grafted) to the surface [3].

Modified electrodes are a relatively modern approach in electrode systems, very useful in a wide spectrum of electrochemical investigations, including the relation of heterogeneous electron transfer and chemical reactivity and electrostatic phenomena at electrode surfaces [1]. They can also be employed in the design of electrochemical devices and systems for applications, such as electrochromic, molecular electronic, active display, energy conversion and storage devices, analytical sensors, reference electrodes, or to protect the underlying substrate from corrosion or chemical attack [1]. In addition, they have been used to characterize electron-, ion- and mass-transfer processes in polymers and other materials, giving insights into how surface structures can be designed to carry out specified reactions or processes [1,4].

Specifically, electrodes coated with proton conducting ionomers are widely used in many electrochemical applications where selective separation of ion fluxes is required, including fuel-cell devices [5–8], flow batteries [9], solar-fuels generators [9], wastewater treatment equipment [10,11] and electrochemical sensors [1,12,13]. Ionomers are solid polymer electrolytes (SPE), *i.e.* copolymers of hydrophobic repeat units with a fraction of monomer units with ionic groups, such as SO_3^-, CO_2^-, PO_3^-, attached to the polymer backbone [3,4,8,14]. Thus, in contact with electrolyte solutions these membranes may acquire a fixed electric charge [15,16]. This hydrophilic/hydrophobic nature makes hydrated ionomers basically a two-phase system on the scale about 4 to 10 nm in diameter [8,14,17,18], with unique physical and morphological properties [8,17–19].

In most of applications, a thin SPE layer usually covers the metal electrode and so, the understanding of the electrical, compositional and structural aspects of the electrode/SPE interface is an essential step toward an optimum design and an overall successful performance of these thin solid state devices [20]. Among these, polymer electrolyte fuel cells (PEFCs) have attracted much interest as one of the most promising technologies for an efficient, non-polluting energy source for transportation and stationary electric powers in urban environments [5,6]. In such applications, a higher performance, such as high current density and quick response of fuel cells, has to be accomplished [21]. The central component of PEFCs is the membrane electrode assembly (MEA), which consists of a cathodic and an anodic catalyst layers (CLs) separated by a proton exchange membrane

(PEM) that permits proton conduction while preventing electron conduction [6,22]. In the CLs, highly disperse catalysts, usually Pt or Pt alloy nanoparticles, are deposited on high-surface-area carbon and impregnated with a 5 to 100 nm thin film of perfluorosulfonated ionomer (PFSI) [5,6,22,23].

Poly(perfluorosulfonic acid)-based ion-conducting membranes are the standard material for chlor-alkali electrochemical cells, PEFC and other electrochemical devices, because of their hydrophilicity, selective permeability to cations, low resistance to current flow, and excellent thermal and chemical stability [5,6,8,14,18,19]. Among them, Nafion®, a DuPont registered trademark polymer, is the most widely used material as both PFSI and PEM because of its remarkable proton conductivity and stability [8,18]. In consequence, extensive work has been undertaken to understand how the structural features of Nafion® influence the material properties of the membrane [8,14,18,24], which in turn affects the electron and mass transfer kinetics of electrochemical reactions on Nafion®-coated electrodes [21,25–43]. However, study of such interactions is challenging and detailed understanding at the molecular level of the Nafion®/electrode interfacial structure remains elusive [22]. This is, in part, due to the complicated nature of the interface: there are perfluorocarbon backbones and sulfonate terminated perfluoroalkyl (PFA) ether side chains of the ionomers, as well as reactant, intermediate and product species.

Since fuel cell reactions occur on the catalyst surfaces, the ionomer plays a critical role to shuttle protons within the electrodes. Additionally, catalytic reactions at surfaces are known to be very sensitive to the nanoscale and atomic level structure of the heterogeneous interface at which they take place [44–52]. Therefore, understanding Nafion®/catalyst interfacial structure is of paramount importance for clarifying electrode reaction mechanisms, maximizing the catalysts utilization to significantly reduce the Pt loading and improving PEFC performance and durability, which are overarching challenges in fuel cell development and deployment.

Scope of this Thesis

Understanding the structure and molecular processes at electrode/membrane interfaces constitutes an important topic in PEFC as well as in electrochemistry [20]. In this sense, the general objective of this thesis was to develop a mesoscopic description of the electrode/SPE interface, from a theoretical and experimental point of view, in order to shed some light on the electrical, compositional and structural characteristics of this interface and on how the presence of the membrane can modify the charge transfer processes taking place on it. Within this goal, Nafion® coated Pt(111) electrodes were studied (Chapter 1), and the experimental results were explained in light of two different theoretical approaches. In the first one (Chapters 2 and 3), the structure and dynamics of the electrode/SPE interface, *i.e.* the formation of the electrical double layer (EDL), was attempted, in terms of the acid/base equilibrium and the different mobility of membrane ionic groups. The second approach was to analyze the reaction kinetics of a fundamental electrochemical surface reaction, such as the CO oxidation, on basis of the effect of the adsorbed species segregation induced by the membrane's two-phase nature (Chapters 4 and 5). In next paragraphs, a brief outline of this thesis will be given.

Although the interface between platinum polycrystalline electrodes and Nafion® films has been extensively studied [21,25–43], use of a well-defined Pt electrode is essential to understand the interfacial processes at an atomic scale. In Chapter 1, the Pt(111)/Nafion® interface in $HClO_4$ acid solutions was studied by cyclic voltammetry and

InfraRed Reflection Absorption Spectroscopy (IRRAS). The Pt(111) electrode was chosen because it is believed that (111) orientation is the most abundant facet in Pt nanoparticles and PEMFC electrocatalysts [53–57], which is based on the theoretical assumption of the cube-octahedral shape as the most energetically stable surface [58,59]. Special attention was devoted to membrane structural changes in contact with the platinum surface with the applied potential. Furthermore, the performance of the Pt(111)/Nafion® in a typical electrochemical reaction, as CO oxidation, was also analyzed. Notable differences in the adsorption and oxidation characteristics of CO on a bare and Nafion® covered Pt(111) electrode were found.

In Chapter 2, a model for the differential capacitance of electrodes coated by SPE membranes in contact with an electrolyte solution is proposed, in which the membrane contains acid/base groups attached to its polymer backbone. The model includes both a thermodynamic treatment of the acid/base equilibrium between charged groups inside the ionomer and a discrete description of the charge position, taking into account the different mobility of polymeric ionic groups and counterions inside the membrane. Results are discussed in light of the electron transfer rate on membrane-coated electrodes for those electrochemical reactions that strongly depend on the double layer structure. It is shown that, in absence of specific adsorption of polymeric anions to the electrode surface, an asymmetrical maximum in the current–potential curves may appear. This asymmetric response is a consequence of changes in the fraction of ionizable groups, due to changes in solution conditions and the applied electrode potential

The Chapter 3 contains an extension of the model discussed in Chapter 2. Here, the change in the C_T–E profile when coions from the solvent phase penetrate into the membrane and considering the ion separation at the SPEM/solution interface as a function not only of the Donnan equilibrium, but also the steric hindrance and dielectric exclusion is included. The dielectric exclusion is expressed in terms of (*i*) the solvation energy change that ions experiences when moving from the aqueous environment to membrane pores [60], and (*ii*) the interaction between ions and polarization charges, induced by the ions themselves, at the dielectric boundary between the pore walls and the pore-filling solution [15,61–64]. It is shown that capacitance maxima may appear not only due to the acid/base dissociation process inside the membrane, but also because of the change in the total interaction energy with the applied potential. At the end of this chapter, the predictions of this physically more realistic model are discussed in light of experimental data obtained at Nafion® covered Pt(111) electrodes [65–70], providing a theoretical basis for a qualitative electroanalyses of these systems.

Regarding the electron transfer on the metal/SPE interface, the Chapter 4 presents a model for the electrocatalytic oxidation of CO on metal surfaces inside the framework of the Mean Field Approximation (MFA). The model includes attractive and repulsive "*effective*" lateral interactions between the species, to represent the effect of the surface segregation, induced by membrane's phase separation, in the electrochemical reaction. A Langmuir–Hinshelwood (LH) mechanism between adsorbed CO, CO_{ads}, and adsorbed OH, OH_{ads} [71,72], resulting from previous water dissociation, is used. Simulated results suggest alternative explanations to experimental observations during CO stripping oxidation on different electrodes by potential step chronoamperometry or voltammetry. Although the model ignores higher order interactions, like three–body and long-range interactions, results are useful for a qualitative understanding of the CO oxidation kinetics and other electrochemical LH reactions.

Under the MFA, the surface is still considered homogeneous. In consequence, average lateral interactions and infinite diffusion rates are considered [73]. Hence, the effect of repulsive/attractive short range interactions is overestimated/underestimated depending on the process takes place. In addition, adsorbate-adsorbate correlations are not properly described. In Chapter 5, the model in Chapter 4 is solved through Dynamic Monte Carlo (DMC) simulations, in order to underscore the importance of the molecular distribution of the reaction partners and their surface mobility on the potential dependence of the rate constant of CO oxidation in an accurate way. This DMC model fully incorporates the nearest neighbour (*nn*) lateral interactions and the correct time dependence of the rate constants [74]. The results obtained are considered useful for an improved qualitative understanding of the kinetics of CO oxidation and in the general theory for other electrochemical LH reactions. All DMC simulations were carried out with the program CARLOS [75,76]. This is a general-purpose program for DMC simulations of surface reactions [74,75,76].

Finally, in Chapter 6 the major conclusions of the results obtained in the development of this thesis are drawn.

1. Spectroelectrochemical Studies of the Pt(111)/Nafion® Interface Cast Electrode[1]

Understanding the structure and molecular processes at the electrode/membrane interfaces constitutes an important topic in PEFC as well as in electrochemistry. In this work, the Pt(111)/Nafion® model interface in $HClO_4$ acid solutions is studied by IRRAS and cyclic voltammetry. It was found that the presence of an electric field mainly promotes deprotonation of sulfonic groups and structuring of water inside the membrane (polar molecules), especially near the electrode surface, with a sudden change of system optical properties at the Pt(111)/membrane interface at 0.9 V, possibly due to clustering within the polymer. Furthermore, the performance of the Pt(111)/Nafion® in a typical electrochemical reaction as CO oxidation has been also analyzed. It is showed that there are notable differences between the characteristics of CO adsorption and oxidation at Pt(111) with and without polymer electrolyte membrane, like a continual wavenumber increase with the potential for the on top CO band, even during CO oxidation which proceeds at higher potentials at the electrode covered by the polymer. The spectroscopic features suggest enhanced proton mobility inside the membrane concomitantly with the deprotonation of sulfonic groups near the electrode surface and with higher potentials, possibly due to oriented morphologies inside the membrane induced by high fields.

1.1 Introduction

Polymer electrolyte fuel cells (PEFC) have attracted much interest as one of the most promising technologies for an efficient, non-polluting power source for vehicles in urban environments. The key element of PEFC is a solid (ionomeric) polymer electrolyte (SPE) which serves as proton conductor and as separator of the anodic and cathodic compartments in this cell. The membrane commonly employed in the most recent PEFC developments is based on Nafion®, a DuPont registered trademark polymer. As electrocatalyst, platinum is mainly utilized owing to its high electrocatalytic activity in acidic electrolyte environments. In consequence, understanding the structure and molecular processes at the electrode/membrane interfaces constitutes an important topic in PEFC as well as in electrochemistry [20].

From a chemical point of view, Nafion®, a perfluorosulfonic acid (PFSA) membrane, consists of a hydrophobic poly-tetrafluoroethylene (PTFE) backbone with fully perfluorinated ether side chains terminated by strongly hydrophilic $-SO_3H$ groups (Scheme 1.1). This structure leads to spontaneous phase segregation at the nano-

---

structural level. In fact, Nafion® can be depicted as a porous solid filled by water [77]. In hydrated membranes, the water content is usually stated in terms of the parameter λ, defined as the number of water molecules per sulfonic acid group. It is well accepted that in hydrated PFSA membranes sulfonic acid groups and water develop an interconnected proton conducting network when a threshold value of water content is reached ($\lambda \approx 2$), while the fluorocarbon backbone forms a semicrystalline hydrophobic phase [24].
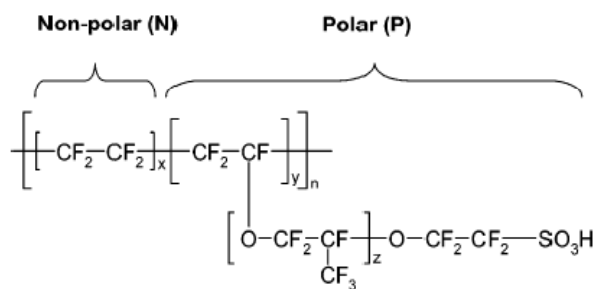
Scheme 1–1: Chemical structure of PFSA 1100 ($x = 7$ and $y = z = 1$). *N* indicates for the nonpolar monomeric units while P indicates the polar monomeric units [24].

The performance of SPE depends on the coordination of ion-exchange groups with water molecules. This coordination results in the formation of ionic channels, through which the mobility of negatively charged ions is dramatically decreased and the transport of positively charged ions (protons) is selectively allowed. Additionally, SPE slows down the rate of diffusion for uncharged species, such as methanol and CO_2 molecules. This phenomenon plays an important role in Direct Alcohol Fuel Cell (DAFC) minimizing the so-called crossover effect [78]. Since the membrane transport properties depend on temperature and hydration level [79], the interaction between water and Nafion® has been extensively investigated with the help of Fourier Transform Infrared Spectroscopy (FTIRS) [17,80–90].

In contrast to the extensive studies of the bulk membrane properties, very little is known about the interaction of the membrane with Pt catalysts, an important question for the understanding of the performance of PEFC [78]. It has been recognized that due to the cellular Nafion® structure, electrochemical processes can take place only at domains where hydrophilic ionic clusters are in contact with the electrode surface [25,26]. The regions where the Pt surface is exposed to the fluorocarbon backbone are inactive. Consequently, when SPE is in contact with a solid electrode, the electrochemically active area is smaller than on the bare electrode exposed to a liquid electrolyte. In addition, although the modification of platinum electrochemistry caused by the presence of the Nafion® interface is obvious from the voltammograms showed in a number of papers, this aspect has not received significant attention [26–28].

It has been reported that Nafion® coating significantly enhances methanol electro-oxidation reaction [29], hydrogen anodic oxidation [25] and oxygen reduction reaction (ORR) [30–33]. In the latter cases, the increase has been attributed to higher O_2 and H_2 solubilities in recast Nafion® than those in aqueous solutions, which is mainly due to the presence of the hydrophobic fluorocarbon phase [31–33]. However, the detailed mechanism of these modifications is still under discussion. Other possible explanation could be a change in the catalyst properties by the membrane-electrode interactions. On the other hand, other studies have concluded that the presence of Nafion® does not

modify the kinetic parameters of ORR [34,35] or, by contrary, it has been found that Nafion®-coated Pt electrodes show lower apparent ORR activity and more H_2O_2 production than on bare Pt electrodes, indicating that sulfonate groups in Nafion® strongly adsorb on Pt sites and modify the surface properties [36,37]. These examples illustrate the need of gaining molecular level information related to the nature of the coordination of a Nafion® membrane to an electrode surface.

In the past, the structure of the Pt polycrystalline/Nafion® interface has been probed by different techniques [20,21,38,39,78]. Osawa *et al.* suggested that the electrochemical microenvironment within Nafion® can be investigated by *in situ* Infrared Reflection Absorption Spectroscopy (IRRAS) [38]. Kanamura *et al.* investigated it by attenuated total reflection (ATR) configuration but information about the potential dependent orientation of Nafion® chemical groups was not reported because the investigation was conducted in the absence of applied potentials [21]. Malevich *et al.* studied a cast Nafion® film on Pt polycrystalline by subtractively normalized interfacial Fourier transform infrared reflection spectroscopy (SNIFTIRS) in the IRRAS configuration, and it was demonstrated that sulfonic acid groups were coordinated to or displaced from the Pt surface depending on the applied potential [78]. Later, Malevich *et al.* investigated the effect of Nafion® on CO adsorption and electrooxidation at Pt nanoparticles and observed that a film of Nafion® slows down the CO oxidation reaction [39]. Finally, the interface has been characterized in $HClO_4$ aqueous solutions using surface-enhanced infrared absorption spectroscopy (SEIRAS) by Ayato *et al.* A potential dependent band was found around 1100 cm^{-1} and assigned to the symmetric vibration of the $-SO_3^-$ groups of the ionomer membrane, and the OH stretching band of non-hydrogen bounded water molecules associated with the Nafion® structure was observed for the first time at 3680 cm^{-1} [20].

Single crystal metal electrodes are often used to characterize electrochemical processes. The rationale behind this is the possibility of establishing a correlation between interfacial properties (*i.e.* the geometry of the surface, the nature and structure of the adsorbing species) and the electrochemical process occurring on it (*i.e.* rate of charge transfer, structure of double layer). With this objective, Subbaraman *et al.* used a voltammetric approach to probe the nature of Pt/Nafion® three phase interfaces for Pt(*hkl*) and polycrystalline platinum surfaces. In that work, they suggested, via CO charge displacement measurements, that sulfonate anions adsorb on the Pt electrode surface [65]. Later, Subbaraman *et al.* studied the kinetics of the ORR at metal/Nafion® interfaces on a wide range of surfaces, ranging from Pt(*hkl*) single-crystal surfaces, Pt-poly, Pt-skin to high-surface-area nanostructured thin-film (NSTF) catalysts, and showed that the adsorption of sulfonate anions on these catalysts negatively impacts the rate of the ORR in perchloric but not in sulfuric acid solutions [66].

All these approaches provide some valuable information about the possible structure of the interface electrode/membrane. However, a great effort still needs to be done in order to obtain a molecular-level structural description of the three-phase interface. The use of well defined surface structures together with *In situ* Infrared Spectroscopy at electrochemical interfaces provides molecular data on adsorbed species under the influence of the electric field (*i.e.* the state of internal and external bonds, the lateral interactions within the adlayer). This information gives valuable information for a molecular picture of the electrochemical double-layer and contributes to an improved understanding of the physicochemical properties of electrified interfaces, which can be correlated with features in voltammograms through the potential and coverage dependence on the spectral parameters [91,92].

In this work, the Pt(111)/Nafion® interface in HClO$_4$ acid solutions is studied by IRRAS and cyclic voltammetry. Special attention has been devoted to the structural changes of the membrane in contact with the platinum surface with the applied potential. Furthermore, the performance of the Pt(111)/Nafion® in a typical electrochemical reaction as CO oxidation has been also analyzed. With these techniques, we showed that there are notable differences in the adsorption and oxidation characteristics of CO on a bare and covered Pt(111) electrode and that CO oxidation proceeds at higher potentials at the covered electrode.

The oxidation of carbon monoxide adlayers on single cristal platinum electrode surfaces is one of the most intensively studied systems, especially the case of the Pt(111) surface. The Pt(111)-CO system can be considered as a model system both in electrochemistry and in the solid-gas interface. The interest in the system arises both from the fundamental point of view of basic science, and because CO is the stable residue formed in the incomplete oxidation of fuels. In the case of electrochemical systems, it is easily formed as the product of dissociative adsorption of simple oxygenated molecules such as formic acid, methanol, ethylene glycol, etc [93].

1.2 Experimental

Pt(111) electrodes were prepared following the Clavilier method [94]. In all experiments, electrodes were annealed and subsequently cooled down in H$_2$ + Ar. gas atmosphere (99.999% –N50– Air Liquid in all gases used), protected with a droplet of ultrapure water (Purelab Ultra®, Elga – Vivendi) and then transferred to a conventional two-compartment cell. Platinum coil wire and reversible hydrogen electrode (RHE) were used as counter and reference electrodes, respectively. Aqueous solutions were prepared from perchloric acid (Merck suprapur), used as received without further purification (0.01, 0.1 and 1 M). The electrolyte was purged with argon in order to remove oxygen and a blanket of argon was kept over the solution during the experiments. Electrodes were assembled into a hanging meniscus rotating electrode (HMRE) holder. Experiments were carried out at room temperature, 22 ºC. The time stability of the voltammetric profiles was carefully checked.

For SPE deposition, a 5 % (w/w) in mixture of lower aliphatic alcohols and water solution of Nafion® (Aldrich) was diluted with ultra-pure water to a concentration of 1 % (w/w). The Nafion® solution was dropped and spread over the Pt(111) surface uniformly. The membrane was deposited by spin-coating procedure at 750 r.p.m in an Ar. atmosphere. Typical drying times ranged from 15 to 30 min. We did not measure the film thickness but it can be calculated from the concentration and the volume of Nafion® solution deposited on the electrode and by using a dry density of 1.5 g cm^{-3}. Typical variations in thicknesses correspond to about 0.88 – 1.7 µm (They were not measured and were calculated by using an apparent density for the Nafion® film). The Nafion® coated electrode was then cured at 135 ± 5 ºC for 1 h in order to evaporate the solvent and to improve the adhesion between the polymer film and the electrode [20,39,78].

Infrared spectroscopic experiments were performed in a Nicolet Magna 850 infrared spectrometer following the same experimental protocol used before [95]. *p* and *s*-polarized light were used in these experiments. For CO adsorption experiments, only *p*-polarized light was used. As in electrochemical experiments, the solution was purged with argon to remove oxygen and a platinum coil wire and a reversible hydrogen electrode (RHE) were used as counter and reference electrodes, respectively. A BaF$_2$ infrared

window was used in order to reach vibrational wavenumbers down to 900 cm^{-1}. The spectra were shown as the ratio $-log(R_{ES}/R_{ER})$, were R_{ES} and R_{ER} are the single beam spectra obtained at the sample and the reference potentials, respectively.

Carbon monoxide was adsorbed at 0.1 V by bubbling CO (99.997% –N47–) gas through the solution. The excess of dissolved CO was removed by purging with Ar. The characteristic hydrogen adsorption/desorption region was completely blocked by the adsorption of CO.

The reference potentials were set as +100mV for Pt(111)/Nafion® experiments and +900 mV for CO–Pt(111)/Nafion® experiments (CO was completely oxidized at that potential) and +100 mV for CO_2 (this potential is more negative than the onset potential of the oxidation of CO to CO_2).

1.3 Results and discussion

1.3.1 Pt(111)/Nafion® Interface

Cyclic voltammetry. Pt(111)/Nafion® interface was initially characterized with cyclic voltammetry. Nafion® film showed good stability and electrode adherence. The first CV recorded after inserting the electrode into the cell showed that Pt(111) surface was blocked. Figure 1-1 shows the CVs of Nafion®-free (0.1 M $HClO_4$) and Nafion®-covered Pt(111) (1, 0.1 and 0.01 M $HClO_4$) in different $HClO_4$ solutions after applying multiple potential cycles between 0.06–0.90 V and 0.06–1.2 V for several minutes (2–4 min.), as cleaning procedure. Up to 0.90 V, the electrode surface reaches a stationary condition, while a more positive upper potential limit slowly increases the active surface area, indicating a modification in the membrane distribution near the electrode surface due to changes in the metal-ionomer interactions. After repetitive cycling up to 1.2 V, surface defects grow on Nafion®-free and Nafion®-covered Pt(111) electrodes. In the next results presented, only potential cycles between 0.06–0.90 V were applied to the covered electrode as a cleaning procedure.

Actually, the state of the art of the different adsorption states of a well-ordered Pt(111) electrode in acidic solutions without anion specific adsorption, as perchloric or trifluoromethane sulfonic acid solutions [96,97], recognizes two zones that can be clearly distinguished (Fig. 1–1). At potentials below 0.40V, pseudocapacitive currents originated by hydrogen adsorption/desorption processes (denoted as underpotential deposition of hydrogen, $H^+ + e^-\ H_{UPD}$) are observed. At potential above 0.55 V, the pseudocapacitive current observed has been traditionally assigned to the water dissociative adsorption as OH species [97]. In the case of Nafion® coated Pt(111) (Fig. 1–1), these two zones are still differentiated, but they are modified quantitatively, specially at lower *pH* dissolutions: the hydrogen and OH adsorption/desorption regions are significantly blocked, probably because a fraction of the Pt(111) surface is covered by hydrophobic PTFE backbone and becomes electrochemically inactive [20,25,78].

Careful inspection of the CVs reveals a significant feature on the Nafion®-covered surfaces: a small, new pseudocapacitive process, relatively irreversible and *pH* dependent in the potential region between 0.45–0.55 V. This behavior could indicate specific interaction between the membrane and electrode surface, markedly visible at *pH*

= 2.0. This result contrast with the common consideration of Nafion® as a non-adsorbing electrolyte, widely accepted in the literature [25,27], but agrees with recent works of Subbaraman *et al.* on Pt(111) [65,66] and other works with polycrystalline Pt, which suggested strong adsorption of sulfonate groups in Nafion® on Pt sites [36,37,39].

Figure 1-1:   Cyclic voltammograms of bare Pt(111) electrode in Ar. saturated 0.1 M HClO$_4$ solution and Nafion®-covered Pt(111) electrodes in Ar. saturated 1, 0.1 and 0.01 M HClO$_4$ solutions at scan rate of 50 mV s^{-1}. Insets: detailed views of the new pseudocapacitive processes at 0.45–0.55 V at different *pH*s.
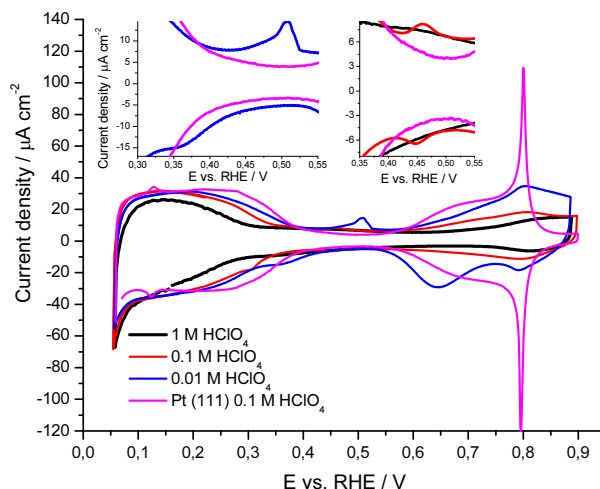
Apparently, the reversibility, peak position and the extent of the adsorption of the new charge transfer process are strongly *pH* dependents, however these results should be taken with caution: although the *pH* within the Nafion® coating should not be altered by changes in the solution *pH*, the measured peak potential may change in response to changes in the solution ionic strength, which in turn affects the Donnan potential [98,99] and Nafion® acidity [100]. Otherwise, in the absence of Donnan potential effects (*i.e.* high ionic strength of supporting electrolyte), process irreversibility could be due to different causes: the reduced mobility and the limited spacing between the anions arising from the structure of the ionomer membrane, similar to what was suggested by Subbaraman *et al.* [65], or by the development of an estable membrane morphology, induced by the electric field, which needs higher perturbations to come back to the "original" state [101,102].

In the same form, *pH* near the electrode surface should be lower than solution *pH*, considering Nafion® acidity [8,100,103,104], and CVs presented in Fig. 1–1 are slightly shifted to lower potential values. The extent of this shift also depends on the electrolyte *pH* and ionic strength, which modifies the cluster size, water structure and ion solvation inside the membrane [98–100]. Additionally, higher proton discharge currents during the negative-going scan could suggest an enhancement of this reaction at covered electrodes (Fig. 1–1). However, much more work is still necessary in order to clarify this point.

Experimentalists are familiar with the fact that the final structure of an ionomer membrane is dependent on the method by which it is prepared, and that the final form of the material is rarely the configuration with the lowest free energy. Boiling, rinsing, microwave drying, and other thermomechanical steps, as well as the manner of removing contaminants from the membrane, influence the membrane structure [101,102,105]. Results in Fig. 1–1

shows markedly contrast with the findings of Subbaraman *et al.*, who reported no hydrogen adsorption/desorption blockage and measured bigger charge transfer for the pseudocapacitive process [65]. Difference in membrane thickness and pretreatments could account for these discrepancies.

Additional experimental work about the electrochemical properties of this charge transfer process also showed that the electrochemical reversibility, peak potential and height, depends on the value of the lower potential limit of the CV (Figure 1-2) and the thickness of the film (coverage), as also was suggested by Subbaraman *et al.* [66]. Larger voltammetric peaks in thicker films are probably due to larger amounts of redox-active ions localized in the film even though their concentration is the same than in thin films. This is consistent with the dynamics of reversible couples in thin layer cells in which the peak current is directly proportional to volume. On the other hand, the upper limit of potential of the CV and the scan rate do not affect this process (Fig. 1–2).

Figure 1-2: Cyclic voltammograms for a Nafion® coated Pt(111) in Ar saturated 0.01 M $HClO_4$ solution at scan rate of 50 mV s^{-1} and different upper and lower cyclic voltammetric limits. Black and magenta: 0.06–0.90 V, red: 0.06–0.70 V and blue: 0.30–0.90 V. Black, red, blue and magenta follow the recording sequence of the CVs.
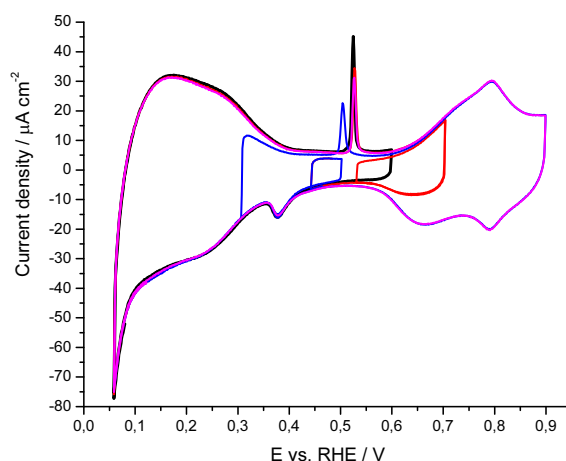
Attending to Nafion® chemical nature and that the peak potential is located in the same potential region where the adsorption of (bi)sulfate anions is observed in sulfuric acid solutions on Pt(111), the charge transfer process taking place between the membrane and the metal can tentatively assigned to the oxidative adsorption of sulfonate anion side chains, as it has been suggested in previous works [65,66,78]:

$$-SO_3H \longrightarrow -SO_3Pt + H^+ + 1e^-$$

(1.1)
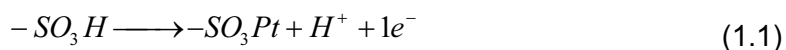
Analogue to (bi)sulfate adsorption/desorption on Pt(111), the peak potential position depends on SO_3^- anionic concentration and solution *pH*. Nevertheless, due to the complexity of interactions between membrane monomers, water molecules, protons and metal electrode, there are many metastable states separated by energy barriers in the equilibrated membrane and questions of how they affect the membrane morphology and the charge transfer at the metal/ionomer interface are not yet answered. Although a few works have provided some valuable information [20,21,25–39,65,66,78], a great effort still needs to be done in order to obtain a molecular-level structural description of the three-

phase interface and develop more detailed and complex models than the simple "spring model" proposed by Subbaraman *et al.* [65,66].

Because of side chains are terminated by $-SO_3H$ groups, Nafion® dramatically decreases the mobility of negatively charged ions through the membrane and eventually can suppress it. To gain further insight into the anion permeability, voltammetric modifications caused by the addition of sulfate anions at 10^{-3}, 10^{-2} and 10^{-1} M in a perchloric acid solution (0.01 M) have been recorded, Figure 1-3. Sulfuric acid was used as additive because sulfate anion adsorption on Pt(111) has a characteristic voltammetric response.

Figure 1-3:   Cyclic voltammograms for a Nafion® coated Pt(111) electrode in 0.01 M $HClO_4 + x$ M HSO_4^- (x = 0, 10^{-2} and 10^{-1} M) at 50 mV s^{-1}. For the sake of comparision the corresponding CVs on a bare Pt(111) electrode are given as inset.
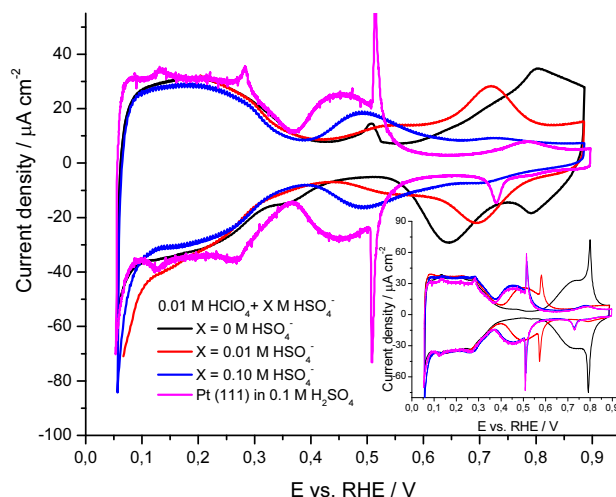
Fig. 1–3 shows that at low sulfate concentrations ($\sim 10^{-3}$ M) the membrane suppresses anion permeability while at higher concentrations the sulfate anions are able to reach the electrode surface. The exact concentration of anions diffusing into the membrane depends on the film thickness and the ionic strength of the solution, which determines the Donan potential at the interface between ionomer and the solution [98,99]. Apparently, sulfate adsorption suppresses Nafion® sulfonate adsorption. It appears that at 0.1 M the ionic strength of the solution is enough to compensate the Donnan potential effects, for common thicknesses employed in this work.

IR band assignment. The assignment of the vibrational bands of Nafion® was based on the already published data [17,80–90]. The fundamental vibrational modes of Nafion® appear below $\sim$1500 cm^{-1} and the frequencies of the vibrational modes corresponding to the $-SO_3^-$ group symmetry (*i.e.* on its environment) are expected in the 1100–1400 cm^{-1} range. Unfortunately, this IR wavenumber range is obscured by the intense CF_2 stretching vibrations and therefore it is difficult be make a precisely assignment [82,85,86,90].

Warren and McQuillan noted the importance of considering vibrational contributions from more than one functional group when assigning IR absorptions of fluoropolymers [90]. The consideration of mechanically coupled internal coordinates is essential for the analysis of IR spectra of ionomers and correlation of those spectra with the effects of ion exchange and state of hydration [89]. The main absorption bands and corresponding

assignments are listed in Table 1-1. It should be recognized that in a system such as that studied here, there is much mixing of the vibrational modes due to the similar masses and symmetry of the various components of the molecule, especially the COC, CF_2, and C-S groups. This mixing complicates spectral assignment based on an interpretive model centered on isolated local modes. Thus, the listed assignments are the dominant vibrational mode(s) that contribute to any given absorption [17,80–90].

Table 1-1:   Selected infrared absorption bands of H- Nafion® [17,80–90].

Band location (cm^{-1})	Assignment
970 m	C–O–C symmetric stretching, mechanically coupled to –HSO_3: v_s(C–O–C) which is sensitive to membrane hydration.
980 s	v_s(C–O–C) ether moiety close to the polymer backbone.
1060 s	Symmetric stretching of –SO_3^- groups, mechanically coupled to C–O–C: v_s(SO_3). Hydrogen bonded to H_2O molecules.
~1160 s	Asymmetric stretching of –CF_2 groups v_{as}(CF_2).
1200–1225 vs[a], br[b]	Mixed region CF/SO_3^-. CF_2 stretching, symmetric: v_s(CF_2). Anti-symmetric stretching modes of –CF_2, v_{as}(CF_2).
1130–1300 s	v_{as}(SO_3^-).
1300 sh	v_{as}(CF_3) .
1320 sh	Stretching mode v_s (S=O) of –SO_3^-.[15]
1430	Stretching mode v_{as} (S=O) of –SO_3H.[15]

[a] Relative intensity: vs, very strong; s, strong; m: medium; w: weak; sh: shoulder; v, V: very; b: broad.

[b] Band width: vbr, very broad.

The region above 1500 cm^{-1} is free of bands from the strong fundamental vibrational modes of the polymer. The rest of the bands in the region 4000–1500 cm^{-1} enable the observation of features attributed to permeating molecules (*i.e.* water vapor and other types of solvents), mainly to condensed water in the membrane [84,85]. It has been proposed that three types of water can exist: not hydrogen bonded, ~3715 cm^{-1}; partially hydrogen bonded, ~3660 cm^{-1}; and hydrogen bonded (either to another molecule of water or a sulfonate group), ~3520 cm^{-1}, Table 1-2 [17].

***In situ* IR reflection spectra.** Once the electrode was immersed in 0.1 M $HClO_4$ solution, p-polarized light spectra were recorded in order to determine the changes during membrane hydration processes. Figure 1-4 shows IRRAS spectra of Nafion® covered Pt(111) in deoxygenated 0.1 M $HClO_4$ solution at open circuit potential, as a function of the time elapsed since the electrode is put in contact with solution.

With increasing hydration different types of water inside membrane are observed: A bipolar band at 3068–3360 cm^{-1} suggests a wavenumber shift progressing into more bulk – like water OH stretching (3400 cm^{-1}). The intensity of this band increases with time, following the increase and sharpening of the band at 1650 cm^{-1}. This dynamics can be associated with the phase separation due to membrane swelling because of membrane

hydration (increase of the hydrophilic region). In addition, the band intensity increase at 3880 cm^{-1} and 3630 cm^{-1} implies an increase of population of "free" and partially hydrogen bonded water due to the water intercalation into the polymer backbone and the subsequent growth in the interfacial region. Alike movements have been obtained from different polymer hydration studies [84,85] and the experimental time dependent absorbance was fit by a pore diffusion model, consistent with proposed structures of Nafion® as consisting of network of hydrophilic pores and channels [85].

Table 1-2:   Selected infrared absorption bands of water inside H- Nafion® [17,80–90].

Band location (cm^{-1})	Assignment
~1625–1635	Close in energy to the bending mode of bulk water (1645 cm^{-1}) and is typically observed somewhat below in IR spectra of hydrated, metal cation exchanged Nafion® materials.
~1735	Characteristic of solvated proton structures, $(H_2O)_nH^+$. It has been assigned to asymmetric H-O-H bending modes of solvated H_3O^+ species.
~3080	H_2O strong bound. (Ice like structure).
~3520	Water which forms hydrogen bonds, either to another molecule of water or to a sulfonate group from Nafion®, the strength of which are significantly weaker than that of the hydrogen bonds in pure water.
~3660	Partially hydrogen bonded: water which is partially bounded to fluorocarbon and has one proton available for hydrogen bonding.
~3715	Non hydrogen bonded water: water with both protons surrounded by fluorocarbons not forming any hydrogen bonds, oriented in a manner that extends both hydrogen atoms toward fluorocarbon regions of the polymer or possibly at the interface of water and air-filled voids in pores and channels of the polymer.

Figure 1-4:   IRRAS spectra for a thin Nafion® film cast at a Pt(111) electrode at open circuit potential *vs.* hydration time. The reference spectrum was set the corresponding to *t* = 0 s. In the inset it is included the spectral region up to 3600 cm^{-1} in order to show the OH stretching potential-dependent behavior.
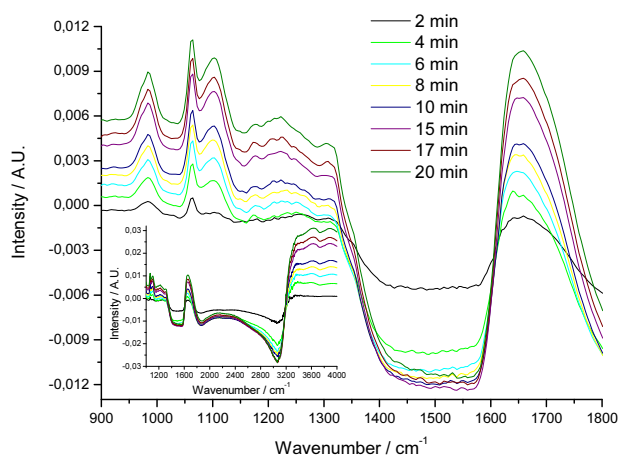
Concomitantly to water uptake, the increase of the bands at 986, with the shoulder at 970, and 1170 cm^{-1} and the 1200–1300 cm^{-1} region, directly associated with the polymer backbone (Table 1-1), points towards global membrane reorganization. Similar trends have been reported from time resolved spectral measurements for membrane hydration with Na$^+$ –exchanged Nafion® [85] The rapid uptake of water precluded similar studies into H$^+$ –exchanged Nafion® [85]. In the former case, least squares modeling was applied to gain insight into changes that occur in the structure of polymer membrane during hydration with an excellent match for bands of the CF$_2$ and C–O–C groups modes, but agreement was not as close for bands arising from modes of the hydrophilic –SO$_3^-$ and water [86]. No further efforts were tried in order to fit similar model in our case.

The growth of bands at 1060 cm^{-1} and 1320 cm^{-1} with time indicates that the sulfonate groups shift to a deprotonation state –SO$_3^-$ and are mainly dissociated at the equilibrium. Conversely to the reported, the intensity of these bands is bigger than similar bands from the spectral response either during polymer hydration studies without the electrode surface [84–86] or for a Nafion® film cast at the Pt polycrystalline electrode [78], which suggest a strongest interaction between –SO$_3^-$ ions and the Pt(111) surface.

Finally, the band at 1100 cm^{-1} is assigned to ClO$_4^-$ ion inside the membrane, as a result of permeation from the supporting electrolyte. With the exception of the band at 3068–3360 cm^{-1}, the wavenumber of the other bands is very little affected by the hydration time.

1.3.2 Influence of the potential on Nafion® membrane

Once full membrane hydration is reached, cyclic voltammetric sweeps were performed between 0.1 and 0.9 V at a scan rate of 2 mV s^{-1}, to study membrane changes with the applied potential either at the interface polymer/Pt(111) as well as in the bulk of the membrane. Figure 1-5 shows the IRRAS spectra for Nafion® covered Pt(111) in 0.1 M HClO$_4$, every 100 mV, taking as reference potential the initial spectrum at 0.1 V. The absence of characteristic bands due to bulk water at 3400 and 1645 cm^{-1} implies that the signals from the bulk solution were successfully cancelled out by the polymer.

Figure 1-5:   IRRAS spectra for a thin Nafion® film cast at a Pt(111) electrode. The reference spectrum was taken at 0.1 V (RHE). Potential sweep rate 2 mV s^{-1}. Left: *p*-polarized light. Right: *s*-polarized light. Inset includes the spectral region up to 3600 cm^{-1} in order to show the OH stretching potential-dependent dynamics.
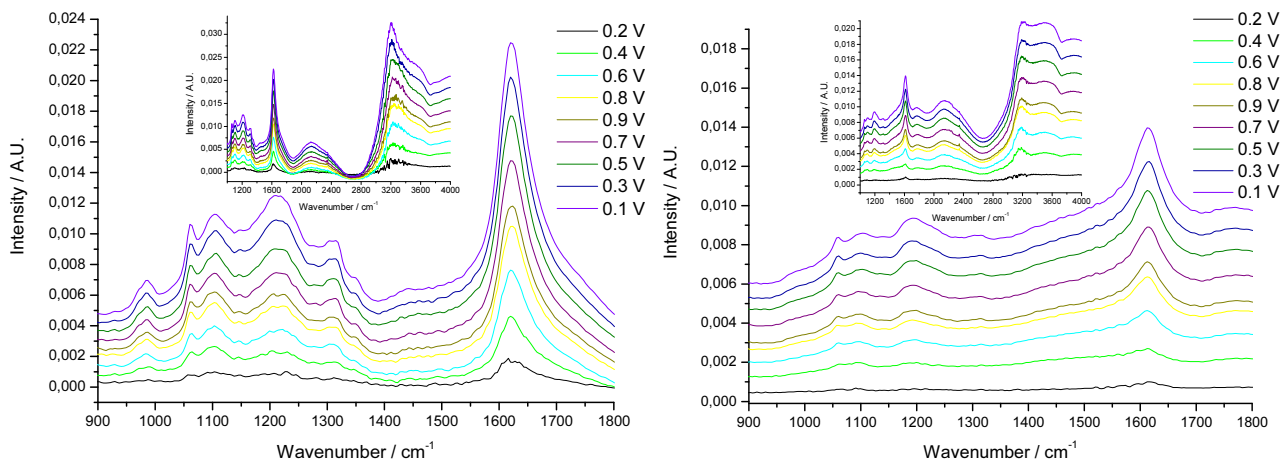
As can be observed from Fig. 1–5 the presence of an electric field mainly affects the water distribution and sulfonic groups inside the membrane (polar molecules) and promotes the perchlorate anion permeation. In addition, the wavenumber of the bands in the spectra collected either with *p*-polarized or *s*-polarized light is not too much influenced by the potential (*e.g.* there is no observable Stark effect).

The changes in the membrane with the potential are very slow: reversing the potential sweep direction does not affect significantly the trends of the membrane absorption changes. This fact suggests the development of quasi-irreversible metastable states induced by the electrode potential at the interface at room temperature, as was recently proposed from molecular simulations [101,102]. As was mentioned before, in systems as complex as humid ionomers, it is not unexpected that there should be several different structures that each represent a local minimum in the free energy and that the barriers to transitions between these morphologies should be much larger than available thermal energies [101,102]. Applied perturbations such as the external field in our study or raising the membrane temperature [106,107], are able to drive the system to states with lower energies and internal stresses in the backbone membrane.

Absorbance in the vicinity of 2360 cm^{-1} is believed to arise from overtones of polymer skeletal modes and low wavenumber vibrations associated with O–H groups [85]. Above ~0.7 V during the anodic sweep, a band at 2344 cm^{-1}, related to CO_2, starts to be detected and its intensity follows the potential sweep, decreasing during the negative-going sweep down to ~0.7 V. The formation of CO_2 can be originated as a product of the oxidation of solution impurities from the cast film or, more likely, to incipient membrane degradation with the potential. More work is necessary to clarify this point.

In particular, the applied potential has a direct effect on the structure and size of the hydrophilic ion cluster region of the membrane that can be understood following the changes in the water absorption bands, as it has already been reported [38]. The number of water molecules playing a role in the hydrogen bonding network inside the membrane, but weaker than in bulk water, increases, while the concentration of isolated ("free") water (3720 cm^{-1}) decreases with the potential. This suggests a growth in the hydrated ion cluster region in addition to changes that may occur in the environment for water surrounding ionic groups within the polymer and decreased area for water/polymer fluorocarbon region interface and explains the increase in the active surface area during successive CVs up to 1.2 V.

On the other hand, the appearance of a sharp band at 3180–3200 cm^{-1}, characteristic of very strong hydrogen bonded water molecules like those in the ice-network structure [91], and the feature near 1650 cm^{-1} (at open circuit potential), close in energy to the bending mode of bulk water (1645 cm^{-1}), shifted downward to 1620 cm^{-1} imply stronger interactions between water molecules and the electrode surface on the Pt(111)/Nafion® interface at higher potentials, probably because the hydrogen-bond water network inside the membrane is weaker than in bulk liquid water. The lower energy mode compared to bulk water has been discussed in terms of water adsorbed on the electrode surface with an electron lone pair [108] or weakening in the hydrogen bonding network caused by interactions of water molecules with sulfonate ions in Nafion® [85]. Hence, it seems that both stronger water/metal interactions and sulfonate adsorption may lead to the OH adsorption to be shifted to more positive potentials on the CVs recorded with Nafion® covered electrodes.

In a similar way, a broad band at 1780 cm^{-1}, generally assigned to H–O–H bending modes of solvated H$_3$O$^+$ species, starts to increase in intensity at more positive potentials, possibly due to oriented structures inside the membrane induced by high external electric fields as has been reported before [101,102]. This points out enhanced proton mobility inside the membrane concomitantly with the deprotonation of sulfonic groups, *i.e.* an increase in the proton conductivity and membrane acidity, like also has been found in previous works on stretched membranes and on Nafion® poling experiments [106,107]. This phenomenon originates from the various forces acting upon the membrane and could be the origin of major H$_2$O$_2$ formation during the ORR in presence of Nafion®, due to lower *pH*s raise H$_2$O$_2$ production, as previously has been reported [30,36,109].

In order to elucidate the functional groups directly interacting with the electrode surface, *p*-polarized and *s*-polarized light infrared experiments were compared. Strong water movements near the Pt(111)/Nafion® interface are testified by the growth in intensity of the band at 3200 cm^{-1} in the spectra recorded with *p*-polarized light. In addition, *p*-polarized light spectra present two growing bands at ~1230 cm^{-1} and 1430 cm^{-1}, which are absent in the *s*-polarized light spectra, and can be related to –SO$_3^-$ and –HSO$_3$ groups, respectively. In this way, more positive potentials induce an orientation in the membrane sulfonic groups nearest the electrode surface. Likewise, the –HSO$_3$ anion band implies a redox equilibrium on the electrode surface and confirms the sulfonate groups as the adsorbing species on Nafion® coated electrode between 0.45–0.55 V, analogue to (bi)sulfate adsorption equilibrium on Pt(111) [65,66,91].

Sulfate/bisulfate adsorption on Pt electrode surface has been systematically investigated and characterized by IRRAS technique [91,110]. The spectra for bisulfate ions on Pt electrode surface exhibited the blueshift with increasing electrode potential while for sulfate adsorption on Pt(111), a weak redshift of the peak 1120 cm^{-1} was observed with potential increase [20,110]. The lack of a wavenumber shift in this study would suggest that sulfonate anions are not specifically adsorbed but populated in the double layer. However, confined polymer environment or an assisted charge transfer by water molecules can obscure this movement. Additionally, combined IR spectroscopy and density functional theory calculations on a model side chain for Nafion® revealed that many modes dominated by the side chain C–F stretching also contain coupled motion of atoms in the C–O–C and –SO$_3^-$ functional groups [88–90]; specially, changes within the 1250–1100 cm^{-1} region, where the asymmetric stretching mode(s) of –SO$_3^-$ are known to absorb [89,90]. More work is necessary to clarify this point.

The band at 1100 cm^{-1}, assigned to perchlorate ion inside the membrane, increases with the electrode potential, indicating that ionomer cannot exclusively support the electrical double layer and this have contribution from bulk electrolyte ions. Anions can penetrate into Nafion® structure and probably reach the Pt surface possibly because of the high concentration of the acids employed in the present study (0.1 M HClO$_4$), in a similar way to the case of SO$_4^-$ anions.

Figure 1-6 shows *p*-polarized and *s*-polarized light IRRAS spectra for successive potential jumps between 0.10 and 1.20 V, every 100 mV, for Nafion® coated Pt(111) in 0.1 M HClO$_4$. The reference spectrum was taken at 0.10 V. Between 0.10 and 0.90 V, the spectra are similar in both Figs. 1–4 and 1–5, indicating that the membrane is not fully hydrated. In addition to the bands discussed before, *s*-polarized light spectra have a new band at 1450 cm^{-1}, characteristic of protonated sulfonic groups. This band is not clearly

seen in Figs. 1–4 or 1–5 and indicates a small fraction of protonated terminal side chain groups.

Figure 1-6: A series of IRRAS spectra recorded for Nafion® coated Pt(111) electrode surface. The reference spectrum was taken at 0.10 V (RHE) and the sample potential E_2 varied from 0.10 to 0.90 V. Left: *p*-polarized light. Right: *s*-polarized light. In the inset, it is included the spectral region from 3000 to 4000 cm^{-1}, in order to show the behavior of the OH stretching band. Other experimental parameters are the same as in Fig. 1–4.
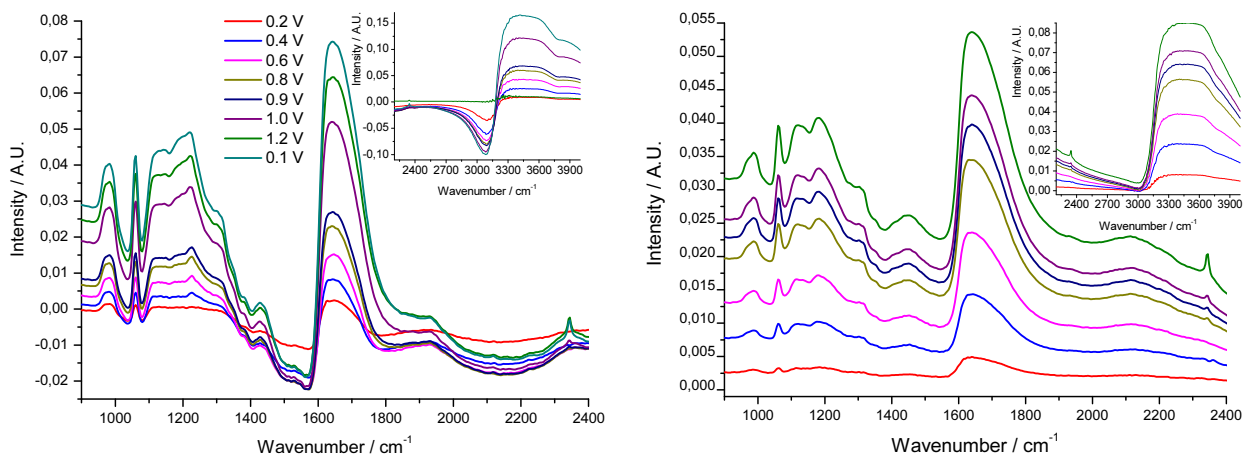
It should be noted that there is a sudden increase in the band intensity for almost all bands above 0.9 V in *p*-polarized light spectra (Fig. 1–6), especially in the bands of water, and this could be related to a change in the optical properties of the metal/membrane interface. This phenomenon can be associated with a change in the membrane/metal interactions at the beginning of the surface oxidation at this potential, similar to the effect discussed before in the cyclic voltammetry experiments.

In a previous work, Malevich *et al.* related the band intensity of a bipolar band with its peak to peak amplitude difference, and demonstrated its proportionality with the surface concentration of the species responsible of that band [78]. Peak to peak amplitude differences of the bipolar bands related to OH stretching and bending water modes in the *p*-polarized and *s*-polarized light spectra are plotted *vs.* electrode potential in Figure 1-7.

Initially, peak to peak amplitude grows almost linearly with the potential for both types of polarized light. At 0.9 V the curve for *p*-polarized light presents a jump, indicating a sudden increase in band intensity in this region (Fig. 1–7). Osawa *et al.* has reported experimental evidence of the formation of stable ice–like structured water on positively charged Pt surfaces [108]. This conclusion was based in the appearance of a broad band at ~3000 cm^{-1} in the ATR–SEIRAS spectrum in 0.1 M HClO$_4$. It was suggested that this band is expected to be shifted from ~3000 to ~3200 cm^{-1} on an oxidized Pt surface, if water molecules are hydrogen bonded to surface oxide, and would considerably increase in intensity by surface oxidation. However, as in their work the ice–like structure was stable even in the surface oxidation region they gave as a possible explanation that the Pt atoms always appear on the oxidized surface due to the place exchange between the adsorbed oxygen species and underlying Pt atoms.

On the basis of the results discussed above, we suggest that the band shift from ~3100 to ~3200 cm^{-1} (Fig. 1–6) together with growth of the peak to peak amplitude difference (Fig. 1–7) at Nafion®/Pt(111) interface can be a clear evidence of the water ice–like structure

disruption. This rupture can be originated because the membrane prevents the place exchange of the Pt(111) atoms during surface oxidation, or because this surface structure is weaker than at the Pt(111)/solution interface, due to the weaker hydrogen bonding network inside the membrane compared to bulk water.

Figure 1-7: Peak to peak amplitude of bipolar bands in the *p*-polarized (*s*-polarized) light spectra. Left: Water bending, 1570−1650 (1565−1640) cm^{-1}. Right: OH Stretching, 3100−3355 (3020−3335) cm^{-1}, as function of the electrode potential (Data extracted from Fig. 1–6).
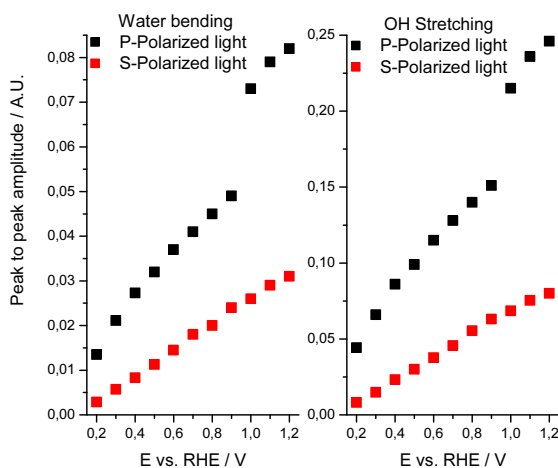
1.3.3 CO-Pt(111)/Nafion® Interface

Cyclic voltammetry. The electro-oxidation of saturated Pt(111)/Nafion®-CO and Pt(111)-CO adlayers were investigated. The CO adlayers were prepared by exposure of the electrode surface to CO gas dissolved in 0.1 M perchloric acid solutions at 0.10 V in an oxygen–free atmosphere. After the formation of a saturated adlayer of CO, witnessed by the low double layer current recorded in the CV between 0.10 and 0.30 V, Ar. was bubbled through the solution for at least 15 min to remove traces of dissolved CO. During the removal of CO from solution, the working electrode was kept at open circuit potential above the solution. Figure 1-8 shows the CVs recorded at 50 mV s^{-1}. As it can be seen in the inset to Fig. 1–8, when the CO adlayer is fully oxidized the CVs for both solutions recover the original profile.

CO oxidation at Pt(111)/Nafion® interface at 50 mV s^{-1} takes place at more positive potentials and within a narrower peak compared to the Pt(111) electrode (Fig. 1–8): ~0.87 V *vs.* ~0.77 V. This behavior suggests that Nafion® influences reaction environment and slows down CO oxidation. This could be caused by a structural modification of the CO adlayer or by a change in the adsorption conditions of the oxygenated species necessary for CO oxidation, *i.e.* adsorbed OH [39,111], similar to the CO oxidation in sulfuric acid solutions on Pt(111) [112–114]. At 20 mV s^{-1} the CV has two consecutive sharp peaks for the CO oxidation, the fist one at ~0.82 V and the second one around ~0.84 V (Data are not shown).

During the negative-going sweep, in the CV of the Nafion® covered electrode appears a broad reduction peak, centered at ~0.36 V, inset to Fig. 1–8. This peak could be related to bicarbonate anion desorption that comes from CO_2 produced during CO oxidation [92].

Bicarbonate adsorbs on the electrode due to a major residence time near the metal surface because its slower diffusion rate through the membrane, this was also evident from IRRAS measurements (Left, Figure 1-10). Slow CO_2 diffusion may be a serious drawback in other Pt surface sites because CO formation would be possible [115–117].

Figure 1-8:   Cyclic voltammograms for saturated Pt(111)/Nafion®-CO and Pt(111)-CO adlayers in 0.1 M $HClO_4$ solution. Potential sweep rate 50 mV s^{-1}. Inset: detailed view of the double layer region in order to show the adsorption-desorption processes.
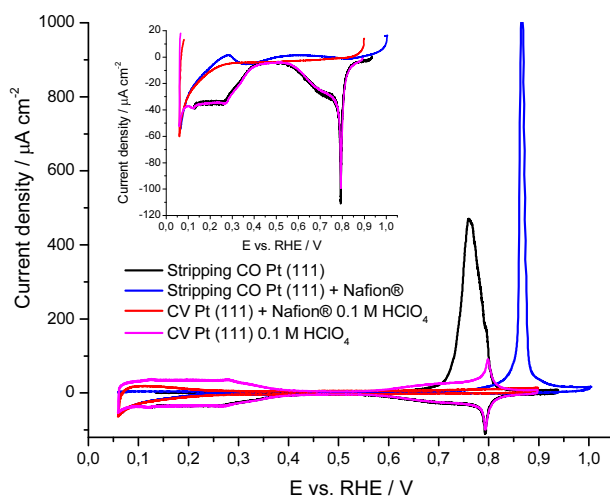
Active surface area of Nafion®/Pt(111) electrodes was estimated by integration of the hydrogen adsorption and CO oxidation charges from the CVs. The active surface area determined by both methods was always lower for Nafion®/Pt(111) as compared to the Pt(111) interface, *i.e.* the ratio between the charges for CO-Pt(111)-Nafion®/CO-Pt(111) was 0.70 at 50 mV s^{-1} and 0.75 at 20 mV s^{-1}. Furthermore, the active surface area was always lower when determined by the hydrogen adsorption charge than by the CO oxidation charge, at least as much as twice lower. This suggests a Nafion® layer shift by the adsorbed CO, which is confirmed by an increase in the hydrogen adsorption charge in the following potential cycles after CO oxidation. With successive cycling, the membrane slowly recovers its initial distribution near the electrode surface. However, the increase in the charge for the hydrogen adsorption is not higher than the active area determined from CO oxidation charge. Hence, it can be concluded that the membrane preferably blocks surface sites with adsorption strength that can be displaced by CO adsorption but not by hydrogen adsorption.

***In situ IR* reflection spectra.** *In situ* IRRAS has been employed to investigate CO adsorption and oxidation at Nafion®-coated Pt(111) interface. A voltammetric sweep was performed between 0.1 and 0.9 V at scan rate of 2 mV s^{-1}. Figure 1-9 shows IRRAS spectra of CO for free and Nafion® covered Pt(111) electrodes in 0.1 M $HClO_4$ at 0.5 V, obtained by choosing as reference potential the single beam spectrum collected at 0.9 V.

There are significantly differences between the CO spectra on both electrode surfaces. The most striking characteristic for Nafion®/Pt(111) interface is that no bridge-bonded CO band, at around 1840 cm^{-1}, was observed [38,39]. Likewise, the wavenumber of linearly bonded CO is blue-shifted for covered electrode: 2075 cm^{-1} *vs.* 2067 cm^{-1}, contrary to the

results reported by other authors for polycrystalline Pt [39]. CO_2 band is similar in both spectra as it would be expected for a non adsorbed species.

Figure 1-9: IRRAS spectra of CO adsorbed on Pt(111) in Ar. saturated 0.1 M $HClO_4$ solution at E = 0.5 V (RHE). Scan rate of 2 mV s^{-1}. The reference spectrum was taken at 0.9 V (RHE).
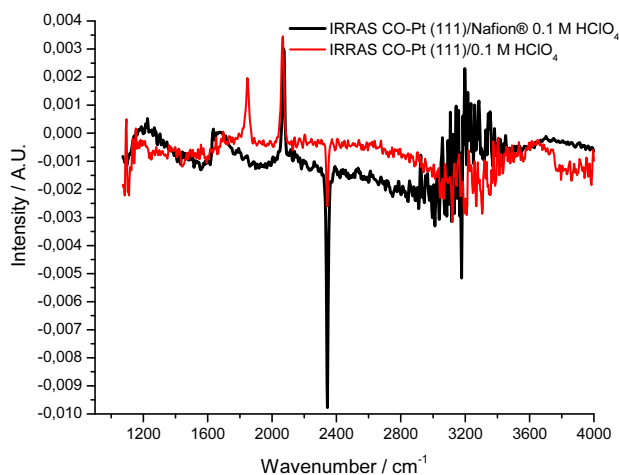
Considering that the linear CO band shifts to higher frequencies with decreasing *pH* for bulk Pt electrodes [113,114,118], and Nafion® is a super acid [8,100,103,104], the band shift on the polymer covered electrode points toward a local *pH* differences between Pt(111) and Pt(111)/Nafion® interfaces, *i.e.* higher proton activity in the nearest surface layer on the membrane covered electrode, in accordance to previously discussed results (increase of the band intensity at 1780 cm^{-1} with higher potentials). Alternatively, the difference between the wavenumber of the linearly bonded CO for membrane covered and membrane free electrodes could be caused by a different packing density in the CO adlayer, because lower CO coverage or fewer water molecules around each CO molecules at the membrane hydrophobic regions in the first case than in the second case (wavenumber closer to that of gaseous CO, ~2100 cm^{-1}) [111,119,120].

We would like to point out that while CO oxidation on Pt(111) starts at ~0.45 V, with a maximum CO_2 intensity at ca. 0.65 V (Left, Fig. 1–10), on the Nafion® covered electrode this oxidation process is shifted to ~0.65 V, with a maximum CO_2 intensity at ~0.85 V (Left, Fig. 1–10), similarly to that reported by Malevich *et al.* [39].

Above ~0.60 V, the CO oxidation is completed for the bare Pt(111) electrode and the band intensity of CO_2 quickly decreases with time (Left and right, Fig. 1–10). For the Nafion® covered electrode, CO oxidation is completed at ~0.90 V and CO_2 inside the membrane remains up to potentials below 0.10 V during the cathodic sweep (Left and right, Fig. 1–10). Therefore the CO_2 diffusion rate is slower through the membrane than in bulk water and facilitates bicarbonate absorption at approximately 0.36 V, as it can be seen on the CV (Fig. 1–10).

The intensity and wavenumber of CO band also depend on the electrode potential (Centrum and right, Fig. 1–10) while band width for both CO and CO_2 has similar behavior at both interfaces during the whole potential sweep. In the case of CO molecules, the full width at half maximum is around 14–15 cm^{-1} and is almost independent of the electrode

potential and CO coverage, until the beginning of the CO oxidation is reached [113,114,119]. Similar behavior has been observed for CO-stripping on a Pt(111) electrode by Chang and Weaver [111] and for a polycristalline Pt electrode by Malevich *et al.* [39] This could indicate that CO oxidation at the Pt(111)/Nafion® interface takes place through island formation, nucleation and growth kinetics, because the environment of CO molecules inside the islands remains essentially unchanged with coverage [39,111].

Figure 1-10: CO IR bands analysis for bare Pt(111) (red) and Nafion® covered/Pt(111) (black). Left: CO_2-Integrated band intensity versus the electrode potential. Centrum: Wavenumber of the CO band at maximum intensity. Right: CO-Integrated band intensity versus the electrode potential.
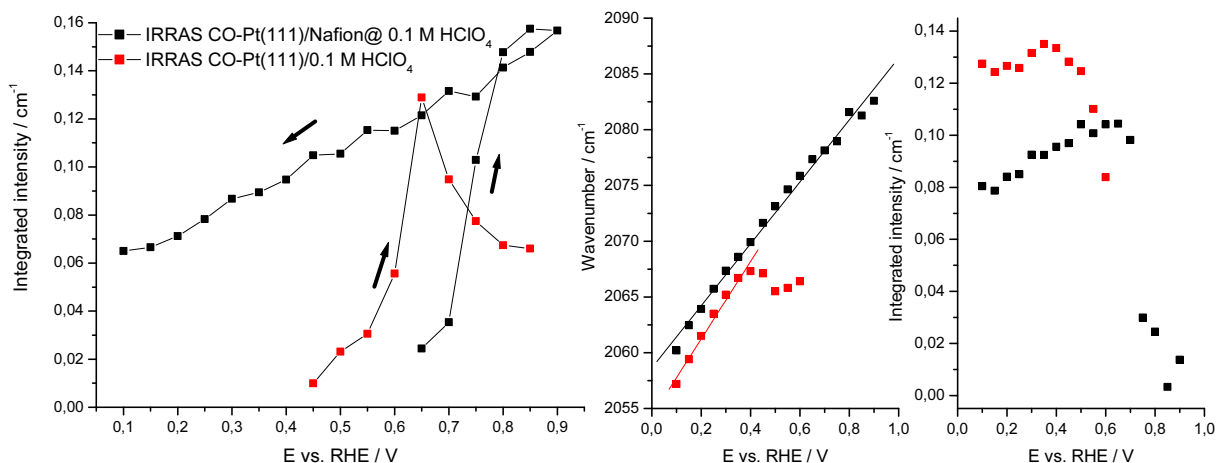
During the whole potential sweep the wavenumber for linearly bonded CO on the Nafion® covered electrode is always greater than on the bare Pt(111) electrode (Centrum, Fig. 1–10) and continuously increases with potential at 29 cm^{-1} V^{-1} (Stark tuning rate). This shift is consistent with the previous literature reports for Pt bulk electrodes [38,39], while for Pt(111) the slope is 34 cm^{-1} V^{-1} up to the onset of CO oxidation, similar to that reported for a coverage of 0.65 ML approximately [91,108,119].

The oxidation of adsorbed CO requires that water molecules penetrate the compact CO adlayer, providing oxygen needed for the conversion of CO to CO_2. This reaction is slower for adlayers that display stronger dipolar coupling [39]. From the results discussed above, the Stark effect is slightly larger for the bare surface than for the covered electrode and this could imply that the dipole–dipole coupling effect, operating between the dipoles of the CO molecules adsorbed on the surface covered with the ionomer membrane, is stronger than on the bare Pt(111). This, concomitantly with the presence of less water molecules around the surface CO islands on the membrane hydrophobic region, would cause the upward shift of the wavenumber for linearly bonded CO during CO oxidation.

The current theory for CO oxidation takes into account that its rate determining step is the formation of hydrogen bonded water–OH$_{ads}$ network, strongly influenced by anions, and that CO oxidation occurs, at least in part, by the diffusion of OH$_{ads}$ through this network [121]. To understand why a stronger dipolar coupling exists at the Nafion®/Pt(111) interface, it can be tentatively proposed that CO molecules are preferentially adsorbed at the hydrophobic region over the surface electrode while the OH molecules can only be adsorbed in the hydrophilic region. Hence, the CO and OH$_{ads}$ diffusions are slower and the coverage within the hydrophobic CO islands remains essentially unchanged. The presence of the membrane adds an additional restriction to the CO oxidation.

Although it has been shown that a lower packing density in the CO adlayer favors the CO oxidation [93], in the present investigation conditions this factor apparently plays only a secondary role. It seems that both, stronger dipolar coupling and a lower *pH* near to the surface, primarily determine the slower catalytic activity at the Pt(111)/Nafion® interface.

1.4 Conclusions

In this work some structural aspects of the Nafion®/Pt(111) interface and its electrochemical behavior have been studied by cyclic voltammetry and *In situ* InfraRed Reflection Absorption Spectroscopy (IRRAS). Nafion® film showed good stability and electrode adherence while its electrochemical behavior was modified quantitatively. The membrane introduces a new charge transfer process at 0.50 V and a surface blockage at both hydrogen and OH adsorption regions, due to the membrane/electrode interactions, strongly dependent on solution *pH* and the pretreatment methods used in the cast film preparation. IR analysis demonstrates that membrane functional groups respond with the changes in the electrode potential, especially the water and sulfonic entities inside the membrane. In addition, the electric field can drive the film morphology to quasi-irreversible metastable states with enhanced proton transport. The interaction between sulfonic groups of the Nafion® membrane and a Pt(111) electrode resembles the interaction between this electrode and a sulfuric acid solution. Additionally, CO stripping experiments reveals that Nafion® film modifies the CO-adlayer structure, which only shows on–top adsorption with a higher wavenumber band that continuously increases with the potential, even during CO oxidation, which is slowed down in the presence of the ionomer. Finally, the CO oxidation peak for the stripping reaction is sharper and shifted to higher potential values on covered Pt(111) electrode.

2. Theoretical Voltammetric Response of Electrodes Coated by Solid Polymer Electrolyte Membranes[2]

A model for the differential capacitance of metal electrodes coated by solid polymer electrolyte membranes, with acid/base groups attached to the membrane backbone, and in contact with an electrolyte solution is developed. It extends the conceptual framework for the interpretation of cyclic voltammograms for these systems and the general theory about electrified interfaces. With proper model parameters, the model reproduces the results from both the Mott-Schottky and Gouy-Chapman-Stern theories as limiting cases. The model is also valid for ionic membranes with other proton donor/acceptor molecules as membrane counterions. Results are discussed in light of the electron transfer rate of electrochemical reactions that strongly depend on the double layer structure on membrane-coated electrodes. It is shown that local maxima and minima in curves of the potential dependence of the double layer capacitance may occur, close to the potential of zero charge, as consequence of the acid/base dissociation of membrane ions and the different mobility of the charge-carrier species, even though there is no specific adsorption of polymer ions. The model provides a tool towards the understanding of the electro-catalytic activity on modified electrodes. However, structural features of real systems are more complex and presented results are only qualitatively compared with experiments.

2.1 Introduction

Modification of electrode surfaces by coating them with a film of a selected chemical moiety to modify the physical, electrochemical and/or optical properties of the unmodified substrate has been a very active area of electrochemistry in recent years [1,2]. A number of reviews, discussing the preparation, characterization, and electrochemical response of chemically modified electrodes, are available [1]. The film can be an irreversible adsorbed (or covalent attached) monolayer or a polymeric (or inorganic) multilayer coating. Hence, it is important to distinguish between physical adsorption, where the film is attracted to the surface via electrostatic or non-electrostatic interactions, and chemical adsorption, where a part of the molecule is chemically bound (grafted) to the surface [3].

Modified electrodes are attractive mainly in electrocatalysis, but they could be employed in electrochromic, molecular electronic and active display devices, in analytical sensors, reference electrodes or to protect the underlying substrate from corrosion or chemical attack [1]. In addition, they have been used to characterize electron- and mass-transfer

---

[2] This work has been submitted.

processes in polymers and other materials, giving insights into how surface structures can be designed to carry out specified reactions or processes [1,4]. Specifically, electrodes coated with ion selective membranes based on solid polymer electrolytes (SPE) are used in many electrochemical systems where selective separation of ion fluxes is required, like proton membrane fuel cells (PMFC) [5–8], wastewater treatment equipment [10,11] and electrochemical sensors [1,12,13]. SPE are usually ionomers, *i.e.* polymers with ionic groups (*e.g.* SO_3^-, CO_2^-, PO_3^-) on the side chains [3,4,8]. The most extensive investigated ionomer is Nafion®, a polymer of tetrafluoroethylene (PTFE) in which the elementary blocks are $-(CF_2)_n-CFR-(CF_2)_n-$, with $R \equiv -O-CF_2-SO_3^-$ as the side chain [5,6,8,18].

Several theoretical studies have described the equilibrium adsorption of neutral and charged polymers to surfaces and interfaces. They include the analysis of polymer/surface interactions, solvent quality, surface characteristics and polymer structures [3,122,123]. Most of these works have used scaling, mean–field, self–consistent field and molecular theories [2,7,123–130]. For an extensive review see the work of Netz and Andelman [3,122]. Nevertheless, few theoretical studies have focused on the relations between the modified electrode electrochemical properties and the molecular organization within the layer [2,77,98,124,129–136]. Besides, the molecular complexity of the problem forces much of this theoretical work to rely on phenomenological ideas and excludes specific film molecular characteristics [1,98,131–136], providing a partial description of the electrochemical processes [124]. Additional work is needed towards a full understanding of the interfacial phenomena at these integrated electrochemical systems.

The structure and dynamics of the electrode/SPE interface, *i.e.* the formation of the electrical double layer (EDL), has been usually described by employing either models in analogy with the conventional Mott-Schottky (MS) model of charge transfer and band bending near a semiconductor/metal interface [137,138], considering the restricted mobility of the ionic groups on the side chain attached to the polymer backbone [1,44–47,77,139,140], or an extended version of the classical Gouy-Chapman-Stern (GCS) model [141–143], in which the position of the SPE charges are considered discrete [144]. These models give similar plots of the interfacial differential capacitance as a function of the electrode potential [144] and a square-root asymptotic scaling of the total charge with diffuse layer voltage for the charged diffuse layer composed by immobile membrane ions [44–47,140]. However, in these systems there is at least one protonable species and, therefore, the properties of the modified electrode should depend on the *pH* of the solution in contact or adjacent to the electrode [2].

In contrast, theoretical approaches have been developed to calculate the interfacial potential distribution (IPD) and the reversible voltammetric, or chronoamperometric, response of metal electrodes coated with irreversible monolayer and submonolayers. These films are either electroactive molecules or electrochemically inert films of molecular acids or bases confined to the surface electrode, such as Langmuir–Blodgett (LB) and self–assembled monolayers (SAMs) [124,145–152]. For SAMs, models have predicted that their acid/base equilibrium may be shifted by changes in solution conditions and the electrode potential, which in turn is coupled with the molecular organization of the film [124,145,148,149,152]. In addition, under certain conditions, a maximum in the capacitance–potential curves is expected due to the dissociation of the acid at increasing electrode potential. These predictions have been validated by Cyclic Voltammetry (CV) [146,149,153], Electrochemical Impedance Spectroscopy (EIS) [154–156], Fourier

Transform InfraRed External Reflection (FTIR–ERS) [153] and Surface Enhanced Raman scattering Spectroscopy (FT–SERS) experiments [157].

In this work, a model for the electrode/SPE interface in contact with an electrolyte solution is proposed, in which the membrane contains acid/base groups attached to its polymer backbone. The model includes both a thermodynamic treatment of the acid/base equilibrium between charged groups inside the ionomer and a discrete description of the charge position, taking into account the different mobility of polymeric ionic groups and counterions inside the membrane. Similar to the case of adsorbed monolayers, and even in absence of specific adsorption of polymeric anions to the electrode surface, an asymmetrical maximum in the current–potential curves may appear. This asymmetric response is a consequence of changes in the fraction of ionizable groups, due to changes in solution conditions and the applied electrode potential.

2.2 Electrochemical model for the interface

The model starts by assuming that the metal electrode is a flat surface with an area, A, located at $x = 0$. It is covered by an electroinactive SPE, physically adsorbed, of thickness δ (m) and with a dielectric constant $\mathcal{E}_M$. The SPE membrane lays at the Outer Helmholtz Plane (OHP), which is the plane of closest approach for the fully solvated membrane and bulk ions, at a distance d_{OHP} (m) from the electrode surface. At the Inner Helmholtz Plane (IHP), the inner layer of the electrode/SPE interphase between the electrode and OHP ($0 < x < d_{OHP}$), there is a layer of water molecules, whose properties are different from the bulk water. This inner water layer has a low dielectric constant, $\sim 3 \leq \mathcal{E}_{IHP} \leq 15$ [148], and a thickness of d_{OHP}. The potential in this region is described by a linear profile [1] (see Figure 2-1).

Figure 2-1: Schematic model of the electrode/SPE interface. Discretisation was only considered in the direction perpendicular to the metal. The ions in the membrane are assumed to lie in planes separate by a fixed lattice space, ΔX. The distance from the electrode surface is designated as 'x' and the first lattice plane in the SPE is situated at $x = d_{OHP}$. A schematic representation of the potential distribution across the SPE and the electrolyte solution is also given.
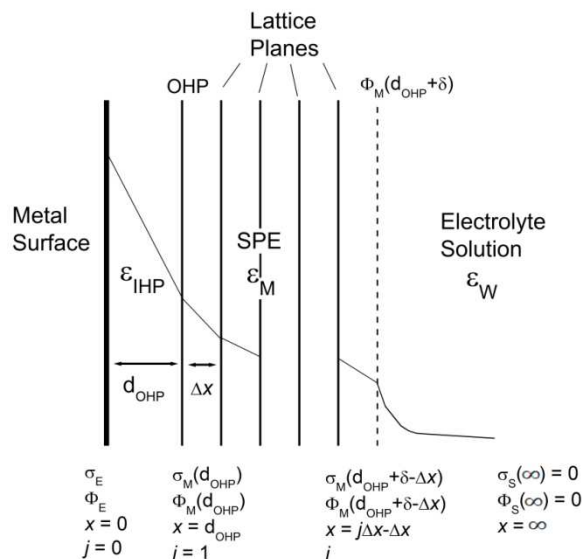
At $x = (d_{OHP}+\delta)$, the outer surface of the membrane is in equilibrium with a large volume of a $z{:}z$ symmetrical electrolyte solution of concentration n (mol cm^{-3}) and dielectric constant $\mathcal{E}_W$. Therefore, the model considers two interfaces: the metal/SPE and the SPE/solution interfaces. In the first case, an electrical diffuse layer, of size L_{EDL} (m), spreads inside the membrane as result of the electrode potential, ϕ_E (V) [139]. In the second case, an electrical potential difference is established between the membrane and the solution, ϕ_{EQ} (V). This difference arises from an equilibrium balance of the selective charge exchange across the interface, usually called Donnan equilibrium [1,158,159], even in absence of the metal/SPE interface. Because of that, there is a continuous IPD that diffuses over distances of order $1/\kappa_M$ on both sides of the membrane/solution interface, where local electroneutrality no longer holds [158,159]. The parameter κ_M (m^{-1}) is known as the membrane Debye–Hückel parameter defined by

$$\kappa_M = ze(\frac{2n}{\varepsilon_0 \varepsilon_M k_B T})^{1/2} \tag{2.1}$$

where e is the charge of an electron (C), $\mathcal{E}_0$ is the permittivity of free space (C^2 N^{-1} m^{-2}), k_B is the Boltzmann´s constant (J K^{-1}) and T is the absolute temperature (K). Without the metal/SPE interface, electroneutrality applies at distances beyond $1/\kappa_M$ on the membrane side.

If $\delta > (L_{EDL}+1/\kappa_M)$, the IPDs around both interfaces do not interact each other and the membrane potential, $\phi_M(x)$ (V), at $(d_{OHP}+L_{EDL}) < x < (d_{OHP}+\delta -1/\kappa_M)$ is ϕ_{EQ}. Otherwise, IPDs will depend significantly on the membrane thickness δ. In the case of the electrolyte solution $x > (d_{OHP}+\delta)$, the IPD follows the GCS theory [141–143], decaying to the potential in the bulk solution, $\phi_S(\infty)$, according to [158,159]

$$tanh(\frac{ze(\phi_S(x)-\phi_S(\infty))}{2k_BT}) = tanh(\frac{ze(\phi_S(d_{OHP}+\delta)-\phi_S(\infty))}{2k_BT})\exp{(-\kappa_S(x-d_{OHP}-\delta))} \tag{2.2}$$

where $\phi_S(x)$ is the potential (V) in the electrolyte solution at position x and κ_S is the Debye–Hückel parameter for the solution. For simplicity, the model considers only electrolyte solutions with monovalent ions resulting from the dissociation of pH-determining electrolytes (*e.g.* HClO$_4$). However, it can be applied for ions with any valence.

The SPE is made up of lattice planes with no electronic conductivity, j, of separation ΔX (m). Each plane contains a uniform density M (mol cm^{-3}) of ionizable acid/base groups and non-ionizable molecules of similar structure. The anions are immobile and represent the negative ionized groups bounded to polymer backbone (A$^-$). Polymer counterions are mobile cations (H_M^+) and they are at equilibrium with H$^+$ in the bulk of the electrolyte solution, H_S^+. It is assumed that the transference number for H_S^+ is unity, and zero for any other ion in the solution.

Other considerations within the model are that charges on the metal electrode surface (at $x = 0$) and at each plane are delocalized; therefore, charge discreteness at $x = 0$, ΔX, $2\Delta X$, $3\Delta X,…$ is ignored. This means that there is a single, averaged potential value at each plane, $\phi_M(x)$, and each ion feels this potential through a 2D ionic atmosphere effect. Additionally, all centres of the ionic charges must lie in one of the SPE lattice planes. Thus, they are at distances x of ΔX, $2\Delta X$, $3\Delta X$, ... $j\Delta X$, from the electrode surface. Finally, the only charge in the membrane is associated with ions formed through the acid/base

dissociation equilibrium at $x = \Delta X$, $2\Delta X$, $3\Delta X$ etc. and the electrolyte counterions permeated from the solution.

The main qualitative elements of the present model for the electrode/SPE/solution system are depicted in Fig. 2–1. The important feature of the SPE for the present discussion is that the dissociation degree of the head group HA, to give the anionic terminating group A⁻, depends on the solution *pH*, applied potential and distance from the electrode surface. Following past works [145,146], this can be assessed by writing down the thermodynamic condition for the equilibrium per plane *j*:

$$HA \leftrightarrow H^+ + A^- \tag{2.3}$$
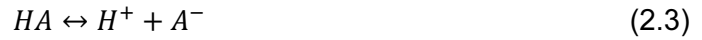
which is represented by

$$\bar{\mu}_{HA}^{\alpha}(x) = \bar{\mu}_{H^+}^{\alpha}(x) + \bar{\mu}_{A^-}^{\alpha}(x) \tag{2.4}$$

where $\bar{\mu}_i^{\alpha}(x)$ is the electrochemical potential of species *i* in medium *α*, at a distance *x* from the electrode surface. Species inside the membrane are designated as "*M*" while species in the electrolyte solution identified as "*S*". The electrochemical potential for each species, in every plane is defined as follows,

$$\bar{\mu}_{HA}^{M}(x) = \mu_{HA}^{0} + RT\ln[a(x)_{HA}^{M}] \tag{2.5}$$

$$\bar{\mu}_{A^-}^{M}(x) = \mu_{A^-}^{0} + RT\ln[a(x)_{A^-}^{M}] + z_{A^-}F\phi(x)^M \tag{2.6}$$

$$\bar{\mu}_{H^+}^{M}(x) = \mu_{H^+}^{0} + RT\ln[a(x)_{H^+}^{M}] + z_{H^+}F\phi(x)^M \tag{2.7}$$

and

$$\bar{\mu}_{H^+}^{S}(\infty) = \mu_{H^+}^{0} + RT\ln[a(\infty)_{H^+}^{S}] + z_{H^+}F\phi(\infty)^S \tag{2.8}$$

where μ_i^0 is the standard chemical potential of species *i*; *R* is the universal gas constant (J K⁻¹ mol⁻¹); $a(x)_i^{\alpha}$ is the activity of species *i*, in medium *α*, at a distance *x* from the electrode surface; *F* is Faraday´s constant (C mol⁻¹) and $\phi(x)^{\alpha}$ is the local electrostatic potential at *x* in medium *α*. At equilibrium

$$\bar{\mu}_{H^+}^{M}(x) = \bar{\mu}_{H^+}^{S}(\infty) \tag{2.9}$$

and

$$RT\ln K_a = \mu_{HA}^{0} - \mu_{A^-}^{0} - \mu_{H^+}^{0} \tag{2.10}$$

where *Ka* is the acid dissociation constant for HA in absence of an interfacial electric field. Using relationships (2.4) and (2.9) through (2.10), and approximating the activities of the acid/base species at the SPE by surface concentrations per plane, $c(x)_i^M \Delta X$, it is found that

$$\ln\left[\frac{f(x)}{1-f(x)}\right] = 2.3(pH - pK_a) - \frac{z_{A^-}F}{RT}(\phi(x)^M - \phi(\infty)^S) \tag{2.11}$$

where *pH* denotes the proton activity in the bulk solution, *f(x)* is the fraction of ionizable groups which are dissociate per plane, *i.e.*

$$f(x) = \frac{c(x)_{A^-}^M}{c(x)_{A^-}^M + c(x)_{HA}^M} \tag{2.12}$$

Equation (2.11) relates the fraction of molecules in the deprotonated state per plane $f(x)$ (or chemical state), the local potential at each plane (at a distance $j\Delta X$ from the electrode surface), the acid dissociation constant Ka and the solution pH. This expression was derived before to calculate the differential capacitance of metal electrodes coated with irreversible adsorbed monolayer films of a molecular acid or base [145,146,148–150]. In this paper, the same expression is used to calculate the formation of the EDL of electrodes coated with a physically adsorbed SPE, containing acid/base functional groups in its structure.

From Eqns. (2.7), (2.8) and (2.9), the density of positive mobile charge, $\sigma_+(x)$ (C cm^{-2}), per plane can be calculated similarly to the Boltzmann factor in the GCS theory [141–143]

$$\sigma_+(x) = z_{H^+} F c(\infty)_{H^+}^S \Delta X exp(\frac{-z_{H^+} F(\phi(x)^M - \phi(\infty)^S)}{RT}) \tag{2.13}$$

The corresponding equation for negative immobile charges, $\sigma_-(x)$, is as follows

$$\sigma_-(x) = z_{A^-} F \Delta X f(x) M \tag{2.14}$$

As it can be appreciated from Eqns. (2.11), (2.13) and (2.14), under the present model, the potential dependence of the density of positive and negative charges does not follow the same mathematical expression and so, a different response in capacitance, to changes in the applied potential for the negative and positive potential side during a voltammetric experiment, is expected. When there are both positive and negative charges per plane, the net charge per unit area in the jth layer, $\sigma(x)$, is given by

$$\sigma(x) = \sigma_+(x) + \sigma_-(x) \tag{2.15}$$

For situations where $\phi_M(x) = \phi_{EQ}$, the net plane charge must be zero, *i.e.* $\sigma(x) = 0$. The dependence of $\sigma_-(x)$ on $\phi_M(x)$ implies that, despite immobile anions, the effective, negative membrane charge per plane may change with the charge density on the electrode surface, σ_E (C cm^{-2}).

The model is purely electrostatic in nature. The potential profile through the interface can be expressed simply in terms of the electric field and charge densities throughout the system. With the potential distribution defined above, the magnitude of the electric field, $|\bar{E}|$, at each region is given by

$$\overline{|E|}(x) = \begin{cases} 0 \ (by \ definition) & x < 0 \\ \frac{(\phi_E - \phi_{OHP})}{d_{OHP}} & 0 < x < d_{OHP} \\ \frac{(\phi_{OHP} - \phi_M(d_{OHP} + dx))}{dx} & d_{OHP} < x < d_{OHP} + dx \\ \qquad . & \\ \qquad . & \\ \qquad . & \\ \frac{(\phi_M(d_{OHP} + \delta - dx) - \phi_M(d_{OHP} + \delta))}{dx} & d_{OHP} + \delta - dx < x < d_{OHP} + \delta \\ \kappa_S \left(\frac{2kT}{ze}\right) \sinh(\frac{ze\left(\phi_S(x) - \phi_S(\infty)\right)}{2kT}) & x > (d_{OHP} + \delta) \\ 0 & x \to \infty \end{cases} \tag{2.16}$$

Denoting the electric field between planes i and i-1 as $E[i$-$\Delta X, i]$, the potential on planes i and i-1 is given by

$$\phi_M(i) = \phi_M(i - \Delta X) - \Delta X E[i - \Delta X, i] \tag{2.17}$$

While the electric field between each lattice plane is determined from the charges on the planes, *i.e.*

$$E[i - \Delta X, i] = \frac{1}{2\varepsilon_0 \varepsilon_M}\left(\sum_0^{i-1} \sigma(x) - \sum_i^j \sigma(x)\right) \tag{2.18}$$

The charge balance between the membrane charge and the electrode charge gives:

$$E[i - \Delta X, i] = -\frac{1}{\varepsilon_0 \varepsilon_M}\sum_i^j \sigma(x) \tag{2.19}$$

when $\delta < (L_{EDL}+1/\kappa_M)$, $|\phi_M(d_{OHP}+\delta)- \phi_{EQ}| < 0$. Therefore, inside the summation of Eqn. (2.19), the net surface charge density of the diffusion layer from the solution, σ_S, should be included. It is calculated by the integral of the volume charge density from the outer membrane surface to the bulk of the solution. On the basis of the GCS model, σ_S is defined as follows [1]

$$\sigma_S = -\varepsilon_0 \varepsilon_W \kappa_S \frac{2kT}{e}\sinh\left[\frac{ze\left(\phi(d_{OHP}+\delta)^M - \phi(\infty)^S\right)}{2kT}\right] \tag{2.20}$$

2.2.1 Methodology of solution

The model is solved through iterative and self-consistent calculations. An initial guess potential at OHP is assumed and the electrode charge is calculated by Eqns. (2.13), (2.14) and (2.15). Next, a new potential is estimated by Eqns. (2.15) and (2.19). Finally, potentials and charge densities are computed by sequentially repeating the cycle until $x =$ ($d_{OHP}+\delta$). If $\phi_M(d_{OHP}+\delta) = \phi_{EQ}$ and $|\sum_i^j \sigma(x)| \geq 1\times10^{-4}$ µC cm^{-2}, a new electrode potential at OHP is attempted and calculations are repeated again. In contrast, if $\phi_M(d_{OHP}+\delta)$ is different to ϕ_{EQ}, σ_S from the solution is determined, and if $|\sum_i^j \sigma(x)+\sigma_S| \geq 1\times10^{-4}$ µC cm^{-2} a new electrode potential at OHP is supposed. In cases in which this criterion could not be reached, a minimization of the sum of the squares of the difference between trial and updated potentials was done, by independently varying the value of the OHP potential, *i.e.*

$$\min \sum_0^\infty (\phi_{OHP}^1 - \phi_{OHP}^2)^2 < 1 \times 10^{-9} \tag{2.21}$$

The capacitance at the interface, C_T (µF cm^{-2}), is computed using a simple midpoint approximation [144]:

$$C_T(\phi_E) = \frac{\partial \sigma_E}{\partial \phi_E} \approx \frac{\sigma_E(\phi_E+10mV)-\sigma_E(\phi_E-10mV)}{0.02V} \tag{2.22}$$

Calculation of C_T each 1 mV exactly produces the same results as each 10 mV. Since the membrane is electrochemically inert, the current in a voltammetric experiment, in which the electrode potential is scanned at a constant rate, v (V s^{-1}), results only from interface charging and is given by

$$I = v\frac{\partial\sigma_E}{\partial E} = vC_T \tag{2.23}$$

where I is the current density ($\mu A\ cm^{-2}$).

2.3 Results and discussion

All results presented were calculated using T = 298 K, z = 1 (corresponding to a 1:1 electrolyte) and dx = 3 Å (simulations with bigger and smaller dx values, dx = 5 and dx = 1 Å, produce similar results). Before examining the results, it is useful to define sets of physical parameters in dimensionless groups that will produce similar generalized responses. Figure 2-2 shows the capacitance, C_T, as a function of the electrode potential, ϕ_E. It is important to highlight that ϕ_E in the simulations is equivalent to the difference between the experimental applied potential, E, and the electrode potential of zero charge, E_{PZC}, (E–E_{PZC}) in an electrolyte whose ions do not adsorb on the electrode surface. Both of them measured with respect to an arbitrary reference electrode (*e.g.* Ag/AgCl) [1].

Figure 2-2:   Interfacial capacitance, C_T, for an electroinactive membrane, with acid/base groups, as function of (*pH-pKa*) and electrode potential. In all cases *pH* = 1 and *pKa*: 1) -2; 2) 0; 3) 2; 4) 3; 5) 4; 6) 6. Dotted (. . .) and dashed (- - -) lines correspond to theoretical curves from discretised Gouy-Chapman-Stern model and Mott-Schottky theory, respectively. The six sets of plots are arranged in two columns and three rows. Columns correspond to $\frac{\varepsilon_{IHP}}{\varepsilon_M\,\kappa_M\,d_{OHP}}$ values. Rows correspond to $\frac{M}{2Zn}$ values.
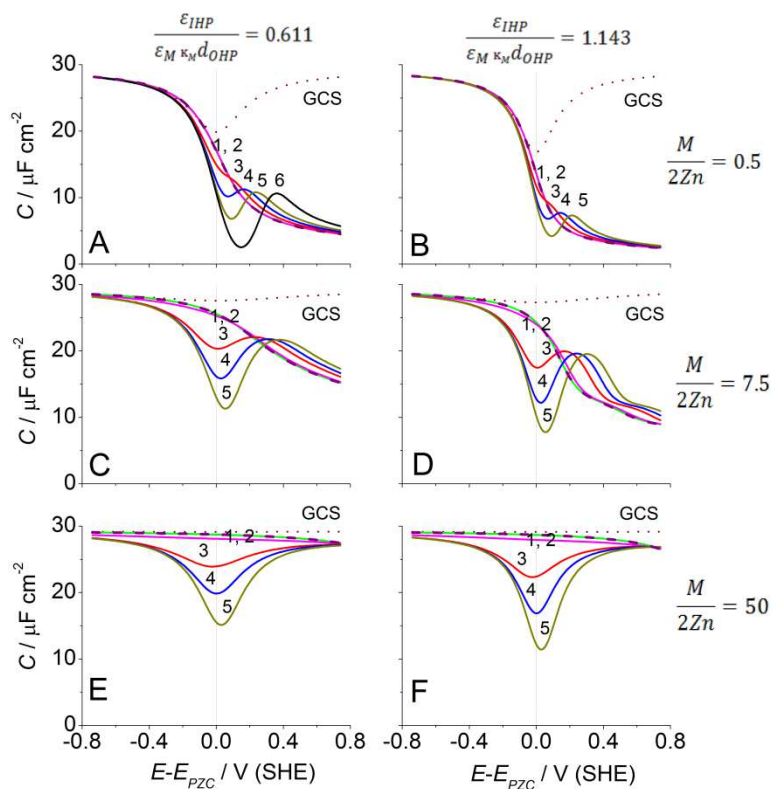
Voltammograms in Fig. 2–2 are arranged in the following way: columns correspond to values of $\frac{\varepsilon_{IHP}}{\varepsilon_M \, \kappa_M \, d_{OHP}}$ (the ration between IHP and membrane capacitances), while the rows correspond to different values of $\frac{M}{2Zn}$ (the ration between the density of ionizable acid/base groups in the membrane and electrolyte concentration in the solution). For a given $\frac{\varepsilon_{IHP}}{\varepsilon_M \, \kappa_M \, d_{OHP}}$ and $\frac{M}{2Zn}$, a set of voltammograms are presented as a function of the *pKa*, at constant *pH* = 1. For the sake of comparison, theoretical curves calculated from the discretised GCS and MS models are also provided. In all cases, the membrane thickness was greater than the EDL length of both electrode/membrane and membrane/solution interfaces, *i.e.* $\delta > (L_{EDL}+1/\kappa_M)$, hence $\phi_M(x)$ at $(d_{OHP}+L_{EDL}) < x < (d_{OHP}+\delta - 1/\kappa_M)$ was ϕ_{EQ}.

The effect of different experimental variables on the capacitive response is shown in Fig. 2–2. In all cases, at large (*pH-pKa*) differences, or potentials higher than E_{PZC}, the capacitance follows the MS model for semiconductors. However, at lower (*pH-pKa*) values, curves clearly deviate. At low and intermediate $\frac{M}{2Zn}$ values (Figs. 2–2A to D), similar to metal electrodes coated by an irreversible monolayer of molecular acid or base [145–149,152], nanoparticles with charged surface groups [160] and ionic liquids [161], a local maximum in C_T–E curves is observed. In some cases, a local, or absolute, minimum is also defined. At large $\frac{M}{2Zn}$ and low (*pH-pKa*) values (Figs. 2–2E to F), the qualitative form of C_T–E curves resemble those calculated from the GCS model but at lower membrane concentrations (Figs. 2–2A to B), *i.e.* near E_{PZC} there is a minimum in the capacitance. However, contrary to the GCS model, this local, or absolute, minimum in capacitance is not located at E_{PZC} but at ϕ_{EQ}.

Experimentally, local maximums close to the *PZC* have been observed in cyclic voltammograms of coated electrodes, as in the case of platinum surfaces covered by Nafion® [22,29,65–69,162], or a different cationic-exchange membrane [162], gold surfaces coated by Nafion® [22,23], or catalytic layers (CLs) for PMFC composed by Pt, carbon and SPEs, as poly(benzimidazole) [163] or Nafion® [162]. In some cases, this peak is not commented upon [29,163], but in others, it has been interpreted in terms of either the formation of oxygenated species on the Pt surface [162] or a specific absorption of Nafion® negative groups on the electrode surface [22,23,65–69]. IR spectroscopy-based techniques [22,164] and Atomic Force Microscopy (ATM) [23] have given support to the latter explanation. However the lack of a wavenumber shift of both protonated and dissociated Nafion®'s sulfonic groups with the electrode potential [20,22,67,78,164], and other experimental techniques [40,165], would suggest that sulfonate anions are not specifically adsorbed but populated in the double layer [20,67,78]. In any case, undoubtedly there is a strong interaction between Pt and Nafion® giving rise to a preferential orientation, electric field driven, of membrane molecular units.

The theoretical results described above have shown the existence of a local maximum in capacitance–potential curves as consequence of the acid/base ionization process inside the membrane and the different mobility of the charge-carrier species, without considering the specific adsorption of membrane ions, suggesting another possible explanation for the reported experimental results. A physical interpretation for the origin of the capacitance peak in Fig. 2–2 can be understood as follows: from Eqns. (2.17) and (2.19), the potential drop across the interfacial region from the metal electrode to the OHP is given by

$$\phi_M(d_{OHP}) = \phi_E(x = 0) - \frac{d_{OHP}}{\varepsilon_0 \varepsilon_M} \sigma_E \qquad (2.24)$$

and

$$\phi_{j+1} = \phi_M(d_{OHP}) + \frac{\Delta X}{\varepsilon_0 \varepsilon_M} \sum_1^{j-1} i\, \sigma_{i+1} + \frac{\delta \sigma_S}{\varepsilon_0 \varepsilon_M} \tag{2.25}$$

If $\delta > (L_{EDL}+1/\kappa_M)$, $\sigma_S = 0$ and $\phi_{j+1} = \phi_{EQ}$,

$$\phi_M(d_{OHP}) = \phi_{EQ} - \frac{\Delta X}{\varepsilon_0 \varepsilon_M} \sum_1^{j-1} i\, \sigma_{i+1} \tag{2.26}$$

In order to derive an expression for the differential capacity of the interface, C_T, Eqns. (2.24) and (2.26) are derived with respect σ_E

$$\frac{1}{C_T} = \frac{\partial \phi_E(x=0)}{\partial \sigma_E} = \frac{\partial \phi_M(d_{OHP})}{\partial \sigma_E} + \frac{1}{C_{IHP}} \tag{2.27}$$

where C_{IHP} is the Helmholtz capacitance: the capacitance at the IHP due to the existence of closest- ion's distance approach, and it is given by

$$\frac{1}{C_{IHP}} = \frac{d_{OHP}}{\varepsilon_0 \varepsilon_M} \tag{2.28}$$

and

$$\frac{\partial \phi_M(d_{OHP})}{\partial \sigma_E} = -\frac{\Delta X}{\varepsilon_0 \varepsilon_M} \frac{\partial}{\partial \sigma_E} \sum_1^{j-1} i\, \sigma_{i+1} \tag{2.29}$$

$$\frac{\partial \phi_M(d_{OHP})}{\partial \sigma_E} = \frac{\Delta X}{\varepsilon_0 \varepsilon_M} \left[1 + \frac{\partial \sigma_1}{\partial \sigma_E} - \frac{\partial}{\partial \sigma_E} \sum_1^{j-2} i\, \sigma_{i+2} \right] \tag{2.30}$$

using

$$\sigma_E = -\sum_1^j \sigma_i \tag{2.31}$$

and

$$1 = -\frac{\partial}{\partial \sigma_E} \sum_1^j \sigma_i \tag{2.32}$$

Additionally, from Eqn. (2.15)

$$\frac{\partial \sigma(x)}{\partial \sigma_E} = \frac{\partial \sigma_+(x)}{\partial \sigma_E} + \frac{\partial \sigma_-(x)}{\partial \sigma_E} \tag{2.33}$$

In consequence, similar to the GCS theory, C_T will be determined by the lower capacitance between C_{IHP} and an effective "membrane" capacitance, $C_M = \frac{\partial \phi_M(d_{OHP})}{\partial \sigma_E}$. When $(E-E_{PZC}) < \phi_{EQ}$, $\frac{\partial \sigma(x)}{\partial \sigma_E} \approx \frac{\partial \sigma_+(x)}{\partial \sigma_E}$, C_T will be similar to that predicted from the GCS model. The only difference stems in the use of the proton concentration inside the membrane at equilibrium with the electrolyte solution, $c_{EQ}{}_{H^+}^M$, instead of $c(\infty)_{H^+}^S$ as the bulk proton concentration (Fig. 2–2). Contrary, when $(E-E_{PZC}) > \phi_{EQ}$, $\frac{\partial \sigma(x)}{\partial \sigma_E} \approx \frac{\partial \sigma_-(x)}{\partial \sigma_E}$. In this case, for a fully deprotonated membrane, $f(x) \to 1$ and $\sigma_-(x)$ is constant, so the system will approach the MS model (Fig. 2–2) [44–47,139,140]. Hence,

$$\sigma_E = -z_{A^-} F M L_{EDL} \tag{2.34}$$

and Eqn. (2.26) becomes

$$\phi_{M}(d_{OHP}) = \phi_{EQ} - \frac{z_{A^-}FML_{EDL}^2}{2\varepsilon_0\varepsilon_M} \tag{2.35}$$

Combining Eqns. (2.24), (2.34) and (2.35) L_{EDL} is given by

$$L_{EDL} = -d_{OHP}\frac{\varepsilon_M}{\varepsilon_{IHP}} + \sqrt[2]{\left(\left(d_{OHP}\frac{\varepsilon_M}{\varepsilon_{IHP}}\right)^2 + \frac{2\varepsilon_0\varepsilon_M}{z_{A^-}FM}(\phi_E - \phi_{EQ})\right)} \tag{2.36}$$

As in past works [44–47,140], a constant $\sigma_-(x)$, Eqn. (2.36) predicts a square-root asymptotic scaling of the total charge with applied potential for the charged diffuse layer composed by immobile membrane ions. In addition, from Eqn. (2.35), it is obtained that

$$\frac{\partial\phi_M(d_{OHP})}{\partial\sigma_E} = -\frac{z_{A^-}FML_{EDL}}{\varepsilon_0\varepsilon_M}\frac{\partial L_{EDL}}{\partial\sigma_E} \tag{2.37}$$

Therefore, C_T slowly will decrease as the electrode potential increases because L_{EDL} continuously increases with the square root of ϕ_E (Fig. 2–2). Otherwise, if $f(x) < 1$ from Eqns. (2.11) and (2.149

$$\frac{\partial\sigma_-(x)}{\partial\sigma_E} = z_{A^-}F\Delta XM\frac{\partial f(x)}{\partial\sigma_E} \tag{2.38}$$

$$\frac{\partial f(x)}{\partial\sigma_E} = -z_{A^-}\frac{F}{RT}f(x)(1-f(x))\frac{\partial\phi_M(x)}{\partial\sigma_E} \tag{2.39}$$

and Eqn. (2.30) becomes

$$\frac{\partial\phi_M(d_{OHP})}{\partial\sigma_E} = \frac{1-\frac{\partial}{\partial\sigma_E}\sum_1^{j-2}i\sigma_{i+2}}{\frac{\varepsilon_0\varepsilon_M}{\Delta X}+z_{A^-}^2\frac{F^2}{RT}\Delta XMf(d_{OHP})(1-f(d_{OHP}))} \tag{2.40}$$

In this case ($f(x) < 1$), because $\sigma_-(x)$ varies in response to the electrostatic potential inside the membrane, from 0 for $\phi_E << \phi_{EQ}$ to $z_{A^-}F\Delta XM$ for $\phi_E >> \phi_{EQ}$, C_T may reach a maximum value at $\phi_E > \phi_{EQ}$ when the membrane is half ionized at d_{OHP} ($f(d_{OHP}) = \frac{1}{2}$). The limiting dynamics from $f(d_{OHP}) \rightarrow 0$ to $f(d_{OHP}) \rightarrow 1$ is determined by the dielectric and geometrical characteristics of the interphase (C_{IHP}, ε_M), which have been assumed to be potential independent. Once the local maximum has been reached at $f(d_{OHP}) = \frac{1}{2}$, other lattice planes, neighbors to OHP, also reach this half ionized condition and $f(d_{OHP}) \rightarrow 1$. Therefore, the total capacitance continuously decreases with further increases in the electrode potential. It is important to note that, although the local capacitance maximum is reached when $f(d_{OHP}) = \frac{1}{2}$, it is not possible to estimate an effective membrane *pKa* value without a suitable model for the EDL, because $\phi_M(d_{OHP})$ cannot be known from experimental measurements [1].

Another characteristic feature of the present model is the lack of linearity between the density of ionizable groups attached to the polymer backbone and the height of the capacitance maximum. From this point of view, it does not seem feasible to carry out a quantitative determination of *M* from an analysis of the capacity curves.

The complete membrane ionization process can be better appreciated by examining the influence of ($E–E_{PZC}$) on the ionization process at the first membrane lattice plane, d_{OHP} (Figure 2-3), and from the distribution of the dissociated fraction of ionizable groups'

across the electroinactive membrane per plane, $f(x)$, as function of the applied potential. In Figure 2-4, a representative example of $f(x)$ at $(E-E_{PZC}) = 0.38$ V is shown.

Figure 2-3:   Fraction of molecules in the deprotonated state, $f(d_{OHP})$, plotted against electrode potential, E, for systems A (A), C (B) and E (C) in Fig. 2–2. $\dfrac{\varepsilon_{IHP}}{\varepsilon_M\,\kappa_M\,d_{OHP}} = 0.611$. In all cases $pH = 1$ and pKa: 1) -2; 2) 0; 3) 2; 4) 3; 5) 4; 6) 6.
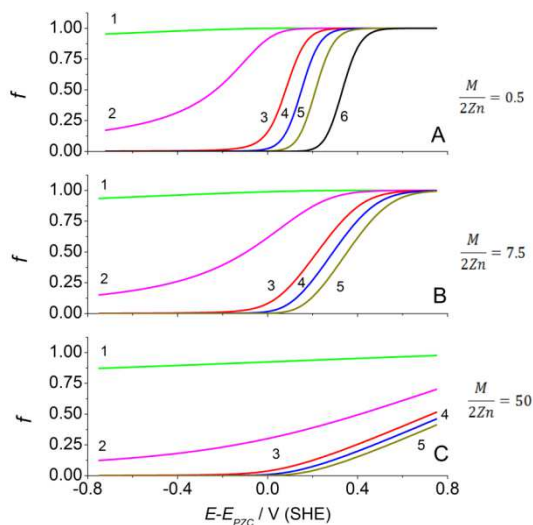
Figure 2-4:   Interfacial profiles for the fraction of molecules in the deprotonated state, $f(x)$, for systems A (A), C (B) and E (C) in Fig. 2–2 at $(E-E_{PZC}) = 0.38$ V, and pKa: (■) -2; (●) 0; (▲) 2; (▼) 3; (◆) 4; (●) 6. $pH = 1$ and $\dfrac{\varepsilon_{IHP}}{\varepsilon_M\,\kappa_M\,d_{OHP}} = 0.611$.
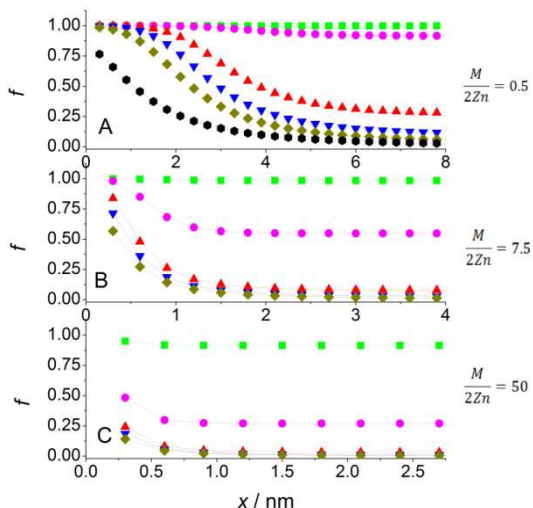
Figures 2–3 and 2–4, together with in Fig. 2–2, show how the extent of the ionization process at d_{OHP} and inside the membrane increases as the electrode potential is made more positive. Then, the structure of the polymer electrolyte close to the surface is different than that in the bulk and changes with the applied potential. These changes in $f(d_{OHP})$ and $f(x)$ with the applied potential have already been experimentally observed through different spectroscopic techniques for Nafion®–Poly(Pt) [20,22,78], Nafion®–Pt/C and Nafion®–Pt₃Co/C [164] and Nafion®–Pt(111) interfaces [67].

As mentioned, the appearance of a local maximum in C_T–E curves is determined by $f_{EQ} <$ 0.5 and the value of $c_{EQ}{}_{H^+}^M$ (Fig. 2–4), which, in turn, determines the existence of a local (or global) minimum in the curve. These equilibrium values are defined by the (*pH-pKa*) difference and $\frac{M}{2Zn}$. On the other hand, the peak amplitude is determined by the value of $\frac{\varepsilon_{IHP}}{\varepsilon_M \kappa_M d_{OHP}}$ and $\frac{M}{2Zn}$; higher $\frac{\varepsilon_{IHP}}{\varepsilon_M \kappa_M d_{OHP}}$ or lower $\frac{M}{2Zn}$ values give rise to narrower capacitance maximums and the full shape of the curve will be easier to observe (Fig. 2–2).

2.3.1 Extent and electron transfer rate on membrane coated electrodes

The presence of a membrane close to the electrode surface, where electrochemical reactions (ECRs) take place, may affect the overall reaction kinetics [44–49]. ECR rate constants, accompanying by electron transfer (ET) via the electrolyte/metal interface, exponentially depend on the electrode potential or, more specifically, on the overpotential (ϕ_E-$\phi_S(\infty)$ -$E^{0'}$), where $E^{0'}$ is the reaction formal potential. Phenomenologically, this influence is usually described by employing the Tafel, or Butler–Volmer, law. For a totally irreversible one-step, one-electron reaction the Tafel law is given by [1]

$$\frac{I}{FA} = k_0 C_0(0, t) \exp\left(-\alpha \frac{F}{RT}(\phi_E - \phi_S(\infty) - E^{0'})\right) \qquad (2.41)$$

where k_0 is the standard rate constant, $C_0(0, t)$ is the concentration of the reacting species outside the diffuse layer and α is the global transfer coefficient [1]. This empirical dependence is attributed to the electric field contribution to the reaction free energy and to the reaction activation energy changes [1,77,139]. This expression is particularly valid in the cases when ECR includes the ET over the entire EDL [77] or for reactions close to equilibrium, because the reaction rate is determined by thermodynamic values [139]. In these situations, neglecting any membrane electronic effect, the presence of the membrane would slightly affect the ET because the equilibrium potential is ϕ_{EQ} instead of $\phi_S(\infty)$, in addition to the change in the mass transfer coefficient of reactants and products.

For irreversible reactions that need a high overpotential to take place, or for reactions far from equilibrium occurring close the metal surface [77,139], the EDL structure strongly affects the ET kinetics. This effect, first discussed by Frumkin [166], has usually been described by replacing (ϕ_E-$\phi_S(\infty)$) by (ϕ_E-$\phi_S(d_{OHP})$-$\phi_S(\infty)$) in Eqn. (2.41). Therefore, the field contribution to the reaction free energy is smaller than ϕ_E and the potential difference driving the electrode reaction is smaller [77,139,166]. Additionally, if reacting species are ionic, their concentrations are affected by the potential similar to Eqn. (2.13) and so, they will be different to $C_0(0, t)$. Hence, in these cases, the effect of the membrane on the ECR is expected to be stronger. In agreement, few general models of thin electrochemical cells, including the Frumkin correction to calculate the ET rate of relevant ECRs, have shown that diffuse charge effects can be important even in SPEs [44–52].

Figure 2-5 shows values of the local potential at d_{OHP} as a function of the applied potential for some cases shown in Fig. 2–2. As can be seen, the presence of the membrane, in general, increases the absolute value of the potential at the OHP, $|\phi_M(d_{OHP})|$, and thus, decreases the ET rate of ECRs. At any $\frac{M}{2Zn}$ value, if $f_{EQ} < 1$, this effect is stronger for $\phi_E > \phi_{EQ}$ than that predicted by both the GCS and MS models, and even for $\phi_E < \phi_{EQ}$ at intermediate and high $\frac{M}{2Zn}$ values. Lower f_{EQ} values make even bigger the difference

between the $|\phi_M(d_{OHP})|$ calculated by GCS or MS models and that predicted by our model. However, surprisingly at high $\frac{M}{2Zn}$ and low (pH-pKa) values the overall ET rate actually increases (curves 1 and 2 in Fig. 2–5C).

Figure 2-5:   Local potential at the OHP, ϕ_{OHP}, as function of applied electrode potential, E, for systems A (A), C (B) and E (C) in Fig. 2–2. $\frac{\varepsilon_{IHP}}{\varepsilon_M \, \kappa_M \, d_{OHP}}$ = 0.611. The central "0" on the plot from the GCS model indicates the point of zero charge. In all cases pH = 1 and pKa: 1) -2; 2) 0; 3) 2; 4) 3; 5) 4; 6) 6.
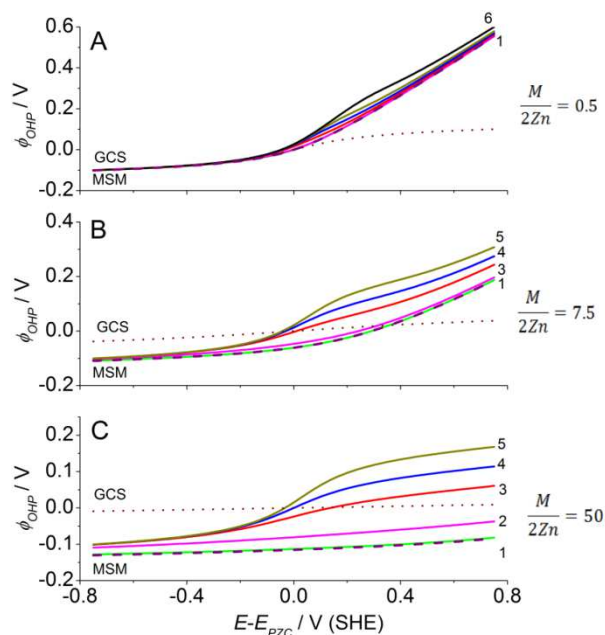
Specifically, the EDL structure of an interface is mainly determined by the interfacial potential distribution and the excess charge density on each plane, as functions of the applied potential. In order to closely analyze the EDL structure for the Metal/SPE interface, Figures 2–6 and 2–7 depict the potential profile in the EDL for the electrode/membrane interface and the normalized charge density profile inside the membrane at (E–E_{PZC}) = 0.38 V, respectively. These figures also include the theoretical predictions from both discretised GCS and MS models.

Similar to GCS and MS models, the potential inside the membrane decays from its value on the surface until to reach the equilibrium potential, ϕ_{EQ}. This latter potential may be either positive or negative, depending on $\frac{M}{2Zn}$ and (pH-pKa), which in turns also define f_{EQ}. Lower f_{EQ} values increases ϕ_{EQ} and, at higher $\frac{M}{2Zn}$ values there is a larger increase in $\phi_M(x)$ close to the surface as the membrane passes from the dissociated to the protonated state (Fig. 2–6). In addition, if f_{EQ} = 1, the EDL length approaches the predicted value from the MS model and increases at lower f_{EQ}. Thick EDLs with higher $\phi_M(x)$ will reduce even more the average ECRs rate compared to thin layers with lower $\phi_M(x)$ values. Thus, membranes with low f_{EQ} values would markedly inhibit ECRs. At larger $\frac{\varepsilon_{IHP}}{\varepsilon_M \, \kappa_M \, d_{OHP}}$ values, the potential decay is more abrupt and so, the EDL is thinner (data not shown).

Figure 2-6:   Interfacial potential profiles for systems A (A), C (B) and E (C) in Fig. 2–2 at E = 0.38 V, and *pKa:* (■) -2; (●) 0; (▲) 2; (▼) *pKa* = 3; (♦) 4; (⬡) 6. Dotted (. . .) and dashed (- - -) lines correspond to theoretical curves from discretised Gouy-Chapman-Stern model and Mott-Schottky theory, respectively. The fraction of molecules in the deprotonated state at equilibrium, f_{EQ}, is also given in figures.
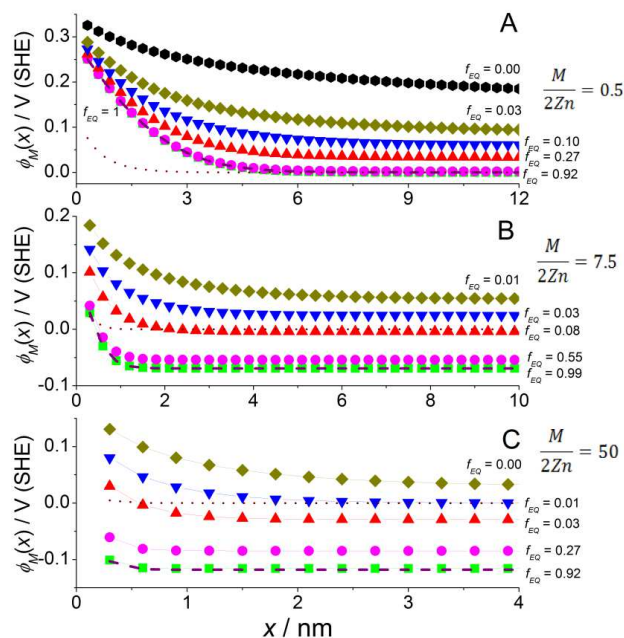
Figure 2-7:   Surface charge density, normalized to the value at OHP, as a function of distance for systems A (A), C (B) and E (C) in Fig. 2–2 at E = 0.38 V, and *pKa:* (■) -2; (●) 0; (▲) 2; (▼) 3; (♦) 4; (⬡) 6. Dotted (. . .) and dashed (- - -) lines correspond to theoretical curves from discretised Gouy-Chapman-Stern model and Mott-Schottky theory, respectively. Lattice spacing 0.3 nm, pH = 1 and $\dfrac{\varepsilon_{IHP}}{\varepsilon_M \, \kappa_M \, d_{OHP}}$ = 0.611.
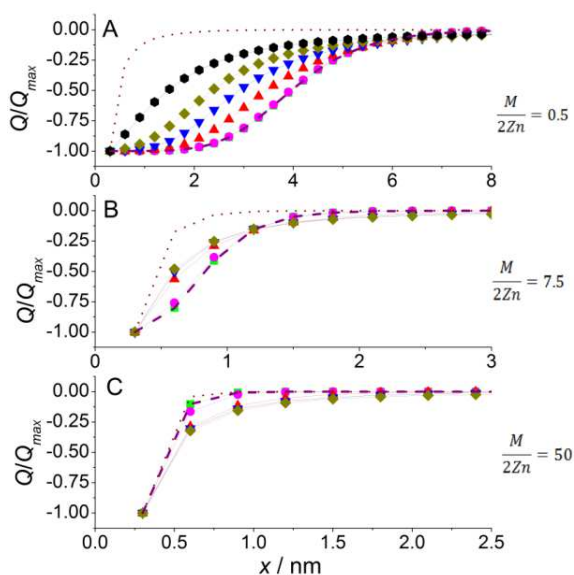
On the other hand, in the case of ionic reacting species, besides to changes in the overpotential, there are also changes on the species concentration, $C_0(0, t)$, because of $\phi_M(x)$, Eqn. (2.13). Hence, in some situations, the overall reaction rate, Eqn. (2.41), may increase because of the increase on $C_0(0, t)$, and despite the decrease in the overpotential, *e.g.* first order reactions either for anionic reacting species, close to the reaction onset, with an $E^{0'} > \phi_{EQ}$ or cationic species with an $E^{0'} < \phi_{EQ}$. Of course, electrocatalytic reactions are complex processes and their kinetics are affected by a large number of parameters not considered here, such as changes in the activation energy with the surface coverage and the presence of either intermediate species or ordered surface structures [1,67,167]. A comprehensive analysis should always consider all these parameters when analyzing a specific reaction mechanism.

Comparing Figs. 2–6 and 2–7, it is clear that the charge density decays more abruptly than the potential. As a result, the effect of discretisation is more noticeable, especially at high $\frac{M}{2Zn}$ values. On the other hand, while in the GCS model there is no limit in the amount of charge per plane, the restricted anion mobility in the model generates a charge saturation in the lattice planes nearest the interface as ϕ_E increases, $\phi_E > \phi_{EQ}$. In consequence, once $f(d_{OHP}) > \frac{1}{2}$, the capacitance monotonically decreases with the potential far from the PZC (Fig. 2–2). This charge saturation occurs faster at higher f_{EQ} values (Fig. 2–7), and because of this, the capacitance maximum is narrower and the EDL is thinner. At high $\frac{M}{2Zn}$ values, the membrane charge density per plane is higher and higher applied positive potentials are necessary to reach the charge saturation. In these cases, the charge density profile is similar to what is predicted by the GCS theory but with lower *M*.

Experimentally, it has been found that some irreversible ECRs, important in low temperature PMFC, are inhibited on Nafion® covered electrodes. Reported ECRs include the oxygen reduction [66] and the electro-oxidation of methanol [69] and carbon monoxide [67]. In consequence, it is probable that Nafion® membrane falls into one of the categories represented in Fig. 2–5A or B with low or intermediate $\frac{M}{2Zn}$ values. This could be a serious drawback in PMFC and it would be better to find a membrane with a superior diffuse charge effect. In this sense, the fact that for some membranes the overall reaction rate may actually increase, as a consequence of the structure of the double layer (curves 1 and 2 in Fig. 2–5C), opens the possibility to design membranes that, not only, do not inhibit the ECR rate but even could improve it.

2.3.2 Influence of other model parameters

After the discussion, it is useful to analyze the influence of other important model parameters such as the membrane thickness (Figure 2-8), the inner capacitance values, C_{IHP}, (Figure 2-9) and the solution *pH* (Figure 2-10) on the capacitance response as function of the applied potential.

If the membrane is thick enough, *i.e.* $\delta > (L_{EDL}+1/\kappa_M)$, C_T–E curves in Fig. 2–8 superimpose each other. However, when $\delta < (L_{EDL}+1/\kappa_M)$, the capacitance curve only overlaps the curves for $\delta > (L_{EDL}+1/\kappa_M)$ for positive membrane charges, *i.e.* when $(E–E_{PZC}) < \phi_{EQ}$ but deviates from them at higher potentials. In both cases, the local capacitance maximum is located at the same potential. This result can be understood taking into account that when $(E–E_{PZC}) > \phi_{EQ}$, the negative charge inside the membrane is not

enough to compensate the electrode charge. Thus, $L_{EDL} > \delta$ and includes a portion of the electrolyte solution. In this case, deriving Eqn. (2.25), with $\phi_{j+1} = \phi(d_{OHP} + \delta)^M$, results in

Figure 2-8:   Interfacial capacitance, C_T, of the electrode/membrane interface (A) and local potential at OHP, ϕ_{OHP}, (B) plotted against electrode potential, E, and the interfacial potential profiles at $E = 0.38$ V (C) for various membrane thicknesses, δ, as indicated in figure. $pKa = 3$ and $pH = 1$. Other parameters are the same as those in Fig. 2–2A.
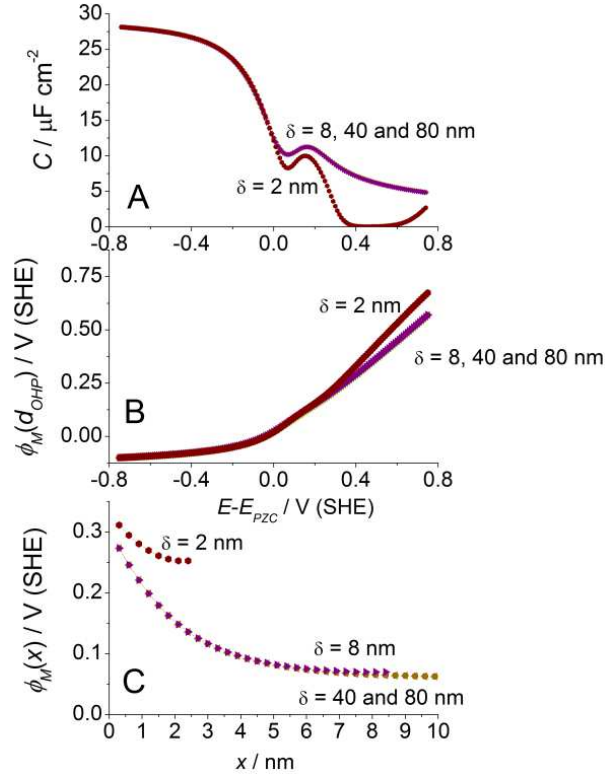
$$\frac{\partial\phi_M(d_{OHP})}{\partial\sigma_E} = \frac{\partial\,\partial\phi(d_{OHP}+\delta)^M}{\partial\sigma_E} - \frac{\Delta X}{\varepsilon_0\varepsilon_M}\frac{\partial}{\partial\sigma_E}\sum_1^{j-1} i\,\sigma_{i+1} - \frac{\delta}{\varepsilon_0\varepsilon_M}\frac{\partial\sigma_S}{\partial\sigma_E} \tag{2.42}$$

while from Eqn. (2.20)

$$\frac{\partial\sigma_S}{\partial\sigma_E} = -C_S\frac{\partial\phi(d_{OHP}+\delta)^M}{\partial\sigma_E} \tag{2.43}$$

where C_S is the potential-dependent solution capacitance. On basis of the GC model, C_S is defined as follows

$$C_S = \varepsilon_0\varepsilon_W\kappa_S\cosh\left[\frac{ze\left(\phi(d_{OHP}+\delta)^M-\phi(\infty)^S\right)}{2kT}\right] \tag{2.44}$$

From Eqns. (2.43) and (2.42)

$$\frac{\partial\phi_M(d_{OHP})}{\partial\sigma_E} = \frac{\left[\frac{1}{C_S}+\frac{\delta}{\varepsilon_0\varepsilon_M}\right]+\left[\frac{1}{C_S}+\frac{(\delta-\Delta X)}{\varepsilon_0\varepsilon_M}\right]\frac{\partial}{\partial\sigma_E}\sum_2^j\sigma_i-\frac{\Delta X}{\varepsilon_0\varepsilon_M}\frac{\partial}{\partial\sigma_E}\sum_1^{j-2} i\sigma_{i+2}}{1+z_A^2-\frac{F^2}{RT}\Delta XMf(d_{OHP})(1-f(d_{OHP}))\left[\frac{1}{C_S}+\frac{\delta}{\varepsilon_0\varepsilon_M}\right]} \tag{2.45}$$

evidencing a complex dynamics. For this situation, Eqn. (2.31) should be substituted by

$$\sigma_E = -\sum_1^j \sigma_i - \sigma_S \tag{2.46}$$

Therefore,

$$\frac{\partial\,\partial\phi(d_{OHP}+\delta)^M}{\partial\sigma_E} = [1 + \frac{\partial}{\partial\sigma_E}\sum_1^j \sigma_i]\frac{1}{C_S} \tag{2.47}$$

Therefore, after the local maximum is reached ($f(d_{OHP})$ = ½), the total capacitance decreases faster than in the case when $\delta > L_{EDL} + 1/\kappa_M$ because C_S continuously decreases for potentials further from the *PZC*. Similarly, once $f(d_{OHP}) \to 1$ is reached, the total capacitance is much smaller because the term $\frac{\partial}{\partial\sigma_E}\sum_2^j \sigma_i$ reduces the value of $\frac{\partial}{\partial\sigma_E}\sum_1^{j-2} i\,\sigma_{i+2}$. However, at more positive potentials $\frac{\partial\sigma_i}{\partial\sigma_E} \to 0$ and C_T again begins to increase, approaching the minimum value between $\frac{\varepsilon_0\varepsilon_M}{\delta}$ and C_{IHP}.

Regarding the ET, one important fact from Figs. 2–8B and C is that when $\delta < (L_{EDL}+1/\kappa_M)$, $\phi_M(d_{OHP})$ and $\phi_M(x)$ are closer to ϕ_E (Figs. 2–8B and C) for ϕ_E values higher than the potential at which $f(d_{OHP}) \to 1$. Because of this, it is expected that the ET rate of ECRs will be more inhibited in thinner, rather than in thicker, membranes. This effect would be particularly important when designing CLs involving SPEs. In the case of PMFC, a parabolic response for the CL-performance as a function of the ionomer amount has been experimentally reported [6,168], *i.e.* the exchange current density (j_0) for a ECR *vs.* ionomer content in the CL. This dynamics is usually explained considering an optimal balance between proton conductivity and oxygen diffusivity inside the CL. However, results here suggest that, in addition to these two factors, changes in the EDL structure when decreasing the ionomer content (smaller δ) can also explain the lower j_0 measured.

Additionally, when analizing the effect of C_{IHP}, Fig. 2–9A, it is found that greater C_{IHP} values sharpen the local capacitance maximum and shift it toward less positive potentials, i.e. while with C_{IHP} = 14.8 µF cm^{-2} only a broad and poor defined peak is obtained, if C_{IHP} is increased to 132.8 µF cm^{-2} a clear current peak is observed, keeping constant all other model parameters. In consequence, because both E_{PZC} and C_{IHP} depend on the substrate, the appearance or not of discernible local maxima could depend on the type of electrode covered by the membrane. This variation in C_T when increasing C_{IHP} arises from changes in the potential drop at IHP, which in turn increases $\phi_M(d_{OHP})$ (Fig. 2–9B). Thus, similar to thinner membranes, higher C_{IHP} values may reduce more the ET rate of ECRs. However in this case, even at $\phi_E < \phi_{EQ}$ the inhibition may occur (Fig. 2–9C). Besides, increasing C_{IHP} also spreads the ionization process over a smaller potential range (Fig. 2–9C) and so, once the local maximum is reached C_T decreases faster at more positive potentials.

Capacitance curves as a function of the solution *pH* are shown in Fig. 2–10A for a membrane with M = 5.0 M, pKa = 1 and ε_M = 20, and with C_{IHP} = 66.4 µF cm^{-2}. Since the electrolyte is assumed to be a strong acid, for example, perchloric acid, the ionic strength, µ, on the solution changes with the *pH*. As can be seen, when *pH* increases, the entire C_T–E curve shifts towards negative potential values. If there are local minimum and maximum in the capacitance, their calculated potential shift is around 0.059 mV (Inset to Fig. 2–10A) per *pH* unit, corresponding to $\frac{2.3RT}{z_A-F}$, as expected from Eqn. (2.11). Nevertheless, the potential range in which the transition from $f(d_{OHP}) \to 0$ to $f(d_{OHP}) \to 1$ occurs remains constant (Fig. 2–10B). This shift in the C_T–E profile occurs due to the decrease in the bulk's hydrogen ion activity.

Figure 2-9: Interfacial capacitance, C_T, (A), local potential at OHP, ϕ_{OHP}, (B) and fraction of molecules in the deprotonated state at OHP, $f(d_{OHP})$, (C) for the electrode/membrane interface plotted against electrode potential, E, for different values of the capacitance at IHP, C_{IHP}, as indicated in figure. Inset to (A): Magnified scale of Fig. A. $pKa = 4$, $pH = 2$, $M = 1.5$ M and $C_M = 5.8$ µF cm^{-2}.
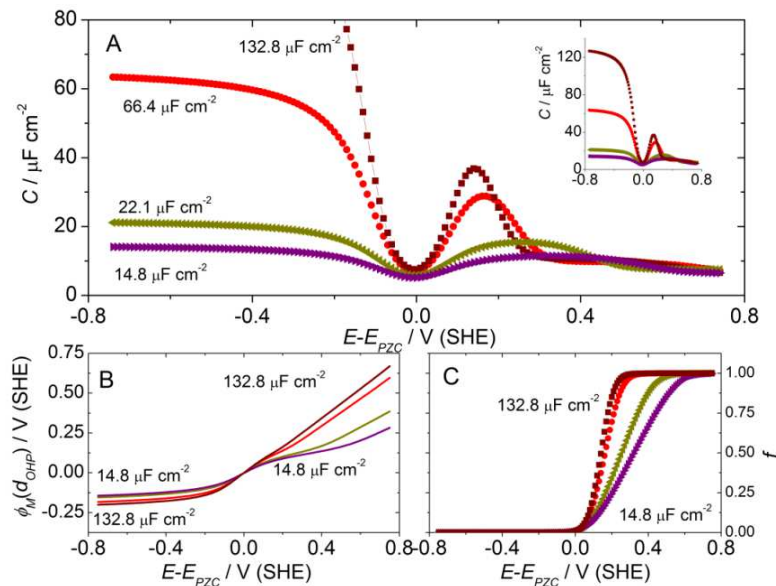
Figure 2-10: Interfacial capacitance, C_T, (A) and fraction of deprotonated molecules at OHP, $f(d_{OHP})$ (B) for the electrode/SPE interface plotted against electrode potential, E, at four solution pHs: 0.0 (solid), 1.0 (dash-dot), 2.0 (dot) and 3.0 (dash). Inset to (A) Peak potential, E_{max}, versus pH. The acid/base groups are at a uniform density $M = 5.0$ M. C_{IHP} = 66.4 µF cm^{-2}, $\mathcal{E}_M = 20$ and $pKa = 1$.
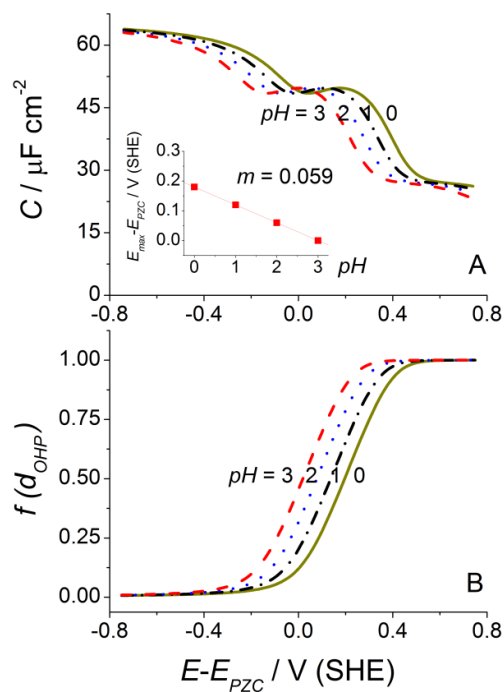
As discussed, the existence of a local minimum or maximum in C_T–E curves depends on different factors, including the dielectric and geometrical interface characteristics and membrane and solution properties. However, if a set of conditions produces a local capacitance maximum, it remains over a large *pH* range, even if *pH > pKa* (Fig. 2–10A), where the dissociation process is thermodynamically more favored. Therefore, the response in Fig. 2–2 is not only because of a large (*pH-pKa*) difference, but also due to specific $\frac{\varepsilon_{IHP}}{\varepsilon_M\,\kappa_M\,d_{OHP}}$ and $\frac{M}{2Zn}$ values. This fact is consequence of the change in ϕ_{EQ} as the solution *pH* increases, which, in turn, changes μ. As μ decreases, the potential drop across the IHP layer becomes greater and decreases the tendency of the head group to dissociate. However, at the same time, ϕ_{EQ} becomes more negative, f_{EQ} decreases, and the potential drop across the EDL at some *E* remains almost constant.

Unfortunately, detailed studies about the structure of the metal/SPE interface and its changes with the solution *pH* are missing and a proper comparison of model predictions with experiments is limited. However, some phenomena, like the presence of a local maximum close to E_{PZC} in C_T–E curves [22,23,29,65–69,162,163], the response of membrane units close to the surface to the electrode potential [20,22,67,78,164] and lower ET rates for ECRs that strongly depend on the EDL structure [6,66,67,69], can be explained in light of the present model. In addition, the model suggests valuable guidelines when designing membranes and CLs, as in the case of PMFC, in order to improve their overall performance, considering the membrane thickness and specific membrane characteristics according to the nature of reacting species. Further improvements in the model should include the effect of coion permeation through the membrane and specific membrane effects, such as the ion solvation energetic and steric restrictions [169]. Finally, it is important to note that the model analysis described above equally applies to any ionic membrane with other proton donor/acceptor molecules, different to H$^+$, as membrane counterions.

2.4 Conclusions

In this study, an electrostatic model for an electrode covered by a solid polymer electrolyte (SPE), in contact with an electrolyte solution, was proposed. The model does not consider specific adsorption of membrane ions on the electrode surface but explicitly includes the acid/base chemical dissociation equilibrium of ionic polymer groups and the different mobility of the charge-carrier species. The differential capacitance (C_T) of these systems as a function of the applied electrode potential, *E*, and the solution ionic strength and *pH* was calculated. The model is discussed for proton conducting membranes but it equally applies to any ionic membrane with other proton donor/acceptor molecules as membrane counterions.

Simulations show that C_T–E curves depend on different factors, including the dielectric and geometrical interface characteristics and membrane and solution properties. The model also predicts as limiting responses both the Mott-Schottky model, for charge transfer near a semiconductor/metal interface, and the Gouy-Chapman-Stern model dynamics. Between these two limits, local maxima (or minima) in the C_T–E profiles may appear as consequence of the dissociation of the acid/base molecular species and differences in ions' mobility.

In addition, the effect of the interfacial potential distribution on the electron transfer rate (ETR) of some electrochemical reactions on SPE coated electrodes is also discussed. It

is shown that, under some conditions, this effect could be significant and should be included in the analysis of the voltammetric response. The presence of the membrane usually slows down the ETR, but in some cases, it can enhance it. Calculations also suggest that cyclic voltammetry can be used to estimate the effective *pKa* of membrane acid/base groups, provided a suitable model.

In spite of the level of simplicity, the model holds great promise in the understanding of the electrocatalytic activity on modified electrodes. It extends the conceptual framework for the interpretation of cyclic voltammograms for these systems and the general theory of electrified interfaces. This is especially true considering that experimental techniques for examining the structure of these layers at molecular level are not available. In addition, the model suggests valuable guidelines when designing membranes and catalytic layers, as in the case of fuel cells, in order to improve their overall performance, considering the membrane thickness and specific membrane characteristics according to the nature of reacting species. Nevertheless, structural features of real systems are much more complex and it is necessary to continue improving the model. Future work will include coion membrane permeation and ion solvation energetics inside the membrane.

3. Charged Ion Interaction Effects at Electrode/Solid Polymer Electrolyte Membrane Interfaces[3]

A model for the differential capacity and the potential distribution at interface between an electrode modified by a solid polymer electrolyte membrane and an electrolyte solution is presented. The model includes the permeation of coions from the solvent phase and considers the ion partitioning equilibrium at the SPEM/solution interface, as a function not only of the Donnan equilibrium, but also the steric hindrance, the solvation energy change when ions move from water to membrane pores and ion electrostatic interactions. Results are compared with those ignoring these effects. It is shown that capacitance maxima may appear not only due to the acid/base dissociation process inside the membrane, but also because of the change in the total interaction energy with the applied potential. At low dielectric constant inside membrane pores, $\mathcal{E}_P$, sharp peaks can be obtained, which broaden, decrease in magnitude and shift to more positive potentials when increasing $\mathcal{E}_P$. Finally, the predictions of this physically more realistic model are discussed in light of recent experimental data obtained on Nafion® covered Pt(111) electrodes, providing a theoretical basis for qualitative electroanalyses of these systems

3.1 Introduction

Solid Polymer Electrolyte Membranes (SPEMs) are polymers with ionic groups covalently attached to the polymer backbone [170]. These ionic groups usually are acid groups, mainly sulfonic or carboxylic acids, and in them the hydrogen ion may be partially or totally exchanged by all kinds of cations or cationic groups [17]. Thus, in contact with electrolyte solutions these membranes may acquire a fixed electric charge [15,16]. SPEMs are widely used in batteries, fuel cells and many other important electrochemical systems such as supercapacitors, photo-electrochemical and electrochromic devices [1,2]. In most of these applications, a thin SPEM layer usually covers the metal electrode and so, the understanding of the electrical, compositional and structural aspects of the electrode/SPEM interface is an essential step toward an optimum design and an overall successful performance of these thin solid state devices [20]. As for example, the catalyst layer of proton electrolyte membrane fuel cells (PEMFC), where highly disperse catalysts, deposited on high-surface-area carbon, are impregnated with Nafion® ionomer, a typical SPEM [5,6,8,18,19].

There are extensive theoretical studies describing polymer adsorption on surfaces and interfaces at equilibrium [3,122,123]. Although, only few theoretical studies treat the link between the electrochemical properties of the modified electrode with the layer's molecular organization [2,77,98,124,129–136]. Indeed, the formation of the electrical double layer (EDL) of the electrode/SPEM interface has been usually described by employing either models in analogy with the conventional Mott–Schottky (MS) model for a semiconductor/metal interface [1,137,138], considering the restricted mobility of the ionic groups on the side chain attached to the polymer backbone [1,44–47,77,139,140,], or an extended version of the classical Gouy–Chapman–Stern (GCS) model [141–143], in which the position of the SPEM charges are considered discrete [144]. However, the acid/base equilibrium of membrane ionic groups significantly influences the overall EDL structure, and is affected by the applied potential and solution properties [145,146,148,149,155,160,171].

Recently, we have described a model for the electrode/SPEM interface in contact with an electrolyte solution. It includes a thermodynamic treatment of the acid/base equilibrium of polymer charged groups and a discrete description of their spatial positions in the membrane, to take into account the different mobility between polymeric ionic groups and counterions inside the membrane [171]. It has been shown that local maxima and minima in curves of the interfacial differential capacitance (C_T) as a function of the electrode potential (E) may occur as consequence of the dissociation of acid/base molecular species, without specific adsorption of the immobile polymer anions. However, this model bases the description of the equilibrium partitioning of ions at the SPEM/electrolyte interface solely on the Donnan equilibrium theory [172], which relates the electrochemical potential in the bulk electrolyte to that within the membrane pores. Additionally, the coions' permeation from the electrolyte solution in is neglected [171].

In order to improve the physical relevance of the description of the process, the existing models should include more of the complex phenomena involved [16]. Experimentally, it has been shown that the coions' permeation through the membrane from the electrolyte solution at the interface SPEM/solution is possible and depends on their concentration in the solution [67]. Besides, it is also known, from the study of electrolyte transport through membranes [15,16,60–64], that the ionic partitioning at membrane/electrolyte solution interfaces mainly depends upon three effects: charge repulsion, steric and dielectric effects. The first effect is caused by the charged nature of the membrane and electrolytes, while the second effect is caused by the relative size of ions to the membrane pores; the third effect is caused by differences in the dielectric constants between bulk and membrane pore [15,16,60–64]. Additional phenomena can also affect the membrane performance, like ion-membrane affinity, specific adsorption and hydration [173].

In the present paper, an extension of the one-dimensional model previously discussed is done [171], in order to include the change in the C_T–E profile when coions from the solvent phase penetrate into the membrane and considering the ion separation at the SPEM/solution interface as a function not only of the Donnan equilibrium, but also the steric hindrance and dielectric exclusion. This latter expressed in terms of (*i*) the solvation energy change that the ions face when moving from the favorable high dielectric environment of water to the unfavorable low dielectric of the membrane [60], and (*ii*) the interaction between ions and the polarization charges, induced at the dielectric boundary between the pore walls and the pore-filling solution, *i.e.* the so-called image charges [15,61–64]. Finally, the predictions of this physically more realistic model are discussed in light of recent experimental data obtained at Nafion® covered Pt(111) electrodes [65–70].

3.2 Electrochemical model for the interface

The main qualitative features of the present model for an electrode/SPEM/electrolyte system were described in Chapter 2 and depicted in Figure 2–1. However, in order to consider coions' permeability from the solution (B⁻), the transference number for H_S^+ is not unity, nor zero for any other ion in the solution. As explained before, the model is developed by writing down the thermodynamic condition per plane *j* for the equilibrium, Eqns (2.3) and (2.4), and the electrochemical potential for each species in every plane, Eqns (2.5) and (2.6). However, in this case, Eqns. (2.7) and (2.8) are replaced by

$$\bar{\mu}_i^M(x) = \mu_i^0 + RT\ln\left[a(x)_i^M\right] + z_iF\phi(x)^M + \Delta W_i(x)^M \tag{3.1}$$

and

$$\bar{\mu}_i^S(\infty) = \mu_i^0 + RT\ln[a(\infty)_i^S] + z_iF\phi(\infty)^S \tag{3.2}$$

where μ_i^0 is the standard chemical potential of species *i*, in the solution *i* = H⁺ and B⁻ and $\Delta W_i(x)^M$ is the interaction free energy, including all interactions of the ion with the medium, not accounting for the mean field (J mol⁻¹) [61], *i.e.* those energy barriers that affect the equilibrium partitioning of ions at the entrance of charged pores in addition to the Donnan potential [15,16,61,62,173]. For example, separation mechanisms such as images forces, ion hydration effects, excluded volume interactions and screening of the charge. If these effects are not considered $\Delta W_i(x)^M = 0$. Assuming local thermodynamic equilibrium at the membrane/solution interface,

$$\bar{\mu}_i^M(x) = \bar{\mu}_i^S(\infty) \tag{3.3}$$

Hence, from Eqns. (3.1) and (3.2), the concentration of the species *i*, inside the membrane, at a distance *x* from the electrode surface, $c(x)_i^M$ is given by

$$c(x)_i^M = c(\infty)_i^S \left(\frac{\gamma(\infty)_i^S}{\gamma(x)_i^M}\right)exp\left(-\frac{z_iF(\phi(x)^M - \phi(\infty)^S) + \Delta W_i^M(x)}{RT}\right) \tag{3.4}$$

where $\gamma(x)_i^\alpha$ is the activity coefficient of species *i*, in medium *α*, at a distance *x* from the electrode surface. It takes into account the deviations from ideality due to ion-ion Coulomb interactions. Activity coefficients are calculated here according to the extended law of the Debye–Hückel theory [174]

$$\ln(\gamma(x)_i^\alpha) = -\frac{\frac{e^2z^2}{8\pi\varepsilon_0\varepsilon_Pk_BT}\kappa'_M(x)}{z_i + r_{ionic}\,\kappa'_M(x)} \tag{3.5}$$

where r_{ionic} is the ionic radius (m) of the ion *i* and κ'_M is the membrane Debye–Hückel parameter. Usually, this latter is assumed to be a function of the solution ionic strength, μ. However, a specific model for the IPD across a charged membrane in equilibrium with an electrolyte solution showed that it is more precise to define κ'_M, *i.e.* the inverse of EDL thickness formed inside the membrane at the interface SPEM/solution, as [158]

$$\kappa'_M(x) = \kappa_M\left[1 + \left(\frac{\sigma_M(x)}{2z^2nF\Delta X}\right)^2\right]^{1/4} \tag{3.6}$$

where $\sigma_M(x)$ is the surface charge density of the membrane at a distance x from the electrode surface.

The distribution of ions in the vicinity of the interface could be calculated if accurate expressions for the change in the total interaction energy of an ion when passing from the solution to the membrane, as a function of the position x, $\Delta W_i^M(x)$, would be available. However, expressing $\Delta W_i^M(x)$ as the sum of three dominant electrical and non-electrical interactions is a simple way to get reasonable estimations of the ion distribution [60],

$$\Delta W_i^M(x) = \Delta W_{Ion-solvent}^M(x) + \Delta W_{Ion-dipole}^M(x) + \Delta W_{Neutral}^M(x) \tag{3.7}$$

where $\Delta W_{Ion-solvent}^M(x)$ and $\Delta W_{Ion-dipole}^M(x)$ represent the change in the ion-solvent and ion-dipole interactions; while $\Delta W_{Neutral}^M(x)$ includes all of the other contributions to the free energy, *i.e.* hydrophobic and Van der Waals interactions, in addition to the steric exclusion. Unfortunately, energetic terms in Eqn. (3.7) cannot be estimated separately since they are strictly connected each other. Because of that, as a first approximation in this work simple expressions to calculate them will be employed. It is important to note, however, that the expressions proposed here for the separation mechanisms caused by solvent properties within confined pores are not expected to exactly represent the physical system. They are used to convey a fundamental understanding and simple quantification of these important phenomena, in a form which retains the practicality of the model and does not introduce further parameters that cannot be readily measured or estimated.

For small ions hydrophobic and Van der Waals interactions are small ca. 2.1–4.2 kJ mol^{-1} [60] and thus, they can be neglected. In this situation, $\Delta W_{Neutral}^M(x)$ can be expressed as function only of the "sieve effect" due to the membrane intrinsic porosity [61]

$$\Delta W_{Neutral}^M(x) = -RTln\varphi_i \tag{3.8}$$

where φ_i is the steric partitioning coefficient for ion i. This parameter is defined as the ratio between the available section, *i.e.* taking into account the zone inside the pore in which the ion center cannot penetrate because of its finite size, and the pore cross section. According to pore geometry, φ_i is usually defined as [15,16,61,62]

$$\varphi_i = (1 - \frac{r_i}{r_p})^2 \qquad \text{(Cylindrical pores)} \tag{3.9}$$

$$\varphi_i = (1 - \frac{r_i}{r_p}) \qquad \text{(Slit-like pores)} \tag{3.10}$$

where r_i is the Stokes radius (m) of specie i [15] and r_p is the characteristic pore size (m), *i.e.* the average membrane pore radius for a cylindrical pore or the half-width for a slit-like pore [15,16,61–63]. The Stokes radius can be estimated from ionic mobilities and by using Stokes–Einstein equation [175]. It is indicative of the apparent size of the dynamic hydrated/solvated particle. The coefficient φ_i is bounded between $0 < \varphi_i < 1$ and it has been added in order to consider the hindered transport through narrow membrane pores, comparable with the molecular dimensions of permeating species [15]. If this steric hindrance is not taken into account $\varphi_i = 1$.

Regarding the ion-solvent interactions, the simplest model to calculate the work of charge transfer from a region with the dielectric constant $\mathcal{E}_W$ to a region with the dielectric constant $\mathcal{E}_P$ is the Born model, given by [60,151,176]

$$\Delta W^{M}_{Ion-solvent}(x) = \frac{ez^2 F}{8\pi\varepsilon_0 r_{ionic}}(\frac{1}{\varepsilon_P} - \frac{1}{\varepsilon_W}) \tag{3.11}$$

A good agreement with experiments has been obtained for a number of ions if the radii used in the Born equation were chosen so as to account for the separation between the ion and the center of the water dipole or the Stokes radius [16,177], instead of r_{ionic} [178].

Finally, approximate expressions for the interaction energy due to image forces, $\Delta W^{\alpha}_{Ion-dipole}(x)$, are taken from previous works, where this phenomenon has been extensively studied [63,64]. In the case of cylindrical pores, equations are mathematically complicated and involve Bessel functions [63,64]. Instead, for slit-like pores the mathematical treatment is much simpler. Thus, in this work the expression for slit-like pores are used, given by [15,63,64]

$$\Delta W^{\alpha}_{Ion-dipole}(x) = -\frac{eFz^2}{8\pi\varepsilon_0\varepsilon_P r_p}\ln\left[1 - \frac{\varepsilon_P-\varepsilon_M}{\varepsilon_P+\varepsilon_M}\exp\left(-2r_p\,\kappa'_M(x)\right)\right] \tag{3.12}$$

This energetic term is always unfavorable for any ion, independently of the ion charge and appears whenever media endowed with different dielectric properties are put in contact with each other. Since the dielectric constant of the solution inside membrane pores is remarkably higher than the corresponding value of the polymeric matrix, electrostatic interactions arise between the ions of the solution inside membrane pores and the polarization charges, induced by the ions themselves, on the discontinuity surface located in the boundary between these two dielectric media [15,61,63,64]. However, for $r_p \geq 6$ nm, $\Delta W^{\alpha}_{Ion-dipole}(x)$ becomes negligible with respect to ion-solvent interactions [15]. In this case, for nearly all small inorganic ions (*e.g.* Na$^+$, K$^+$, Ca^{2+}, SO$_4^-$) the most important factor is the Born electrostatic energy barrier. When calculated by Eqn. (3.11), Born energy for a small ion gives rise to an energy barrier of ~ 50 kJ mol^{-1}, significantly higher than the average thermal energy, ~2.5 kJ mol^{-1} [60].

Now, combining Eqn. (2.10) for *Ka*, with Eqns. (2.4), (3.3) and (3.4), an expression for *f(x)* is calculated, similar to Eqn. (2.11) when it is considered $\Delta W_i(x)^M = 0$, $\varphi_i = 1$ and $\gamma(x)^{\alpha}_i = 1$. Thus, the inclusion of these phenomena does not directly modify the membrane acid/base equilibrium. However, they limit the concentration of mobile species, Eqn. (3.4), and hence, they affect the overall C_T–*E* curves. As mentioned, this equation relates the fraction of molecules in the deprotonated state per plane *f(x)* (or chemical state), the local potential at each plane (at a distance *jΔX* from the electrode surface), the acid dissociation constant *Ka* and the solution *pH*.

The density of positive mobile charge per unit area, $\sigma_+(x)$, in each lattice plane (C cm^{-2}) can be calculated from Eqn. (3.4). This expression is similar to the Boltzmann factor assumed in the GCS theory [141–143], but including the $\Delta W^{M}_{H+}(x)$ factor and the deviations from ideality due to ion-ion Coulomb interactions

$$\sigma_+(x) = z_{H+}Fc(\infty)^{S}_{H+}\Delta X(\frac{\gamma(\infty)^{S}_{H+}}{\gamma(x)^{M}_{H+}})exp(\frac{-z_{H+}F(\phi(x)^M-\phi(\infty)^S)-\Delta W^{M}_{H+}(x)}{RT}) \tag{3.13}$$

A similar expression can be derived from Eqn. (3.4) to calculate the coions concentration inside the membrane, and the density of negative mobile charge per plane due to coion permeation, $\sigma_{B-}(x)$, can be derived in a similar way to Eqn. (3.13)

$$\sigma_{B^-}(x)|_{co-ions} = z_{B^-}Fc(\infty)_{B^-}^S \Delta X \left(\frac{\gamma(\infty)_{B^-}^S}{\gamma(x)_{B^-}^M}\right) exp\left(\frac{-z_{B^-}F(\phi(x)^M - \phi(\infty)^S) - \Delta W_{B^-}^M(x)}{RT}\right) \qquad (3.14)$$

The corresponding equation for negative immobile charges, $\sigma_{A^-}(x)$, is given by Eqn. (2.14). Hence, the net negative charge per unit area in the jth layer, $\sigma_-(x)$, when coions from the solution permeate the membrane, *i.e.* the charge due to A$^-$ and B$^-$ negative ions, is:

$$\sigma_-(x) = \sigma_{B^-}(x) + \sigma_{A^-}(x) \qquad (3.15)$$

When there are both positive and negative charges per plane, the net charge per unit area in the jth layer, $\sigma(x)$, is given by Eqn. (2.15). As mentioned, if $\phi_M(x) = \phi_{EQ}$, $\sigma(x) = 0$.

Similar to Chapter 2, the improved model described here is still purely electrostatic in nature. Therefore, the potential profile through the interface and the electric field between each lattice plane can be expressed by Eqns. (2.17) to (2.19). Again, when $\delta < (L_{EDL} + 1/\kappa_M)$, $|\phi_M(d_{OHP} + \delta) - \phi_{EQ}| < 0$, and summation in Eqn. (2.19) should include the net surface charge density of the diffusion layer from the solution, σ_S, calculated by Eqn.(2.20).

3.2.1 Methodology of solution

Because the model described here conserves the same characteristics than the simpler model developed in Chapter 2, the same methodology of solution is employed.

3.3 Results and discussion

The model described here includes a series of equations representing different phenomena: steric hindrance, the solvation energy barrier, image charges and ion-ion interactions. In consequence, it would be possible to calculate the same ion partitioning with different set of parameters. Therefore, in the following, the effect of these separation mechanisms on the total system capacitance, C_T, will be separately described, in order to get a better understanding. Additionally, similar to the previous chapter [171], dimensionless groups of geometrical and physical parameters, that produce similar generalized curves, are also defined, such as $\frac{\varepsilon_{IHP}}{\varepsilon_M \kappa_M d_{OHP}}$, the ration between the IHP and membrane capacitances, and $\frac{M}{2Zn}$, the ration between the density of ionizable acid/base groups in the membrane and electrolyte concentration in the solution.

Presented results were calculated with T = 298 K, z = 1 (corresponding to a 1:1 electrolyte) and dx = 3 Å. Simulations with bigger and smaller dx values, dx = 5 and dx = 1 Å, produce similar results. Notice that ϕ_E in simulations is equivalent to the difference between the experimental applied potential, E, and the electrode potential of zero charge, E_{PZC}, ($E-E_{PZC}$), in an electrolyte whose ions do not adsorb on the electrode surface. Both of them measured with respect to an arbitrary reference electrode (*e.g.* Ag/AgCl) [1]. In all cases, membrane thicknesses were greater than EDL lengths of both electrode/membrane and membrane/solution interfaces, *i.e.* $\delta > (L_{EDL} + 1/\kappa_M)$, hence $\phi_M(x)$ at $(d_{OHP} + L_{EDL}) < x < (d_{OHP} + \delta - 1/\kappa_M)$ is ϕ_{EQ}. Results for thinner membranes, but considering only the Donnan equilibrium in the ion partitioning equilibrium and neglecting coions' permeation, were discussed in Chapter 2 [171]. Similar results are expected with the model described here.

3.3.1 Steric exclusion and coions' permeation effects

Experimentally, it has been shown that coions from the solution can permeate into the film. This process depends on the magnitude of the field inside the membrane and on coions' charge and concentration [67]. However, ion permeation is also limited by the size of the permeating species, because ions larger in size that membrane pores cannot enter the pore. Figure 3-1 shows different curves of the C_T, the fraction of molecules in the deprotonated state and the local potential at OHP, $f(d_{OHP})$ and ϕ_{OHP}, respectively, as a function of ϕ_E, when steric hindrance and coions' permeation are included into the model. In all cases, steric partitioning coefficients, φ_i, were calculated according to Eqn. (3.9) for cylindrical pores and φ_{H+} is fixed at 0.64. For slit-like pores, the steric exclusion would be smaller because φ_i would be larger, Eqn. (3.10).

Figure 3-1:   A and B: Interfacial capacitance, C_T, for an electroinactive membrane, with acid/base groups, as function of (*pH-pKa*) and electrode potential, considering steric exclusion and coions' permeation through the membrane. In all cases *pH* = 1 and φ_{H+} = 0.64. $\frac{\varepsilon_{IHP}}{\varepsilon_M \, \kappa_M \, d_{OHP}}$, $\frac{M}{2Zn}$, *pKa* and φ_{B-}: (1) 0.611, 0.5, -2 and 0.36; (2) 0.611, 0.5, 4 and 0.01; (3) 1.143, 0.5, 4 and 0.36; (4) 1.143, 50, 4 and 0.36; (6) 1.143, 50, 4 and 0.81; (5) 1.143, 7.5, 4 and 0.36; (7) 1.143, 7.5, 4 and 0.81. C and D are the fraction of molecules in the deprotonated state and the local potential at OHP, $f(d_{OHP})$ and ϕ_{OHP}, respectively. Dashed lines correspond to theoretical curves derived from the original model [171].
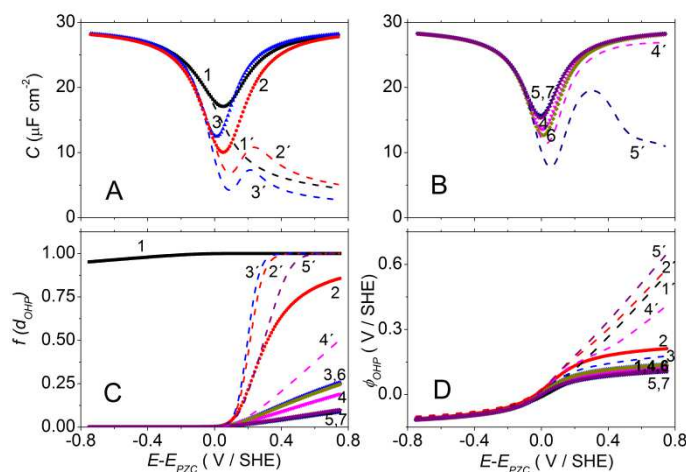
Including the steric exclusion on the model does not significantly modify the total system capacitance, regardless the value of φ_{B-} = 0.81 (curves 6 and 7), 0.36 (curves 1, 3, 4 and 5) or 0.01 (curve 2). The main effect is to decrease the effective ion concentration in the bulk, from $c(\infty)_i^S$ to $\varphi_i c(\infty)_i^S$. Instead, coions' permeation significantly modifies the C_T–E curves when the electrode bears a positive potential, and the EDL is built not only by membrane anions but also by anions from the solution. In consequence, the potential drop close to the surface, between the electrode and OHP, is higher than in absence of permeation (Fig. 3–1D), which, in turn, decreases the deprotonation of membrane anions (Fig. 3–1C). The effect of this can be to "wipe out" the capacitance maximum and so, C_T–E curves tend to the response predicted by the GCS model, but with a more pronounced minimum because of the steric exclusion effect (Figs. 3–1A and B).

3.3.2 Dielectric exclusion and ion-ion Coulomb interactions effects

When describing ion transport through membranes, it has been shown that steric exclusion and Donnan equilibrium are not sufficient to explain the high rejection values for counterions [15,16,61–64,173]. Therefore, it is necessary to include additional energy barriers to decrease the ion flux at the membrane/solution interface. In the next, capacitance curves when including the effect of ion-ion interactions and $\mathcal{E}_P/\mathcal{E}_W$ and $\mathcal{E}_M/\mathcal{E}_P$ differences into the model are described. Contrarily to Donnan equilibrium, dielectric exclusion, mainly caused by the differences between $\mathcal{E}_P$, $\mathcal{E}_M$ and $\mathcal{E}_W$, is always unfavorable for any ion, independent of the ion sign. In the same way, ion-ion interactions decrease the ion activity coefficient and so, the species electrochemical potential.

Change in the solvation energy. The confinement of water molecules within pores affects not only the solvent viscosity but also decreases water dielectric constant [16,61,62]. This reduction in $\mathcal{E}_W$ implies a new energy barrier to ions' solvation into membrane pores. In this work, this mechanism is estimated on the basis of the Born model [60,151,176], Eqn. (3.11), and hence, similar to Donnan equilibrium, represents the addition of a constant energy term in Eqns. (3.13) and (3.14). This has the advantage to be easily included in the model, without increasing the complexity of calculations. Figure 3-2 shows C_T and $f(d_{OHP})$ as function of (pH-pKa) and the electrode potential, when including the change in the solvation energy of both positive and negative permeating ions. In all cases $\varphi_{H+} = 0.64$ and $\varphi_{B-} = 0.36$.

Figure 3-2: Interfacial capacitance, C_T, for an electroinactive membrane, with acid/base groups, as function of (pH-pKa) and the electrode potential, including the change in the solvation energy when ions permeate. In all the cases $pH = 1$ and pKa: (1) -2; (2) 0; (3) 2; (4) 3; (5) 4. Dashed lines correspond to the fraction of molecules in the deprotonated state at OHP, $f(d_{OHP})$. The six sets of plots are arranged in two columns and three rows. The columns correspond to values of $\dfrac{\varepsilon_{IHP}}{\varepsilon_M \kappa_M d_{OHP}}$. The rows correspond to values of $\dfrac{M}{2Zn}$.
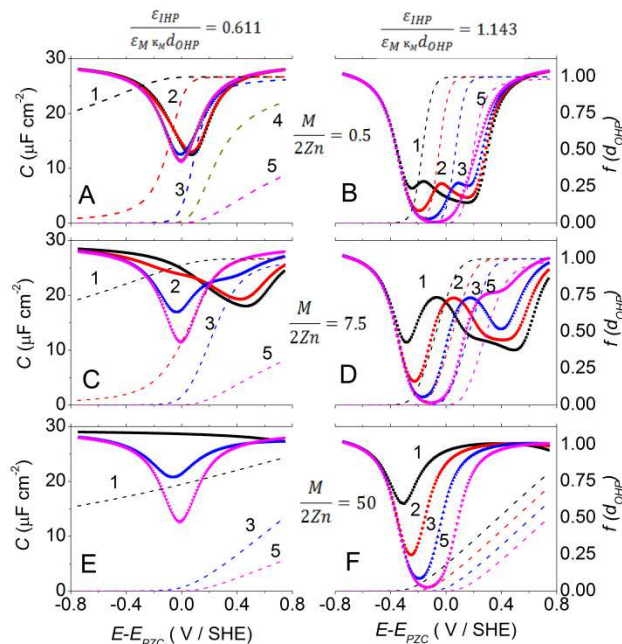
Curves in Fig. 3–2 are arranged in the following way: columns correspond to values of $\frac{\varepsilon_{IHP}}{\varepsilon_M \kappa_M d_{OHP}}$, while the rows correspond to different values of $\frac{M}{2Zn}$. For a given $\frac{\varepsilon_{IHP}}{\varepsilon_M \kappa_M d_{OHP}}$ and $\frac{M}{2Zn}$, a set of curves are presented as a function of the *pKa*, at constant *pH* = 1. In general, C_T–*E* curves have a complex response. Most of them reach a minimum value close to ϕ_{EQ}, but in few cases even two local minima can occur. In the cases when $f(d_{OHP}) \to 0.5$ in the vicinity of ϕ_{EQ}, a local maximum in the capacitance appear, even at low *pKa*, when the dissociation process is thermodynamically more favored (curve 1 in Figs. 3–2B and D). As expected from Eqn. (3.11), the effect of change in the solvation energy is more noticeable for lower membrane dielectric constants (Figs. 3–2B, D and F), and for smaller ions' size, because the constant energy barrier in these cases is larger, *i.e.* for $\mathcal{E}_P$ = 35, ΔW_{H+} = 0.047 and ΔW_{B-} = 0.024, while for $\mathcal{E}_P$ = 10, ΔW_{H+} = 0.305 and ΔW_{B-} = 0.152 V.

Figure 3-3 shows the local potential at d_{OHP} as a function of ϕ_E for curves in Fig. 3–2. As can be seen, when including the change in the solvation energy into the model, even at negative potentials the presence of the membrane increases the absolute value of the OHP potential, $|\phi_M(d_{OHP})|$, and thus, also decreases the electron transfer (ET) rate of electrochemical reactions (ECRs) at these potentials. Anyway, although coions' permeation increases the potential drop close to the surface, at any $\frac{M}{2Zn}$ value if $f_{EQ} < 1$, the ET's inhibition is stronger for $\phi_E > \phi_{EQ}$. In contrast, as explained before [171], at high $\frac{M}{2Zn}$ and low (*pH-pKa*) values the overall ET rate actually increases, especially at positive potentials. This is more important when the change in the solvation energy is considered, and particularly at high membrane dielectric constants (curve 1 in Figs. 3–3C and E).

Figure 3-3: Local potential at OHP, ϕ_{OHP}, as a function of the applied electrode potential, *E*, for systems in Fig. 3–2. The numbering of the curves are the same as in Fig. 3–2. Dashed lines correspond to theoretical curves derived from the original model [171].
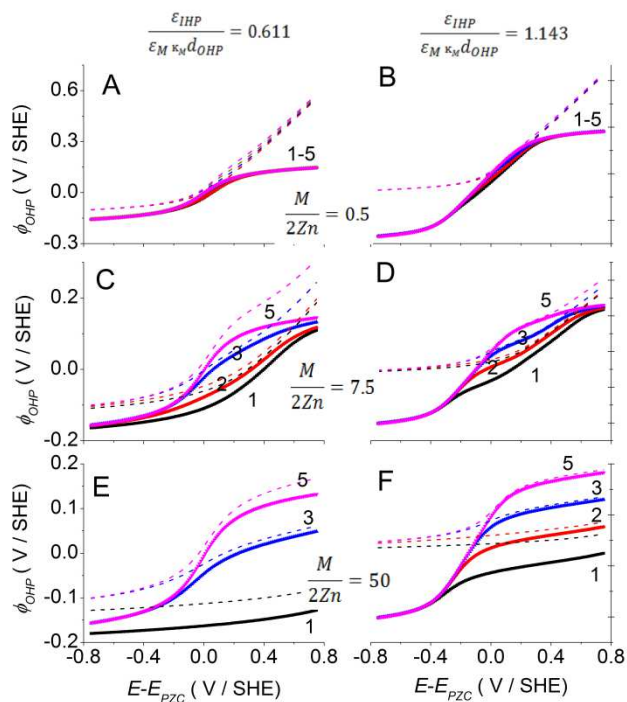
Interaction between ions and polarization charges. The interaction free energy of an ion inside a pore is also affected by its interaction with ions and with the polarization charge, induced by the ion itself at the interface between the membrane matrix and the solution inside the pore. Figure 3-4 shows C_T as function of (*pH-pKa*) and the electrode potential, when including these interactions into the model, calculated by Eqns. (3.5) and (3.12), respectively. Besides, because ion electrostatic interactions depend on the electrode potential, the change in the total interaction energy at OHP, $\Delta W_i^M(d_{OHP})$, is also included in Fig. 3–4. Finally, some C_T–E profiles when both interactions are included into the model, *i.e.* the change in the solvation energy when ions permeate and the ion-ion and ion-image charge interactions, are depicted in Figure 3-5. For all curves φ_{H+} = 0.64 and φ_{B-} = 0.36.

Figure 3-4:   Interfacial capacitance, C_T, for an electroinactive membrane, with acid/base groups, as function of (*pH-pKa*) and electrode potential, including interactions between ions and polarization charges. The numbering of the curves are the same as in Fig. 3–2. Dashed lines correspond to the change in the total interaction energy at the OHP, $\Delta W_i^M(d_{OHP})$. Arrows highlight where $f(d_{OHP})$ = 0.5.
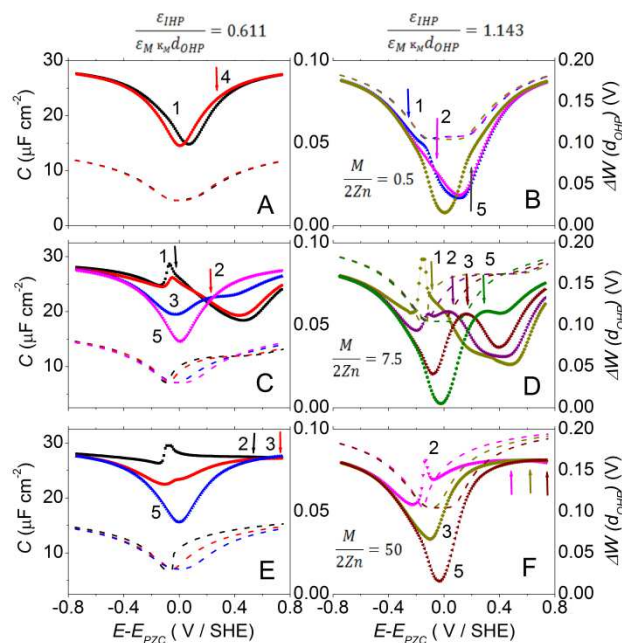
Curves in Figs. 3–4 and 3–5 are similar to those depicted in Fig. 3–2. However, when ion electrostatic interactions are taken into account, capacitance maxima may appear not only due to the acid/base dissociation process, but also because of the change in the total interaction energy with the applied potential (Fig. 3–4). From simulations, it is seen that this latter mainly comes from deviations from ideality due to ion-ion Coulomb interactions, because ion-polarization charge interactions are calculated negligible. The small radius of membrane pores and the strong molecular orientation close to the electrode surface make the pore solvent dielectric constant approach that of the membrane, reducing the effect of "image forces" within the pores while increasing the solvation energy barrier [16,173]. In addition, image charges are also screened in electrolyte solutions due to EDLs [16,173].

Figure 3-5: Interfacial capacitance, C_T, for an electroinactive membrane, with acid/base groups, as function of (*pH-pKa*) and electrode potential, including both interactions between ions and polarization charges and the change in the solvation energy when ions permeate. A. $\frac{M}{2Zn}$ = 7.5. B. $\frac{M}{2Zn}$ = 50. (a) $\frac{\varepsilon_{IHP}}{\varepsilon_M \, \kappa_M \, d_{OHP}}$ = 1.143; (b) $\frac{\varepsilon_{IHP}}{\varepsilon_M \, \kappa_M \, d_{OHP}}$ = 0.611 and (c) $\frac{\varepsilon_{IHP}}{\varepsilon_M \, \kappa_M \, d_{OHP}}$ = 0.448. The numbering of the curves are the same as in Fig. 3–2.
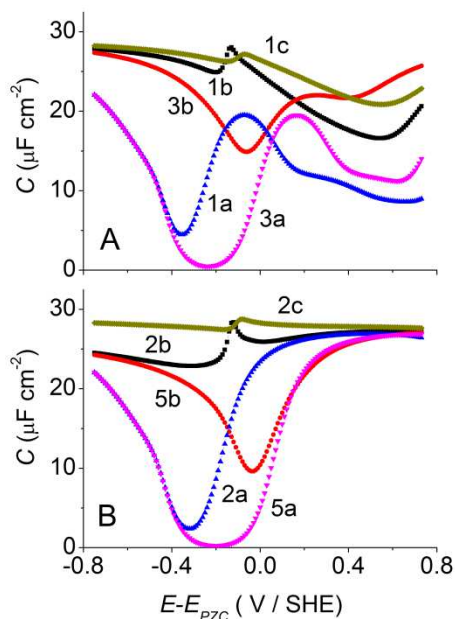
Additionally, some curves in Figs. 3–4 and 3–5 show sharp maxima in capacitance (see curves 1 and 2). This peak broadens, decreases in magnitude and shifts to more positive potentials when increasing the membrane dielectric constant (curves 1 and 2, Fig. 3–5). Sharp local capacitance maxima have been also reported at large C_{IHP} values with a simpler model [171]. In this sense, capacitance curves at a large C_{IHP} value when interactions between ions and polarization charges are taken into account, and also when the change in the solvation energy of permeating ions is included, are shown in Figures 3–6A and B, respectively. Under this condition, pretty sharp peaks are obtained, as consequence of both the acid/base dissociation process and the change in the total interaction energy with the applied potential. Indeed, although the exact shape of the curves will depend on the mathematical expression employed to calculate ions' interactions, the existence of an energy barrier, potential dependent will give rise to sharp capacitance maxima.

3.3.3 Model vs. Experiments: The Pt(111)/Nafion® Interface

Poly(perfluorosulfonic acid)-based ion-conducting membranes, like Nafion®, are the standard material for chlor-alkali electrochemical cells, PEMFC and other electrochemical devices, because of their hydrophilicity, selective permeability to cations, low resistance to current flow, and excellent thermal and chemical stability [5,6,14]. These are ionomers, *i.e.* copolymers of hydrophobic repeat units with a small fraction, no more than 10 mol% [17], of monomer units with an ionic functionality [14]. This hydrophilic/hydrophobic nature makes to hydrated ionomers basically a two-phase system on the scale about 4–10 nm in

diameter [8,14,17,18], with unique physical and morphological properties [8,17–19]. Specifically, Nafion® consists of a poly(tetrafluoroethylene) (PTFE) backbone with regular spaced long perfluorovinyl ether pendant side chains, terminated by a sulfonate ionic group [8,17,18].

Figure 3-6:   Interfacial capacitance, C_T, for an electroinactive membrane, with acid/base groups, as function of (*pH-pKa*) and electrode potential, when including: A. Interactions between ions and polarization charges. B. The change in the solvation energy when ions permeate and interactions between ions and polarization charges. The numbering of the curves are the same as in Fig. 3–5. M = 1.5 M and C_{IHP}.= 295 µF cm^{-2}.
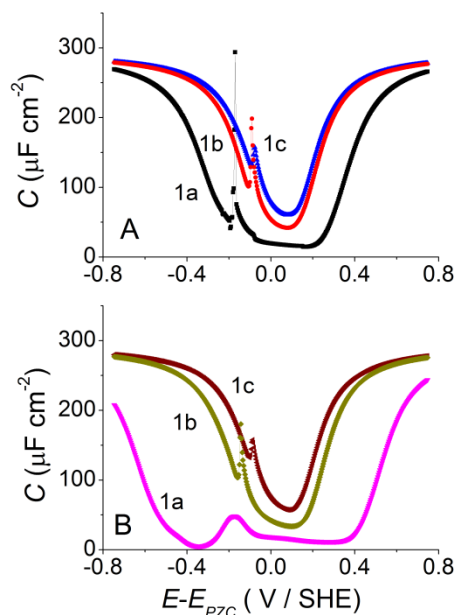
As discussed in Chapter 1, on Nafion® coated Pt(111) electrodes, both, H_{ads} and OH_{ads} adsorption regions can be still differentiated, but they are significantly modified, compared to a bare Pt(111) electrode. It was suggested that this could be possibly because a fraction of the surface is covered by hydrophobic PTFE backbone and becomes electrochemically inactive [20,25,67,78]. In addition, a current peak, *pH* dependent [67], between ~ 0.45–0.53 V appears in the CV, close to the electrode *PZTC* (Figs. 1–1 and 1–2) [68]. Attending to the Nafion®'s chemical nature and the similarity between the current peak on Nafion® covered electrodes, and the current peak for the (bi)sulfate adsorption on Pt(111) [65,110], recent works suggested a specific adsorption of Nafion® sulfonate groups on the surface [65–69]. However, although some IR spectroscopy-based techniques on polycrystalline Pt (PolyPt) have given support to this latter idea [22,164], several experimental results cannot be explained within that framework.

For example, while (bi)sulfate adsorption has a negative electronic effect for the ORR on Pt electrodes [183], on Nafion® coated Pt electrodes such inhibition does not occur. Instead, the ORR occurs with apparent activation energy lower than on bare Pt electrodes in HClO$_4$, but similar to trifluoromethanesulfonic acid (TFMSA), solutions [37], although both HClO$_4$ and TFMSA are non-adsorbing electrolytes [96]. Similarly, while on stepped surfaces, containing both {111} and {100} terraces, the current from (bi)sulfate adsorption on terraces depends on the terrace width [184], on Nafion® coated electrodes is not always possible to assign a current contribution for the apparent sulfonate adsorption on

terraces [68]. Moreover, the lack of a wavenumber blue-shift of both protonated and dissociated Nafion®'s sulfonic groups with increasing the electrode potential [20,22,67,78,164] would suggest that sulfonate anions are not specifically adsorbed but populated in the EDL [20,67,78]. Concomitantly, neutron reflectivity measurements shown that sulfonate-containing hydrophilic side chains are pushed away from the surface if Nafion® is in contact with a Pt surface, while in contact with a PtO monolayer, the hydrophobic backbone is pushed outward, and the hydrophilic side chains are in contact with the surface [40].

In addition, contrary to (bi)sulfate adsorption, on Pt(111)/Nafion® electrodes the current peak is an irreversible process, with a sharp peak in the positive-going scan and a small, and broad, current contribution in the negative one [65–69] (Fig. 1–2). Besides, the reversibility, peak position and sharpness of the process at 0.45 V are apparently *pH* dependents (Figs. 1–1 and 1–2). However when comparing with other studies, it is found that even under similar working conditions measured CVs differ [65,66,68,69]. This is clearly seen in Figs. 1–1 and 1–2, where two electrochemical responses for Nafion® films at *pH* = 2, differently prepared but evaluated under similar conditions, are shown. Indeed, previous studies recognized that reported experimental CVs are metastable and that Nafion® peaks shift to more positive potentials, broaden and decrease in magnitude when the electrode is left at open circuit for short periods (5–10 min) [68].

Undoubtedly there is a strong interaction between Pt and Nafion®, giving rise to preferential orientation, electric field driven, of membrane molecular units [20,67,78]. However it does not necessarily imply a specific adsorption of Nafion® sulfonate groups on Pt surface. According to our model [171], capacitance maxima close to the electrode *PZC* may appear as consequence of the acid/base equilibrium of membrane ionic units. These current peaks may be sharp when ion–ion coulomb interactions and dielectric exclusion effects have an important role, for example in membranes with low dielectric constants and narrow pores (Figs. 3–4 and 3–5), and especially for electrodes with a large C_{IHP} (Fig. 3–6). Nevertheless, following the model [171], current responses of SPEM coated electrodes in positive and negative-going scans during voltammetric experiments should be the mirror image of each other, which is not seen in Figs. 1–1 and 1–2.

Sharpness and irreversibility may appear due to the existence of large surface hydrophilic/hydrophobic membrane domains [185], a phenomenon not included in our simulations, and the asymmetry/peak broadening observed on the negative-going scan relative to the positive sweep would reflect relaxation of these domains into a wider range of smaller domains after deprotonation of sulfonate groups [68]. Additionally, considering the long time needed to reach a membrane structure in equilibrium (>20 min) [67], irreversibility in Figs. 1–1 and 1–2 may also arrive because of quasi-irreversible, far from equilibrium, metastable states of Nafion films close to the interface, with a low hydration level induced or not by the electrode potential [101,102]. Hence, reported changes, when Nafion® coated electrodes are left at open circuit for short periods [68], would occur because $\mathcal{E}_P$ increases as the membrane hydrates, *i.e.* the current peak broadens, decreases in magnitude and shifts to higher potentials (Figs. 3–5 and 3–6). Peak shift can also occur because the membrane *pH* decreases when is being hydrated, since at higher *pH*s the maximum shifts towards negative potentials [171].

Under this view, membranes in equilibrium, with high $\mathcal{E}_P$, should only display small and broad current features close to the *PZC*. In addition, taking into account the limited water uptake and the restricted anion mobility in thin membranes [9,186–188], it is expected that

thicker membranes will reach equilibrium conditions faster and so, thin membranes are more prone to show sharp current peaks [65–69]. This would explain why current peaks for Nafion® coated Pt electrodes have not been always reported [27,41–43,70]. In agreement, initial studies on Nafion® covered Pt electrodes have reported reversible restructuring processes, strongly influenced by the polymer hydration level [21] and the electrode potential [67], that influence the entire electrochemical response of the Pt/Nafion® interface and the electron transfer rate of the electrochemical reactions taken place on it [41–43]. It has been also shown that thin-film confinement can strongly affect both the structure and properties of Nafion® [9,186–188].

From the above discussion, it is clear that including a more refined expression to calculate the ion partitioning at the SPEM/solution interface can explain most of the experimental results reported for the Pt(111)/Nafion® interface, without considering specific adsorption of membrane anions on the electrode surface. In this sense, the proposed model can help to shed light on the molecular-level structural description of metal/SPEM interfaces. Nevertheless, the complexity of the system is huge and many factors play an important role. In consequence, a great effort still needs to be done, in order to obtain a full knowledge of the transport and charge transfer processes at the electrode/SPEM/solution interfaces.

3.4 Conclusions

In this work, a model for the differential capacity and the potential distribution at interface between an electrode modified by a polymer solid electrolyte membrane and an electrolyte solution is presented. The model includes counterions' and coions' permeation from the solution and considers the ion partitioning equilibrium at the SPEM/solution interface, as a function not only of the Donnan equilibrium, but also the steric exclusion, the change in the solvation energy that the ions face when moving from the favorable high dielectric environment of water to the unfavorable low dielectric of the membrane and the interaction between ions and the polarization charges, induced by ions themselves at the dielectric boundary between the pore walls and the pore-filling solution.

The proposed model can help to shed light on the molecular-level structural description of the metal/SPEM interface. Results show a strong coupling between the acid/base properties of the film, the change in the total interaction energy and the applied electrode potential. In some cases, a voltammetric current peak may arise from the reversible, electric field-driven, deprotonation of the acid/base membrane group, although the films is localized at the Outer Helmholtz Plane. In addition, at low dielectric constant inside membrane pores, $\mathcal{E}_P$, sharp peaks can be obtained, which broaden, decrease in magnitude and shift to more positive potentials when increasing $\mathcal{E}_P$. These peaks can be even sharper if the capacitance at the Inner Helmholtz Plane, C_{IHP}, is large.

Finally, the predictions of the model are discussed in light of recent experimental data obtained on Nafion® covered Pt(111) electrodes, providing a theoretical basis for qualitative electroanalyses of these systems. In this context, most of the experimental results reported for this system can be explained, without considering specific adsorption of membrane anions on the electrode surface. Nevertheless, the complexity of the system is huge and many factors play an important role. In consequence, a great effort still needs to be done, in order to obtain a full knowledge of the transport and charge transfer processes at the electrode/SPEM/solution interfaces.

4. Mean Field Approximation of Langmuir-Hinshelwood CO-surface Oxidation Considering Lateral Interactions[4]

The mean field approximation to model the CO electrocatalytic oxidation on metal surfaces, including attractive and repulsive *effective* lateral interactions between the species, is employed. Adsorbed CO reacts with adsorbed OH from water dissociation through a Langmuir–Hinshelwood mechanism. Simulated results suggest alternative explanations to experimental observations during CO stripping oxidation on different electrodes by potential step chronoamperometry or voltammetry. Even though the model ignores higher order interactions, such as three-body or long-ranged interactions, the results extend the conceptual framework for transient kinetics and stripping voltammograms for CO oxidation on metallic surfaces or any other electrochemical Langmuir–Hinshelwood reaction. In spite of the high level of simplicity, the model is a promising tool for the understanding of the electrocatalytic activity and results were qualitatively compared with experimental results.

4.1 Introduction

CO surface oxidation and adsorption reactions have been one of the cornerstones of surface science and one of the most intensively studied processes in electrocatalysis. Understanding the mechanisms and kinetics of these reactions is of considerable interest and vital for a proper optimization of low temperature fuel cells [189].Over the last decades, there have been extensive studies on CO adsorption on Platinum (Pt) surfaces [72,93,189–196]; however, the CO oxidation reaction mechanism is still under debate and some essential aspects of this reaction demand further investigations.

It is well established that CO oxidation involves a surface reaction between adsorbed CO (CO_{ads}) and oxidized surface species located at an adjacent site on the surface: the Langmuir–Hinshelwood (LH) scheme or reactant pair [71]. *In situ* electrochemical measurements using Scanning Tunneling Microscopy (STM), Fourier Transform Infrared (FTIR) [111,190,197], and information obtained from emersed electrodes in Ultra High Vacuum (UHV) [198], have yielded a wealth of structural data of CO adsorption on Pt single–crystal electrodes. However, it has remained relatively unclear how these microscopic structural features, or more generally the distribution of CO_{ads} on the

electrocatalytic surface, affect the overall macroscopic electrocatalytic activity [93,199,200].

Two different models have been mainly proposed to describe the kinetics of the CO electrocatalytic oxidation. The first approach assumes that the reaction, in the monolayer (ML) of CO_{ads}, proceeds at a perimeter of water islands containing adsorbed hydroxyl species (OH_{ads}), coming from water dissociation. The reaction is then controlled by the Nucleation and Growth (N&G) of these islands [93,190–192,200–202], as it was confirmed by spectroscopic measurements [91,111,190,203–205]. The second model is based on a Mean–Field Approximation (MFA) [72,193–195,206]. It assumes a fast surface diffusion of CO_{ads} and OH_{ads} and a perfect species mixing on the electrode surface. The validity of this model has been claimed on accurate fittings of experimental current transients [193–195,207,208]. This model was recently modified considering that the oxidation reaction proceeds at specific surface sites, like surface defects, kinks and/or edges. Therefore, CO_{ads} and OH_{ads}, diffuse on the surface towards the reaction zone [195]. This model is described in detail in the literature (*e.g.* refs 196, 209 and 210).

Fast surface diffusion and island formation do not necessarily exclude each other and both phenomena may occur concomitantly if lateral interactions between reactant particles are considered [189]. Physical properties of CO_{ads} molecules are different from those the other surface adsorbates, like water (H_2O_{ads}) and anion species, such as OH_{ads} and adsorbed HSO_4 ($HSO_{4,ads}$). Hydrogen bonds between these latter species, along the surface, are considerably stronger than CO-CO lateral interactions [93,211] and so, the formation of these bonds may or may not result in CO segregation, considering that electrochemical oxidation is usually analyzed at room temperature. The influence of all these interactions between adsorbates on the kinetics of CO oxidation will determine its surface structure, adsorption/desorption kinetics and the chemical reaction dynamics. This was recently suggested by CO oxidation studies on Nafion® covered Pt(111) electrodes [67]. The "*effective*" interactions inside the adlayer may be attractive or repulsive, depending on the balance between inter–particle and intra–particle interactions [212–214].

There are extensive theoretical works on the effect of lateral interactions on electrochemistry [212–222]. However, there are not many studies regarding this effect on the CO electrocatalytic oxidation reaction. Main theoretical efforts to simulate various kinetics aspects of this reaction treat adsorbed reactants as Langmuir particles: no lateral adsorbate-adsorbate interactions [72,223–228]. Nevertheless, Zhdanov and Kasemo simulated a two particle system, A and B, with B–B attractive interactions in an attempt to extend these previous studies [189]. It was shown that adsorbate–adsorbate lateral interactions affect the transient potential steps for CO oxidation on Pt single crystals. Indeed, the reaction kinetic may be accompanied by CO_{ads} segregation employing realistic values of these interactions (~4.2 kJ/mol), despite a fast CO diffusion over the surface.

In this work, the effect of "*effective*" lateral CO–CO interactions on the CO electrocatalytic oxidation kinetics over metal surfaces is studied. A LH mechanism between CO_{ads} and OH_{ads}, resulting from previous water dissociation, is used. Averaged lateral interactions that depend on CO coverage are included through the MFA formalism [73]. Although the model ignores higher order interactions, like three–body and long–range interactions, results are useful for a qualitative understanding of the CO oxidation kinetics and other electrochemical LH reactions. In addition, this MFA model will serve as the foundation of a Dynamic MC model that will be published elsewhere [229].

The manuscript is organized as follows: in section 2, the reaction kinetic model is described as well as the system equations based on the MFA, also called in electrochemistry as the Frumkin approximation [1,215]. In Section 3, results start with the non-interacting model, continuing to systems with attractive and repulsive interactions. The results are presented in terms of stripping voltammetry and chronoamperometry. Experimental data are given in order to provide comparison with numerical results. The manuscript ends with a summary of the most important observations and conclusions.

4.2 The reaction model and the LH-MFA formalism

The basic features of the model are described within this section (a detailed picture of it is given in Ref. 72). As mentioned before, the reactant pair model for the electrochemical CO oxidation in acidic solutions is widely accepted [71]. In it, the reaction scheme is described in terms of the LH mechanism with participation of adsorbed oxygen–containing species. Nevertheless, the exact nature of these species and the interpretation of the reaction kinetics are still under debate [189,195,230,231]. The most likely oxygen donor candidates have been H_2O_{ads} and OH_{ads}, however recent experimental works suggest that atomic oxygen (O_{ads}) could be another suitable species, which would imply novel paradigms for electrooxidation reactions [232–234]. In the present model, considering that the formation of the oxygen-containing species and the CO oxidation are potential dependent reactions [72], OH_{ads} will be considered as the reactive oxygen–containing species, resulting from water dissociation. The reaction model is as follows [72]

$$H_2O + * \xrightleftharpoons[]{k_1, k_{-1}} OH_{ads} + H^+ + e^- \tag{4.1}$$

$$CO_{ads} + OH_{ads} \xrightarrow{k_2} CO_2 + H^+ + e^- + 2 * \tag{4.2}$$
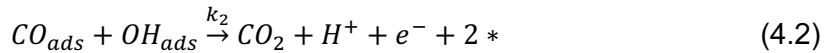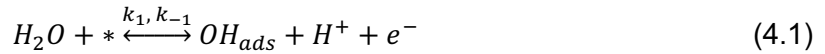
where * denotes a free surface site (or H_2O_{ads}) and subscripts "*1*", "*-1*" and "*2*" refer to the reactions of OH adsorption, OH desorption and CO oxidation, respectively. The model considers two reactant species (or three if empty sites are interpreted as H_2O_{ads}). This simplification avoids complications contained in complete schemes of CO oxidation, which may include multiple adsorbed species besides CO_{ads} and OH_{ads}, such as $HSO_{4,ads}$ [228]. For typical electrochemical processes, when coverage effects are considered, the corresponding rate constants for the reactions in Eqns. (4.1) and (4.2) are given by [1,216]

$$\mathrm{k_{OH,ads}} = k_1 = k_1^0 \exp\left(\frac{\beta_1 FE}{RT}\right)\exp\left(\frac{\gamma_1 f_1(\theta_T)}{RT}\right) \tag{4.3}$$

$$\mathrm{k_{OH,des}} = k_{-1} = k_{-1}^0 \exp\left(-\frac{(1-\beta_1)FE}{RT}\right)\exp\left(-\frac{(1-\gamma_1)f_1(\theta_T)}{RT}\right) \tag{4.4}$$

$$\mathrm{k_{CO_2,des}} = k_2 = k_2^0 \exp\left(\frac{\beta_2 FE}{RT}\right)\exp\left(\frac{\gamma_2 f_2(\theta_T)}{RT}\right) \tag{4.5}$$

where *β$_i$ = 0.5* are symmetry factors for electron-transfer reactions, *γ$_i$ = 0.5* are Brønsted factors, specifying to which extent the transition state for adsorption/desorption/reaction is influenced by the interactions between the species, *E* is the electrode potential, *f$_i$(θ)* is a function to describe the variation of the heat of adsorption of the species with the total coverage [216], *F* is the faraday constant, *R* is the ideal gas constant and *T = 300* K is the temperature. The reaction rate constants *k$_1$⁰*, *k$_{-1}$⁰* and *k$_2$⁰* correspond to the low–coverage limit and they are independent of lateral interactions. All of them have dimensions of

reciprocal seconds. In addition, rate constants k_1^0 and k_{-1}^0 include water and proton concentrations at the surface, respectively.

The exact form of $f_i(\theta)$ in Eqns. (4.3) to (4.5) is not known [216–218]. Assuming a linear dependence of the heat of adsorption with coverage, $f_i(\theta)$ can be written in the MFA frame considering empty sites as H_2O_{ads}, as follows

$$f_1(\theta_T) = \left(\epsilon_{CO/OH} + \epsilon_{W/W} - \epsilon_{CO/W} - \epsilon_{OH/W}\right)\theta_{CO} + \left(\epsilon_{OH/OH} + \epsilon_{W/W} - 2\epsilon_{OH/W}\right)\theta_{OH} \quad (4.6)$$

$$f_2(\theta_T) = \quad (4.7)$$

$$\left(3\epsilon_{CO/W} + \epsilon_{OH/W} - 2\epsilon_{W/W} - \epsilon_{CO/CO} - \epsilon_{CO/OH}\right)\theta_{CO} + \left(3\epsilon_{OH/W} + \epsilon_{CO/W} - 2\epsilon_{W/W} - \epsilon_{OH/OH} - \epsilon_{CO/W}\right)\theta_{OH}$$

where $\epsilon_{i/j}$ is the interaction energy between molecule i and molecule j when they occupy neighboring sites on the surface and θ_i is the average coverage of the species i (with W stating for water molecules). Equations (4.6) and (4.7) highlight that even for the simplest case $f_i(\theta)$s are function of several, poorly defined, unknown parameters. For example, OH_{ads} formation on metal surfaces is a complex process [235], even in the case of mono-crystalline surfaces [179]. Density Functional Theory (DFT) calculations have shown that $\epsilon_{OH/OH}$, $\epsilon_{OH/W}$ and $\epsilon_{W/W}$ energies are highly directional interactions, *i.e.* they can be strongly repulsive or attractive depending on the surface angle between the new OH_{ads} molecule to be formed and the already adsorbed H_2O_{ads} and OH_{ads} [211]. Hence, this feature makes them too complicate to be fully described in theoretical models.

Macroscopically, however, lateral interactions between the different species on the surface may give rise to adsorbate-adsorbate correlations and even island formation, which in turn, increases or decreases the overall oxidation reaction rate. In the MFA, surface patterns cannot be reproduced and only its effect on the oxidation reaction rate can be approached. Besides, during stripping experiments OH_{ads} can be only generated in empty sites left by CO_{ads}. Thus the overall effect of lateral interactions would be enhance or reduce the total OH_{ads} formation rate. In order to keep the model as simple as possible, with a measurable physical meaning and close to observable phenomena, the approach employed by Zhdanov and Kasemo is also used here [189], where, as a first approximation, $f_i(\theta)$ are given by

$$f_1(\theta_T) = 0 \quad (4.8)$$

$$f_2(\theta_T) = \epsilon_{CO-CO}\theta_{CO} \quad (4.9)$$

where ϵ_{CO-CO} represents an "*effective*" interaction energy inside the adlayer between CO–CO molecules that occupy neighboring sites on the surface. In situations when $\theta_{OH} \to 0$ ($k_1 \ll k_2$ or $k_1 \ll k_{-1}$) or $\theta_{OH} + \theta_{CO} = 1$ ($k_2, k_{-1} \ll k_1$). Eqns. (4.6) and (4.7) become only functions of θ_{CO} and simulations with the definition in Eqn. (4.9) accurately describe the system. In addition, when $\theta_{OH} + \theta_{CO} = 1$ and ϵ_{CO-CO} is repulsive, the model reproduces the chronoamperometric transients calculated for the reductive stripping of NO adlayers at Pt single crystal [236].

The total current density, due to reactions in Eqns. (4.1) and (4.2), is given by Faraday's law (one electron, e^-, per reaction)

$$j = e_0(v_1 - v_{-1} + v_2) \quad (4.10)$$

where v_j denotes the rate of the j-th reaction (in cm^{-2} s^{-1}). The MFA expressions for these reaction rates are given by

$$v_1 = \Gamma_s k_1 (1 - \theta_{OH} - \theta_{CO}) \tag{4.11}$$

$$v_{-1} = \Gamma_s k_{-1} \theta_{OH} \tag{4.12}$$

$$v_2 = \Gamma_s Z k_2 \theta_{OH} \theta_{CO} \tag{4.13}$$

where Γ_s is the number of surface sites per cm^2 ($\approx 1.32 \times 10^{15}$ for a Pt(100) surface) and Z = 4 is the number of nearest neighbors (*nn*) on a square lattice. Similar models on triangular lattices give qualitatively similar results [189,219]. Quantitative differences are related to the number of *nn* sites, being *nn* = 6 for triangular lattices. Therefore, the effect of lateral interactions in the ground state on the oxidation rate will be larger [219]. Although this model cannot be used to understand the detailed structural features of CO adsorption at metal/electrolyte interfaces, it is able to provide insights about the importance of microscopic features.

The dynamics of θ_{CO} and θ_{OH} is given by the following differential equations:

$$\Gamma_s \frac{d\theta_{OH}}{dt} = v_1 - v_{-1} - v_2 \tag{4.14}$$

$$\Gamma_s \frac{d\theta_{CO}}{dt} = -v_2 \tag{4.15}$$

As mentioned, the present model includes *average* lateral interactions through the MFA formalism [73]. Therefore the effect of repulsive or attractive short-range interactions will be overestimated or underestimated depending on the reaction process. This is an intrinsic feature of the MFA since adsorbate-adsorbate correlations, which could reduce or increase the effect of *nn* lateral interactions, are not taken into account. The "*effective*" lateral interactions used in this work range from +0.1 (repulsive) to -0.1 eV/atom (attractive), equivalent to ca. ±9.6 kJ/mol. Following previous studies [72,224,227], rate constants for OH adsorption and desorption are chosen such that, at 20 mV s^{-1}, OH adsorption appears reversible (0.02 s^{-1} for adsorption and 10 000 s^{-1} for desorption), while the CO oxidation reaction will adopt different values. Hence, the potential axis used here is arbitrary.

The oxidation during a voltammetric potential scan or potential step of a pre–adsorbed amount of CO (sub–monolayer) onto the surface is considered without CO in solution. The initial CO coverage is 0.99 ML, unless stated otherwise. Experimentally, CO adsorption on Pt(111) and Pt(100) gives an absolute saturation coverage between 0.6 and 0.7 per Pt site [196,237]. In this work, the coverage is defined as the ratio of the absolute coverage to the absolute saturation coverage. Therefore, the relative coverage used in the calculations may be close to unity. For the simulations, coverages of 0.99 are considered as the saturation coverage.

Regarding the surface diffusion, using MFA equations implies that adsorbate diffusion is rapid. In conventional CO oxidation on Pt at metal/gas interfaces, CO diffusion is known to be fast, around 10^{-9} to 10^{-11} cm^2 s^{-1} at room temperature [238], with an activation barrier of ~0.3 eV [239]. In contrast, under electrochemical conditions, with deficiency of accurate experimental validation, CO diffusion is expected to be slower [230]. In the case of OH, usually its diffusion has been assumed to be fast [211,121]. Contrary, recent works have suggested that it could be the rate determining step (RDS) during the CO oxidation

[67,121]. The effect of CO/OH diffusion in the LH scheme, including lateral interactions, will be discussed in detail elsewhere [229].

4.3 Results and discussion

4.3.1 System without lateral interactions

Before studying the effects of the "*effective*" lateral interactions, the current response of the non–interacting model will be described. Koper *et al* [72], have studied this model by MFA and Dynamic Monte Carlo (DMC) simulations considering two different sets of rate constants: A *fast* rate, where the CO oxidation reaction is assumed to be faster than OH adsorption reaction, k_2 = 8.234x10^{-1} s^{-1}; and a *slow* rate, where the OH adsorption is faster than the CO oxidation, k_2 = 8.234x10^{-5} s^{-1}. Their work provided insights about the importance of microscopic features such as mixing, lateral diffusion, and island formation. Hence, the first set of results to be discussed in this paper will highlight their most important findings, as well as other important features of the reaction dynamics.

The most intriguing feature of the LH mechanism described by Eqns. (4.1) and (4.2), either during stripping voltammetry or potentiostatic step experiments, is the curved shape of the plots in Figure 4-1; where the oxidation peak potential, $E_{p,CO/OH}$, in the current–potential plane, j–E, as a function of the sweep rate, v, (Fig. 4–1A), and the current maximum time, t_{max}, in the current evolution, j–t profile, as function of the final potential, E_f, (Fig. 4–1B) are shown for different k_2 values. The analysis of the slopes in Fig. 4–1 should result in the Tafel slope [72,222], but in this particular case the interpretation of the slopes is not that straightforward. For slow scan rates (or low E_f) a slope of ≈ 40 mV is observed, while for fast v (or high E_f) it is ≈ 119 mV. Between these two values, a *transition* zone is observed with slopes between 70 to 110 mV.

Figure 4-1:   (A) Peak potential, $E_{p,CO/OH}$, as a function of the logarithm of the sweep rate, $log(v)$. (B) The logarithm of the time of the current maximum, $log(t_{max})$, as a function of the final potential, E_f; at different CO oxidation rate constants, k_2. Arrow indicates increasing k_2.
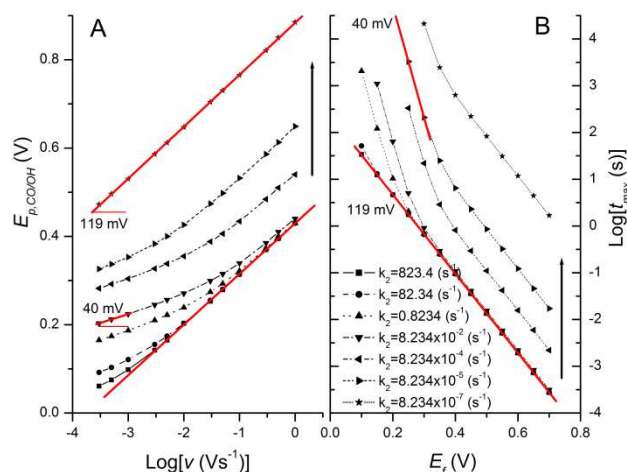
The change in slope is caused by the multistep character of the reaction mechanism, in particular through the desorption reaction [72]. At slow v (or low E_f) $E_{p,CO/OH}$ (or t_{max})

occurs in a potential region where OH desorption is important and competes with the CO oxidation reaction for the OH_{ads} species (parallel reactions). Contrary, for fast v (or high E_f) $E_{p,CO/OH}$ (or t_{max}) occurs in a potential region where OH_{ads} desorption can be neglected. Therefore, the fastest process can be either the OH adsorption or CO oxidation reactions (consecutive reactions).

CO oxidation rates between *fast* and *slow* values may show intermediate dynamics. If the CO oxidation rate is faster than a certain *moderate* value, $k_2 = 8.234 \times 10^{-3}$ s^{-1}, but slightly lower than the *fast* one, the transition zone shifts to greater v values (see Fig. 4–1A). In addition, at slow v the slope is higher than 40 mV and lower than 60 mV; whereas at fast v, the slope is between 90 and 105 mV (still lower than 119 mV). When k_2 is slower than the *moderate* set, the process is reverted and the transition zone now shifts towards lower v values. At *extremely slow* CO oxidation constant, $k_2 \leq 8.234 \times 10^{-7}$ s^{-1}, $E_{p,CO/OH}$ occurs at a higher potential than the OH_{ads} equilibrium and a single slope ~119 mV is observed (see ⋆ curve, Fig. 4–1A).

In contrast, even though the transition zone in the $log(t_{max})$ vs. E_f curve follows similar trends (movement) to those depicted in Fig. 4–1A, Tafel slope values do not change significantly when the CO oxidation constant is decreased (Fig. 4–1B). This difference may rely in the fact that, while in a *potentiostatic* experiment the overall reaction rate is only affected by changes in CO_{ads} and OH_{ads} coverages (the pre-exponential factor in Eqns. (4.9), (4.11) and (4.12)), in a *potentiodynamic* experiment it is modified by changes in both the coverage and the applied potential (the exponential factor in Eqns. (4.3), (4.4) and (4.5)). In consequence, Fig. 4–1B presents an abrupt change between the high and low Tafel regions.

When OH adsorption is the fastest process, the CO+OH oxidation reaction is the RDS and it controls the system response to changes in the applied potential. In this case, curves in Fig. 4–1 shift upwards, proportionally to k_2. Contrary, if the CO+OH oxidation reaction is the fastest process, OH adsorption is the RDS and curves shift downward to a limiting value. The OH adsorption and CO+OH oxidation reactions have the same potential dependence, hence for extremely high or low k_2 values the Tafel slope is always $2.3RT/\beta F \approx 119$ mV.

Stripping voltammetry. Anodic voltammetric sweeps of CO oxidation following the LH mechanism, without considering interactions, are characterized by a single and narrow reaction peak, $E_{p,CO/OH}$. This peak can be located before or after the OH adsorption/desorption peak, $E_{p,OH}$, (~ 0.34 V), depending on the sweep rate v and k_2 [72]. Figure 4-2 shows normalized CO stripping voltammograms (SV), j/j_{max}, as a function of k_2 and v for an initial CO coverage of 0.99 ML. The maximum current, j_{max}, from the stripping voltammogram is obtained at $E_{p,CO/OH}$. For situations where the initial CO coverage is lower than 0.99 ML (or higher amount of active sites), $E_{p,CO/OH}$ is shifted to lower potentials and has a wider shape [72]. Three different CO reaction rates are plotted in Fig. 4–2 to capture the complete spectrum of MFA predictions: *extremely slow*, $k_2 = 8.234 \times 10^{-7}$ s^{-1}; *moderate–slow*, $k_2 = 8.234 \times 10^{-4}$ s^{-1}, and *fast*, $k_2 = 8.234 \times 10^{-1}$ s^{-1}.

At *extremely slow* k_2, OH_{ads} adsorption is in a quasi-equilibrium state, $E_{p,CO/OH}$ occurs beyond the OH adsorption/desorption equilibrium and is symmetric bell shape for all v values. However, the full–width half–maximum (FWHM) value of the peak decreases at greater v (Fig. 4–2A). At *moderate–slow* k_2, the current is greater, the peak becomes narrower and $E_{p,CO/OH}$ shifts toward lower potentials. At slow v, its shape is no longer symmetric because the final part of the process is dictated by the OH adsorption reaction;

i.e. after reaching j_{max} the total reaction rate decreases and the peak collapses rapidly. At faster v, the FWHM slightly increases, although it is still narrower than in the previous case (Fig. 4–2B). At *fast* k_2, the OH_{ads} adsorption controls the entire oxidation process. Therefore, $E_{p,CO/OH}$ has an asymmetric shape if it occurs before $E_{p,OH}$. This is because the equilibrium OH_{ad} concentration is < 0.5 at $E_{p,CO/OH}$. Instead, if $E_{p,CO/OH}$ occurs at more positive potentials the curve recovers its symmetry but it is no longer bell shaped. For all v, $E_{p,CO/OH}$ is sharper and narrower than the other cases and FWHM slightly decreases at faster v (Fig. 4–2C).

Figure 4-2:   Normalized stripping voltammograms at different sweep rates, v, and CO reaction rate constants, k_2. The initial CO coverage is 0.99. (A) $k_2 = 8.234 \times 10^{-7}$ s^{-1} (B) $k_2 = 8.234 \times 10^{-4}$ s^{-1} (C) $k_2 = 8.234 \times 10^{-1}$ s^{-1}. Note that potential-axis is different in figures.
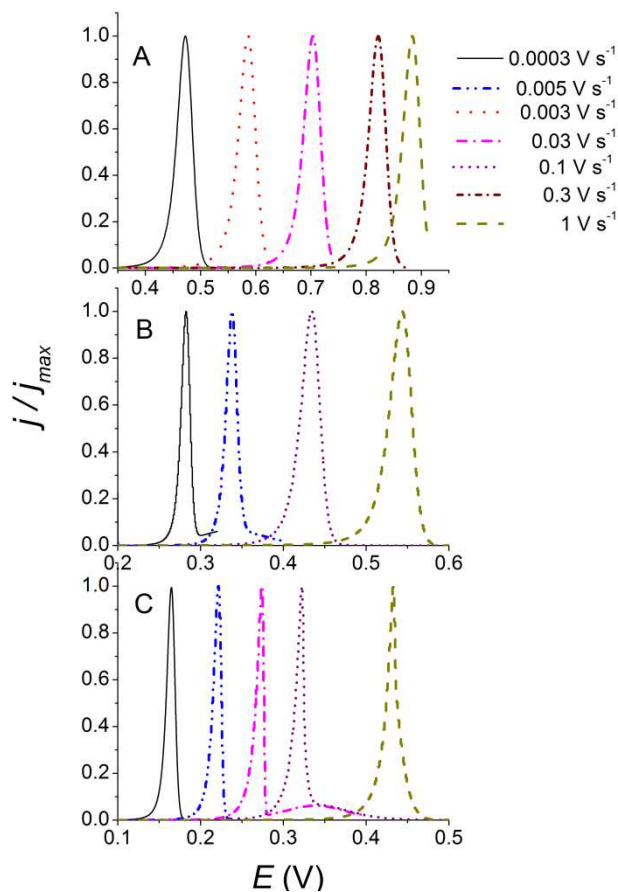
Potential step chronoamperometry. Transient kinetics provides details behind the reaction mechanism. Experimentally, they are observed after pre-adsorption of CO close to saturation and a subsequent potential step resulting in reaction (without CO adsorption) [1]. Figure 4-3 shows normalized current transients, j/j_{max}, after stepping from a potential at which a 0.99 CO monolayer is stable to a final potential, E_f. Normalizations are made for both scales, using j_{max} and its corresponding time, t_{max}. This figure represents most of all peak shapes predicted by the scheme described by Eqns. (4.1) and (4.2) under Langmuir conditions and the MFA.

Potential step simulations without interactions show a single maximum during the current evolution at any k_2 [72,236]. The j–t profile depends on the identity of the RDS and on the

final potential if k_2 is *fast* (Figs. 4–3A and B). For the *slow* reaction rate (*e.g.* Fig. 4–3D), OH_{ads} adsorption is at quasi–equilibrium and transients are practically symmetric in the entire range of step potentials. Under this conditions, using the same set of parameters the normalized current evolution can be fitted to a MF simplified model, despite the potential dependence of t_{max} with E_f (see ► curve, Fig. 4–1B). The MFA simplified model is defined as follows [193–195,207,208],

Figure 4-3: Normalized potential step current transients at different CO reaction rate constants, k_2, and final potentials, E_f. The initial CO coverage is 0.99. (A) k_2 =823.4 s^{-1}. (B) k_2 = 8.234x10^{-1} s^{-1}. (C) k_2 = 8.234x10^{-3} s^{-1}. (D) k_2 = 8.234x10^{-5} s^{-1}. Insets: Potential step current transients at different E_f: (a) 0.6 V, (b) 0.55 V, (c) 0.50 V and (d) 0.45 V. Note that current and time axes are different in insets.
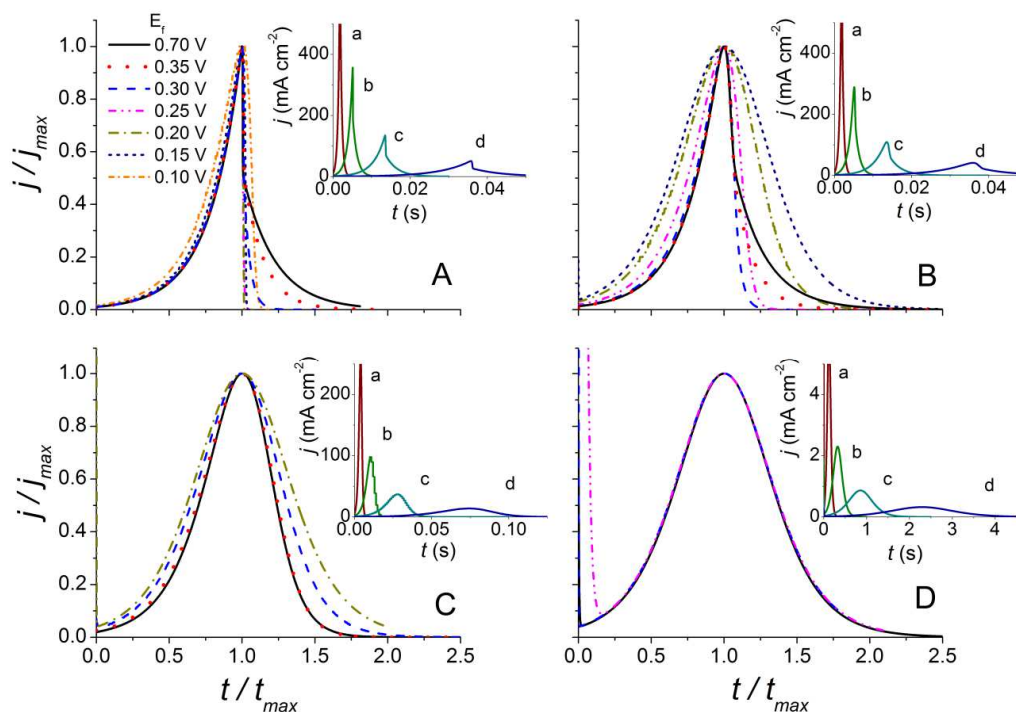
$$j(t) = \frac{Q k_2 exp(-k_2(t-t_{max}))}{[1+exp(-k_2(t-t_{max}))]^2}$$

(4.16)

where $j(t)$ is the current density, Q is the charge associated with the oxidation of CO adlayer in the main peak, t_{max} is the time of the maximum current and k_2 is the CO oxidation reaction constant rate. Equation (4.16) is obtained by assuming a reversible, fast equilibrium for the oxygen-containing species in Eqns. (4.1) and (4.2). Therefore, θ_{OH} is always proportional to $(1-\theta_{CO})$. In the case of Pt(111), this assumption seems reasonable since incipient oxidation of this surface is known to be reversible [193–195,207,208].

In addition, results in Fig. 4–3 indicate that at low E_f the transients for *moderate* and *fast* k_2 can be still fitted by the MF simplified approach, but including an E_f dependence on the normalized peak shape. However, at increasing E_f Eqn. (4.16) cannot accurately capture the slight, non–symmetric dynamics, which does not depend on E_f (Figs. 4–3C and B). At *extremely fast* CO oxidation rates, k_2 = 823.4 s^{-1}, the MFA equation fails to represent the

CO transients (Fig. 4–3A). The OH adsorption/desorption reaction is responsible for the abrupt fall after j_{max} is reached, especially at potentials lower than $E_{p,OH}$ where the equilibrium OH_{ads} concentration is low. These asymmetric transients in Fig. 4–3A cannot be obtained if OH_{ads} is always considered at equilibrium, as it was assumed in past works [189,223,236].

Experimentally, acid media chronoamperometric measurements for CO oxidation of saturated adlayers on Pt(111) and stepped surfaces, after double layer corrections (a high current at short times), are characterized by a current plateau followed by a main peak, and Tafel slopes between 59 and 80±4 mV have been measured for both regions on Pt(111) [193,194,208,240,241]. These Tafel slopes, around to 60 mV, have been interpreted for some authors in terms of a slow chemical step in the reaction scheme as the RDS in the whole mechanism [240,241].

Additionally, it has been widely accepted that the reaction in the main peak follows a LH dynamics with competitive adsorption of CO and OH [193,194,207,208,242,243]. However, the reaction at the current plateau has had different explanations. Some authors proposed an Eley–Rideal (ER) mechanism in the early stages of the oxidation [207,231]. This mechanism involves a solution–phase with H_2O as reactant species, indicating a *zero*-th reaction order in the oxygen donor [207,231]. Instead, Akemann *et al.* explained this dynamics as CO oxidation in the vicinity of defects and steps [243], whereas Lebedeva *et al.* suggested that the plateau is consistent with a LH mechanism where the initial CO–saturated adlayer relaxes, filling the empty sites during the early stages of the oxidation and maintaining a constant OH_{ads} (or H_2O_{ads}) coverage [193,194].

Similar to experimental transients, results in Fig. 4–3 show a non-zero current before the main peak. This current is higher for slower CO reaction rates. To clarify this dynamics, non-normalized *j–t* profiles at different $E_f > E_{p,OH}$ are given as inset to Fig. 4–3. As can be appreciated, the current transients contain a plateau followed by a main peak (see especially Fig. 4–3C). Thus, these experimental two regions may be also a consequence of the multistep character of the LH mechanism itself, and not due to two different mechanisms, ER or LH, nor CO–oxidation in the vicinity of defects [193,194,207,231,243]. In agreement with experiments, the current in the plateau region increases at higher E_f and *log(i)* follows the same trend than *log(t_{max})* for the reaction in the main peak (Fig. 4–1B). In addition, curves in Fig. 4–3A would suggest that, experimentally, k_2 is not extremely greater than OH formation.

For lower initial CO coverages (or higher amount of active sites), current transients qualitatively exhibit the same dynamics described above. Nevertheless, the current evolution only contains a portion of the ascending side of the peak and a tailing on the descending part of the transients is seen, Figure 4-4. These additional features are due to the existence of more free sites for OH adsorption and fewer CO molecules to be oxidized. In consequence, OH_{ads} fills up the empty sites in the adlayer and the reaction begins under higher initial OH_{ads} concentrations. Thus, j_{max} is shifted to lower times because the CO oxidation reaction occurs faster. Kinetic MC simulations that employ the active site concept have also been reported similar transients to those depicted in Fig. 4–4 [230].

At *extremely fast* CO oxidation rates, lower OH_{ads} concentrations are reached before the reaction begins and the current transient includes a bigger portion of the ascending side (Fig. 4–4A). Therefore, if $k_2 >>> k_1$, the OH_{ads} concentration is kept at low values and the reaction may inhibit itself, because the CO oxidation rate depends on both CO_{ads} and

OH$_{ads}$ concentrations, Eqn. (4.16). For *moderate–slow* CO oxidation constants, the transient contains an initial exponential contribution, in addition to the current decay before the peak (Fig. 4–4B). This current contribution comes from simultaneous OH$_{ads}$ adsorption and CO oxidation before OH species fills up all the empty sites in the adlayer. Contrary, at *slow* CO oxidation constant rate and $E_f > E_{p,OH}$, the exponential contribution is due to the OH$_{ads}$ adsorption, filling up all the empty sites in the adlayer (Fig. 4–4C).

Figure 4-4: Normalized potential step current transients, j/j_{max}, at different CO reaction rate constants, k_2, from a 0.7 CO initial monolayer to different final potentials, E_f. (A) $k_2 = 82.34$ s^{-1}. (B) $k_2 = 8.234 \times 10^{-4}$ s^{-1}. (C) $k_2 = 8.234 \times 10^{-5}$ s^{-1}.
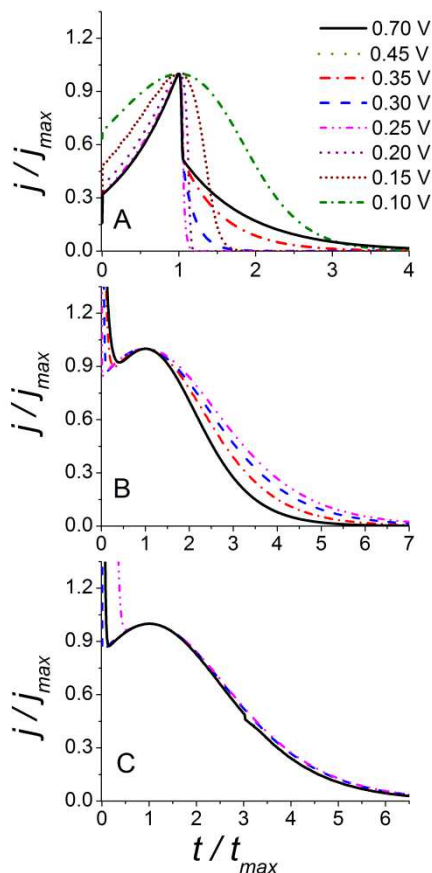
Recently, experimental current transients with an exponential contribution before the main peak have been reported during the CO oxidation on Pt(111) in alkaline media [242,244–246]. In those works, two different reaction mechanisms were proposed for the exponential decay and the main peak [242,246]. Results in Fig. 4–4 suggest that OH$_{ads}$ adsorption on active sites could be an alternative explanation, and it would imply higher amount of active sites for CO oxidation on Pt(111) in alkaline medium.

4.3.2 System including lateral interactions

Experimentally, it is well known that "*effective*" interactions between adsorbates may determine the system dynamics. For example, UHV studies have shown that while water and CO hydrophobically co-adsorb on Pt(111), giving rise to surface segregation, on

Rh(111) surfaces, instead, CO_{ads} and H_2O_{ads} adsorbed together produce more stable adlayers than when they adsorb alone, indicating net attractive $CO–H_2O$ interactions on this latter surface [120]. Hence, in UHV environments, different reaction kinetics for the oxidation of CO on these surfaces are expected, and probably in aqueous solutions too [120].

In agreement, while during stripping voltammetric studies of CO oxidation on Pt(111) and Pt(100) surfaces, an increase in the FWHM at faster *v*, Tafel slopes of 80 and 60 mV, respectively, and narrow and sharp peaks have been reported, the narrower the peak, greater the measured CO oxidation overpotential [199]. On Rh(111) and its vicinal surfaces, Rh[n(111)x(111)], contrarily, the presence of pre- and post-shoulders, as well as a pronounced tailing of the main oxidation peak have been published [247,248]. These latter features, commonly associated with adsorbate diffusion limitations on the electrode surface [247,248].

Similarly, while potentiostatic studies of CO oxidation on Pt(111) and its stepped surfaces, both in acidic [193,194] and alkaline media [242,244–246], have revealed symmetric transients that become slightly asymmetric at lower potentials, with a tailing in the descending part. On Rh(111) and its vicinal surfaces, however, although the same dynamics applies [248,249], potential step experiments in sulfuric acid at low E_f have also found a Tafel slope of ca. 45 mV and an important amount of CO_{ads} still adsorbed on the electrode when the transient current approaches zero, even though the CO oxidation on rhodium initially proceeds faster than on Pt. In consequence, in the latter case, a second electron transfer as the RDS has been suggested [248,249], and it was proposed that either the formation of surface deactivating species during the experiment or an anion effect would be responsible for such a result.

In addition, a central role of the "*effective*" interactions inside the adlayer, in the overall reaction kinetics, is also expected for the CO electrooxidation on Nafion® coated Pt(111) electrodes [67]. Nafion® is a solid polymer electrolyte (SPE) membrane widely used in polymer electrolyte fuel cells, characterized by a phase separation inside its structure. Hence, it may modify the entire environment close to the electrode surface. Fig. 1–8 depicts a typical cyclic voltammogram (CV) for the CO oxidation on Nafion® covered Pt(111). As discussed, the CO oxidation reaction at the Pt(111)/Nafion® interface takes place at higher potentials and in a sharper voltammetric peak than in the case of a bare Pt(111) electrode. It has been proposed that CO molecules are preferentially adsorbed over the surface close to the hydrophobic membrane region, while OH molecules can only adsorb close to the hydrophilic region. Thus, the membrane would promote island formation on the surface [67].

Once some experimental cases where the "*effective*" surface interactions may play an important role have been mentioned, the results of the model considering interactions between the molecules will be discussed in light of these findings. Normalized and non-normalized SVs for the CO oxidation reaction, taking into account lateral *nn* CO–CO interactions ($\epsilon_{CO–CO}$), at 50 mV s^{-1} are shown in Figure 4-5. Analogous to the non–interacting case, most of the voltammetric sweeps are characterized by a single peak before or after OH_{ads} adsorption. Indeed, similar SVs are calculated with different sets of parameters: k_2 and $\epsilon_{CO–CO}$ (curves 1, 6 and 7 in Figs. 4–5A and C). Therefore, finding solid experimental proof of "*effective*" attractive or repulsive interactions based only on the voltammogram shape (adsorption/desorption) is difficult and other experimental approaches are needed.

Figure 4-5:   Normalized stripping voltammograms at different k_2 and "*effective*" lateral interactions $\epsilon_{CO\text{-}CO}$. (A) Attractive interactions: k_2 = 8.234x10^{-2} s^{-1} and $\epsilon_{CO\text{-}CO}$ = -0.02 eV (2) - 0.04 eV (3), -0.06 eV (4), -0.10 eV (5); $k_2/\epsilon_{CO\text{-}CO}$ = 8.234x10^{-1} s^{-1}/-0.04 eV (6); 82.34 s^{-1}/- 0.10 eV (7). (B) Repulsive Interactions: k_2 =8.234x10^{-2} s^{-1} and $\epsilon_{CO\text{-}CO}$ = -0.05 eV (8); -0.10 eV (9); k_2 =8.234x10^{-4} s^{-1} and $\epsilon_{CO\text{-}CO}$ = -0.10 eV (10). (C) and (D) are the non-normalized stripping voltammograms of (A) and (B), respectively. Voltammogram in absence of interaction is also given (1) (solid line). The scan rate was 50 mV s^{-1}. Initial CO coverage 0.99 ML.
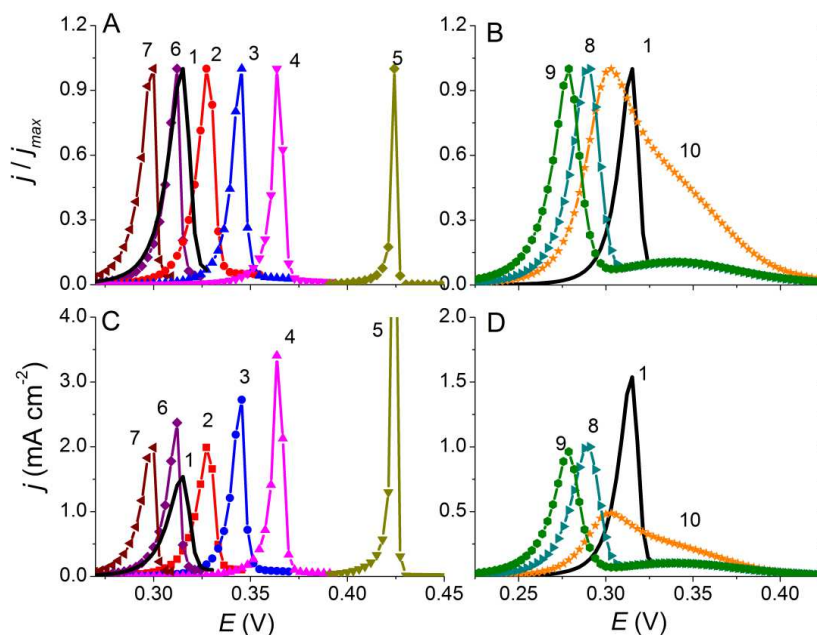
Attractive interactions. Stripping voltammograms, for the case of attractive interactions (negative values of $\epsilon_{CO–CO}$), are characterized by narrow and sharp peaks (Fig. 4–5C). At the same k_2, the voltammetric peak including the attractive interactions narrows, sharpens and shifts to higher potentials when decreasing $\epsilon_{CO–CO}$. The magnitude of these changes is proportional to the magnitude of the interactions (see curves 1 to 5 in Figs. 4–5A and C). Simulations in Fig. 4–5 when decreasing $\epsilon_{CO–CO}$ are similar to Fig. 1–8 when the Pt(111) surface is covered by an thin Nafion® film. Hence, it is highly possible that Nafion® membrane modifies the "*effective*" interactions between CO$_{ads}$–CO$_{ads}$, CO$_{ads}$– OH$_{ads}$ and OH$_{ads}$–OH$_{ads}$ molecules inside the adlayer on Pt(111), making them more "attractive" than in the case of a bare electrode. Differences in physical properties of adsorbed molecules could give rise to these "*effective*" interactions, *i.e.* while H$_2$O$_{ads}$/OH$_{ads}$ molecules form a stable network due to their attractive interactions, CO$_{ads}$– CO$_{ads}$ and CO$_{ads}$–H$_2$O$_{ads}$ interactions are repulsive [93,120,196].

Figure 4-6 shows CO stripping voltammetry for k_2 = 8.234x10^{-2} s^{-1} with $\epsilon_{CO–CO}$ = -0.02 eV and k_2 = 82.34 s^{-1} with $\epsilon_{CO–CO}$ = -0.1 eV, for different scan rates, 0.3 < v < 100 mV s^{-1} (for 50 mV s^{-1} see curves 2 and 7 in Fig. 4–5C). At any scan rate, peaks are highly asymmetric and sharp, with a steep rise and an abrupt descend once $E_{p,CO/OH}$ has been reached. Only when $E_{p,CO/OH}$ occurs in the potential region where OH$_{ads}$ adsorption occurs, $E_{p,CO/OH}$ is less asymmetric because OH adsorption contributes to the descending part of the peak once all the CO molecules have been consumed (the maximum current is reached), Fig. 4–6F. Contrary to the non-interacting system, when attractive interactions

are considered FWHM increases at faster scan rates, similar to what was reported for CO oxidation on Pt(111) and Pt(100) [199].

Figure 4-6:   Stripping voltammograms for (■) k_2/ϵ_{CO-CO} = 8.234x10^{-2} s^{-1}/-0.02 eV and (●) 82.34 s^{-1}/-0.1 eV, at different sweep rates, v. Initial CO coverage = 0.99 ML. For 50 mV s^{-1} see curves 2 and 7, Fig. 4–5C, respectively.
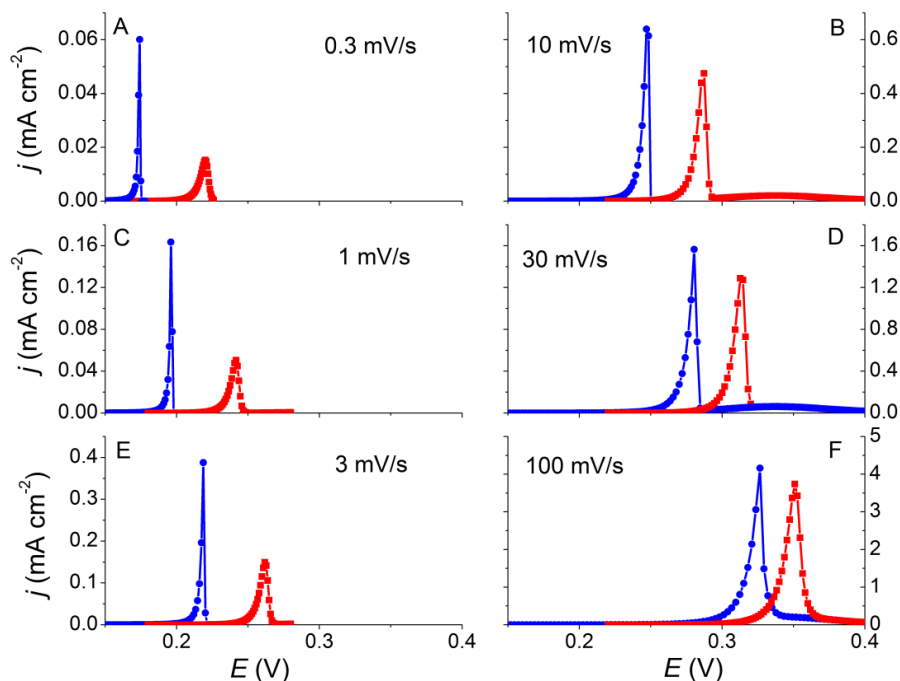
The peak potential, $E_{p,CO/OH}$, as a function of the sweep rate, v, considering attractive interactions, is shown in Figure 4-7A. As in the non–interacting case, the semi-logarithm dependence is non-linear and, in some cases, the transition zone is extended and slopes at slow v are higher than in absence of interactions. The slope depends on the dynamic inside the adlayer during the oxidation: at the beginning of the reaction, CO oxidation rate is slower than at the end, not only because there is a change in the applied potential but also because θ_{CO} decreases when the reaction proceeds. Slopes within 50 and 70 mV are observed for v < 30 mV s^{-1}, while at 3 < v < 100 mV s^{-1} slopes between 60 and 85 mV are obtained. In agreement with what was reported for CO oxidation on Pt (100) and Pt (111), respectively [199].

Figure 4-8 shows potential step current transients for two CO oxidation constants and attractive $\epsilon_{CO–CO}$ values. In this case, $j–t$ profiles are always asymmetric and the transients exhibit an extended plateau before the main peak takes place. This dynamics arrives because at the beginning of the CO oxidation OH molecules replace CO molecules, and the reaction rate is almost constant (no empty sites). If OH$_{ads}$ adsorption is the RDS, the descending part of the peak is governed by this equilibrium and the peak shape is asymmetric (Fig. 4–8A). If not, OH$_{ads}$ fills up the empty sites on the surface as soon as CO$_{ads}$ is oxidized and, because the reaction rate increases as θ_{CO} decreases, j_{max} is reached at θ_{CO} lower than 0.5 (Fig. 4–8B).

Contrary to results from stripping voltammetric simulations, the shape of the current transients, when attractive interactions are considered, are quite different than the

experimental current transients on Pt single crystals [193,194]. A possible explanation for this fact could be either adsorbate-adsorbate correlations or diffusional limitations inside the adlayer, which are more noticeable in potential step experiments and are not taken into account in our MFA model. In order to improve the model, Dynamic MC simulations for the same LH scheme, including lateral interactions and taking into account the effect of CO_{ads} and/or OH_{ads} diffusion will be discussed elsewhere [229]. Nevertheless, it is important to keep in mind that the model illustrated here is quite simply and it is far away from describing real experiments, which include many more phenomena.

Figure 4-7:   Peak potential, $E_{p,CO/OH}$, as a function of the logarithm of the sweep rate, $log(v)$. (■) k_2 = 823.4 s^{-1}, (●) 82.34 s^{-1}, (▲) 8.234x10^{-1} s^{-1}, (▼) 8.234x10^{-2} s^{-1}, (♦) 8.234x10^{-3} s^{-1}, (◄) 8.234x10^{-4} s^{-1}, (►) 8.234x10^{-5} s^{-1}. Filled symbols are when interactions are considered while empty symbols neglect them. (A) Attractive interactions. (B) Repulsive interactions.
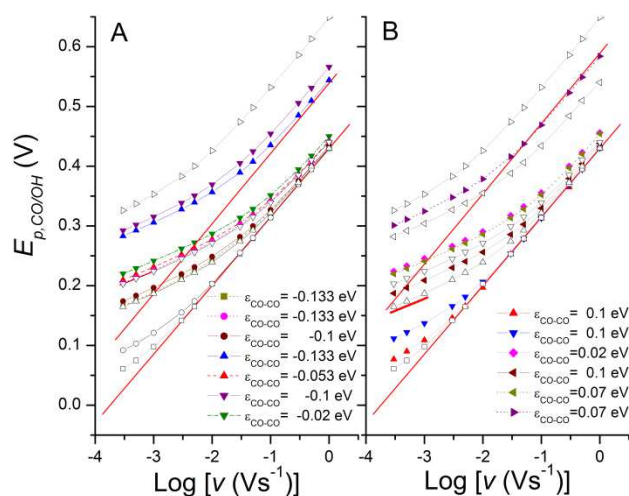
Figure 4-8:   Normalized potential step current transients at different final potentials, E_f. (A) k_2/ϵ_{CO-CO} = 82.34 s^{-1}/-0.1 eV. (B) 8.234x10^{-4} s^{-1}/-0.04 eV. Initial CO coverage = 0.99 ML.
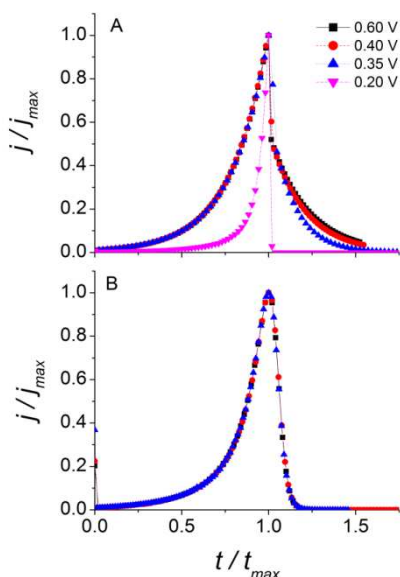
The time at which the maximum current is observed, t_{max}, as a function of E_f is shown in Figure 4-9A for different k_2 values and $\epsilon_{CO-CO} < 0$. For the sake of comparison the curves when no interactions are considered are also given. Similarly to simulations when interactions are not taken into account (Fig. 4–1B), with attractive interactions between particles non–linear Tafel plots are also obtained (Fig. 4–9A). However, the shape of the current transients in Figs. 4–3B and D is quite different to those ones for j–t profiles in Figs. 4–8A and B, respectively. While current transients with attractive interactions always have an asymmetric shape, in absence of interactions decreasing the final potential makes the transients symmetric.

Figure 4-9:   The logarithm of the time of the current maximum, $log(t_{max})$, as a function of the final potential, E_f. ($\bullet$) k_2 = 82.34 s^{-1}, ($\blacktriangle$) 8.234x10^{-1} s^{-1}, ($\blacktriangledown$) 8.234x10^{-2} s^{-1}, ($\blacktriangleleft$) 8.234x10^{-4} s^{-1}, ($\blacktriangleright$) 8.234x10^{-5} s^{-1}, ($\ohm$) 8.234x10^{-6} s^{-1}, ($\star$) 8.234x10^{-7} s^{-1}. Filled symbols are when interactions are considered while empty symbols neglect them. (A) Attractive interactions. (B) Repulsive interactions.
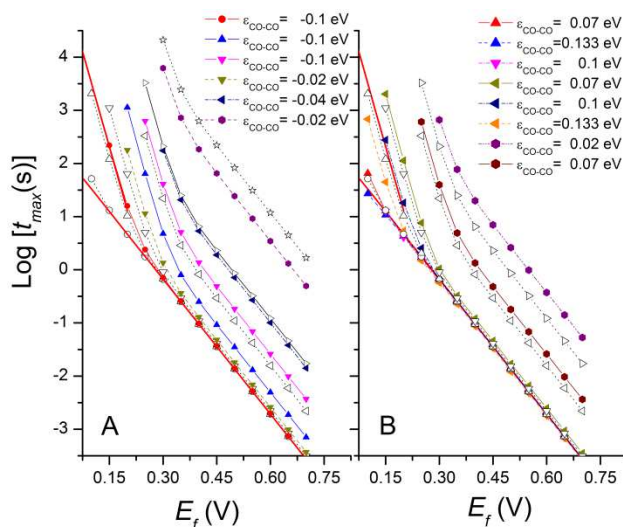

Tafel slopes between 45 to 60 mV and 118 mV are calculated from Fig. 4–9A at low and high E_f, respectively. This result demonstrates that Tafel slopes lower than 119 mV can be obtained for a pure LH mechanism, without considering a chemical step as RDS, as suggested in past works [240,241]. However, Tafel slopes higher than 119 mV, reported by Bergelin *et al* [207], and Love and Lipkowski [191] for CO oxidation on Pt(111) at high potentials, cannot be predicted under the present conditions.

Repulsive interactions. As mentioned, lateral interactions inside the adlayer are difficult to identify merely from stripping voltammetry measurements. However, in the case of a strong repulsion (0.1 eV) and a *moderate–slow* CO rate constant, k_2 = 8.234x10^{-4} s^{-1}, a weak splitting of $E_{p,CO/OH}$ occurs (curve 10 in Fig. 4–5D). This is a consequence of the continuous decrease of the oxidation rate as the reaction progresses (θ_{CO} diminishes). Therefore, if the difference between k_2 and ϵ_{CO-CO} values is large enough, $E_{p,CO/OH}$ in the SV will tends to split. On the other hand, including repulsive interactions between CO molecules broadens and shifts $E_{p,CO/OH}$ to lower potentials than those found in absence of interactions (see Figs. 4–5B and D). Nevertheless, and contrary to the case of attractive interactions, stronger repulsive interactions do not change significantly the SV: *e.g.* doubling the interactions only produces a small shift in the height and position of $E_{p,CO/OH}$ (Figs. 4–5B and D).

Figure 4-10 shows SVs for k_2 = 8.234x10^{-2} s^{-1} and ϵ_{CO-CO} = 0.1 eV, at different scan rates: 0.3 < v < 100 mV s^{-1} (for 50 mV s^{-1} see curve 9, Fig. 4–5D). At slow v, the SV shows a main peak, $E_{p,CO/OH}$, followed by a shoulder (Figs. 4–10A and B), which becomes a tail at the descending side of the peak at faster scan rates (Figs. 4–10C to D). For even more faster v, there is no tail on the peak, and $E_{p,CO/OH}$ is symmetric when it occur before, or after, the potential range for OH adsorption (Fig. 4–10E). Otherwise, $E_{p,CO/OH}$ is asymmetric (curve 9, Figs. 4–5D and 4–10F). Increasing the scan rate decreases FWHM, enhances the $E_{p,CO/OH}$ intensity and shifts it to higher potentials. Fig. 4–7B plots $E_{p,CO/OH}$ as function of v for repulsive interactions. In this case, calculated slopes are around 50 and 70 mV, for v < 30 mV s^{-1} and ca. 90 to 110 mV, for 3 < v < 100 mV s^{-1}.

Figure 4-10: Stripping voltammograms for k_2 = 8.234x10^{-2} s^{-1} and ϵ_{CO-CO} = 0.1 eV at different sweep rates, v. Initial CO coverage = 0.99 ML. For 50 mV s^{-1} see curve 9, Fig. 4–5F.
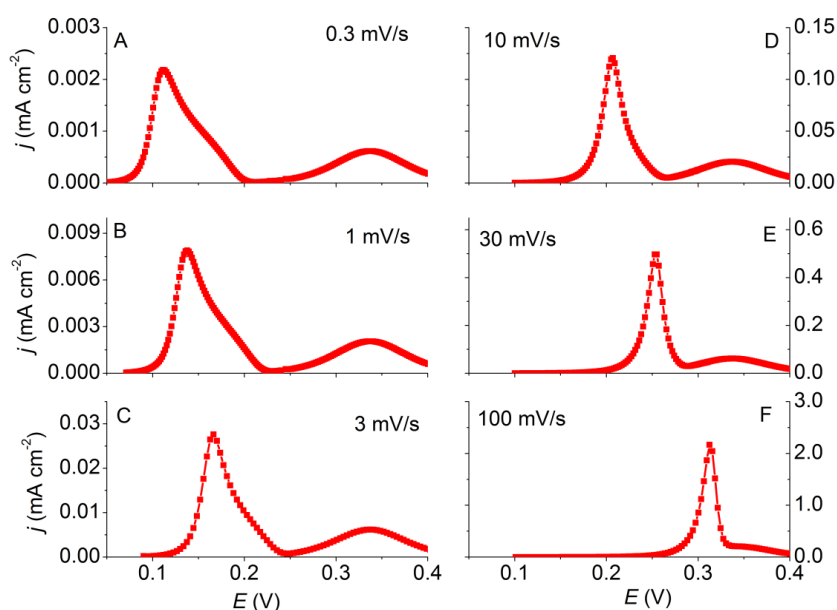
Together with negative interactions inside the adlayer, surface diffusion limitations alone may also produce tailing and shoulders in the main oxidation peak during stripping voltammetry [247,248]. Results from Fig. 4–10 suggest that, in order to differentiate these two surface effects, a scan rate study could be performed. At low scan rates, repulsive interaction effects are more pronounced, and the stripping voltammogram should exhibit an increasing tailing or the appearance of shoulders, or small peaks, on the positive side of the main peak. Instead, under merely diffusional effects the main peak should display pre-shoulders at slow v and single, wider peaks at faster v.

Figure 4-11 shows potential step transients for two k_2 and repulsive interactions between CO molecules. In the case of *extremely slow* CO oxidation constant, k_2 = 8.234x10^{-6} s^{-1}, and low repulsive interactions (Fig. 4–11A), the shape of current transients with the applied potential and its potential dependence (Fig. 4–9B) are similar to the dynamic in absence of CO–CO interactions and *slow* CO oxidation constants (Fig. 4–3D). Nevertheless, with repulsive interactions the plateau region is less extended and the transients are not symmetric and show a tailing on their descending part. Instead, for strong repulsive interactions (0.1 eV) and k_2 = 8.234x10^{-2} s^{-1} (Fig. 4–11B), the transients

are almost symmetric and bell shaped at high potentials, while asymmetric once E_f is decreased. If E_f is lowered even further, a long tail in the descending part of the peak appears and an important amount of CO_{ads} on the electrode still remains, $\theta_{CO} > 0.3$, even when the current has reached an almost steady state and is below of $0.1j_{max}$ (see inset to Fig. 4–11B).

Figure 4-11: Normalized potential step current transients at different final potentials, E_f. (A) $k_2 = 8.234\times10^{-6}$ s^{-1} and $\epsilon_{CO\text{-}CO} = 0.02$ eV; (B) $k_2 = 8.234\times10^{-2}$ s^{-1} and $\epsilon_{CO\text{-}CO} = 0.1$ eV. Inset to (B): CO coverages during step current transients. Initial CO coverage = 0.99 ML.
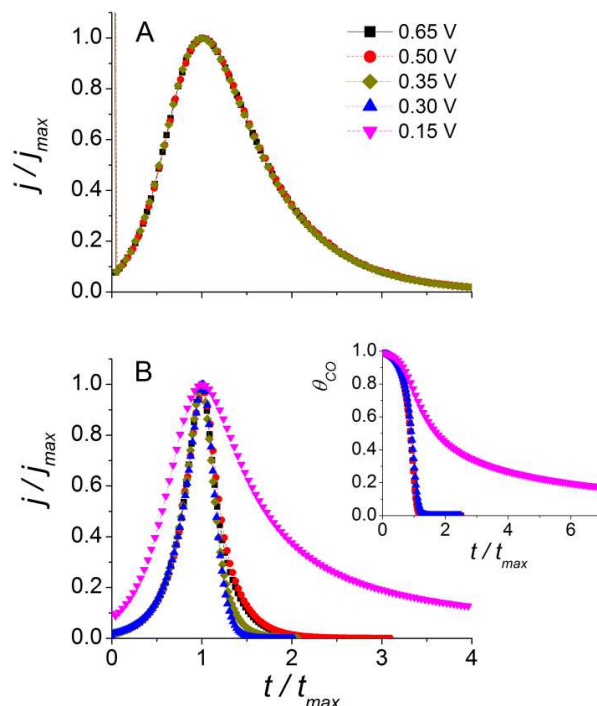
As mentioned above, tailings, pre and post-shoulders on voltammetric peaks [247,248], together with symmetric current transients that become slightly asymmetric at lower potentials, with a tailing in its descending part [248,249], have been observed in CO oxidation experiments on Rh single crystals. Results in Figs. 4–5D, 4–10 and 4–11 show that these experimental observations could also be explained in light of repulsive interactions inside the adlayer. As for example, the high amount of CO_{ads} remaining after a potential step at low E_f on sulfuric acid [248,249], without the necessity to include a second electron transfer as RDS on the mechanism. Of course, this is not the whole picture, and other important phenomena also play an important role. However, the results here highlight the importance of "*effective*" interactions in the reaction kinetics and suggest that they should be taken into account when interpreting experimental data.

4.4 Conclusions

The Mean Field Approximation theory is used to study the electrochemical CO oxidation on metallic surfaces through a Langmuir–Hinshelwood (LH) mechanism including "*effective*" lateral interactions between one of the adsorbates. Results show that differences in current transients and CVs, observed on various surface planes of Pt or Rh

and their vicinal surfaces in acidic medium, may actually be connected, not only to diffusional effects or changes in the rate determining step of the mechanism, but rather with specific features of the reaction kinetics, including, or not, a change in the "*effective*" adsorbate-adsorbate interactions inside the adlayer. Experimental findings during potential step chronoamperometry, like a plateau before a main peak and the appearance of a tailing in the descending part of the main peak, may be also explained by considering lateral interactions. On the other hand, CO oxidation on Pt(111) and its vicinal surfaces on alkaline medium may be described considering greater amount of active sites on the surface under these conditions, without include two different reactions mechanisms.

In the case of "*effective*" attractive interactions between CO–CO molecules, voltammetric peaks are usually highly asymmetric and sharp, with a steep rise and an abrupt descend once j_{max}, at $E_{p,CO/OH}$ or t_{max}, is reached. On the other hand, repulsive interactions at *slow* CO reaction rates can produce one main oxidation peak with either a shoulder or an asymmetrical tail in the descending part. At slow scan rates, or when the difference between the CO rate constant and ϵ_{CO-CO} values is large enough, $E_{p,CO/OH}$ in the SV will tends to split.

Results from simulations extend the conceptual framework for the interpretation of transient kinetics and stripping voltammograms for the CO oxidation on metallic surfaces, such as Pt and Rh, or, more general, for any reaction following an LH mechanism. In spite of the level of simplicity, the model holds great promise in the understanding of the electrocatalytic activity. However, the structural features of the real system are much more complex and it is necessary to continue refining the model.

5. Dynamic Monte Carlo Simulations for the Electrochemical CO Oxidation on Metallic Surfaces: A Langmuir-Hinshelwood Mechanism Including Lateral Interactions[5]

In this work, Dynamic Monte Carlo simulations have been used to solve a lattice-gas model for the electrochemical oxidation of CO on metallic surfaces. The reaction occurs through a Langmuir–Hinshelwood (LH) scheme in which adsorbed CO (CO_{ads}) reacts with oxygen-containing species located at an adjacent site on the surface, assumed to be adsorbed hydroxyl (OH_{ads}). In this context, the effect of lateral adsorbate-adsorbate interactions and the role of OH_{ads} and CO_{ads} diffusion on the potential dependence of the rate constant of the CO oxidation are analyzed. It is shown that including lateral interactions into the LH mechanism can reconcile different experimental results, like island formation and fast CO_{ads} diffusion. This fact highlights the importance of "*effective*" interactions in the reaction kinetics and suggests that they should be taken into account when interpreting experimental data. However, noting that this model is quite simple, only general results are presented and experimental results are not interpreted in detail. Simulations are considered useful for an improved qualitative understanding of the kinetics of CO oxidation and in the general theory for other electrochemical LH reactions.

5.1 Introduction

CO oxidation and adsorption reactions are one of the cornerstones of surface science and it is one of the most intensively studied processes in electrocatalysis [189].However, in spite of its great interest, some essential aspects demand further investigations. Nowadays, the exact mechanism of the CO oxidation reaction is still currently a subject of debate. Although *in situ* electrochemical measurements such as Scanning Tunneling Microscopy (STM) and Fourier Transform *Infrared* (FTIR) [111,190,197], as well as information obtained in ultra high vacuum (UHV) environments [198], have yielded a wealth of structural data on CO adsorption on platinum single-crystal electrodes, it is relatively unclear how these microscopic structural features affect the overall macroscopic electrocatalytic activity.

The most widely accepted mechanism for electrochemical CO oxidation on metallic surfaces is the so-called Langmuir–Hinshelwood (LH) scheme or reactant pair, in which adsorbed CO (CO_{ads}) reacts with oxygen-containing species located at an adjacent site on the surface, as originally proposed by Gilman [71]. In contrast, some authors have also proposed that the stripping of a saturated layer of CO_{ads} initially follows an Eley–Rideal (ER) scheme in the early stage of the process, in which the reaction proceeds without adsorption of anions or H_2O molecules (H_2O_{ads}), and then it follows a LH mechanism [231]. Even though, the real identity of the oxygenated species, at the present time, is not fully established yet [72,232].

Additionally, two different models have been invoked to describe the kinetics of this reaction in the LH scheme. In the first one, the reaction proceeds at the perimeter of water islands containing adsorbed hydroxyl species, OH_{ads}, in the monolayer (ML) of CO_{ads}, and it is controlled by the nucleation and growth, N&G, of these islands [93,191,192,197,200–202]. The second approach is the so-called Mean Field Approximation (MFA) [72,193–195,206], it assumes a fast surface diffusion of CO_{ads} and OH_{ads} and their perfect mixing at the electrode surface. In a more recent version, it is proposed that the oxidation reaction proceeds at specific surface sites (surface defects, kinks, edges, etc.) and both CO_{ads} and OH_{ads} diffuse to the reaction zone created by these sites [195]. It should be mentioned that while spectroscopic data support the N&G mechanism [91,111,190,203–205], accurate fitting of experimental electrochemical current transients validate the MFA [193,194,207,208,223].

There are, however, other intrinsic factors that may be responsible for the observed experimental results. As has highlighted before [189], physical properties of CO_{ads} are quite different compared to those of other adsorbates on the surface as H_2O_{ads}, OH_{ads}, and other anions, as $HSO_{4,ads}$, whose hydrogen bonds can be appreciably stronger than CO-CO lateral interactions. Hence, the formation of these bonds may easily result in CO_{ads} segregation, taking into account that electrochemical oxidation is usually studied at room temperature (RT). In consequence, the influence of all these interactions between adsorbates on the CO_{ads} oxidation can determine the surface structure, adsorption/desorption kinetics, diffusion, and chemical reaction dynamics. Specifically, "effective" interactions inside the adlayer may be attractive or repulsive, depending on the balance between inter–particle and intra–particle interactions [212–214]. Influence of lateral interactions on the electrochemical oxidation of CO has been suggested from CO oxidation studies on Pt single crystals [250] and Nafion® coated Pt(111) electrodes [67].

In contrast, most of the studies to model the electrochemical CO oxidation on metallic surfaces treat adsorbed reactants as Langmuir particles, *i.e.* no lateral adsorbate–adsorbate interactions between the species were considered [72,223,225–228]. Trying to go further this approach, Zhdanov and Kasemo [189], simulated a two particle system, A and B, with B–B attractive interactions using Monte Carlo simulations (MCS), and proved that current transients for CO oxidation are fairly sensitive to adsorbate–adsorbate lateral interactions. Specifically, they showed that with realistic values of these interactions (~4.2 kJ/mol) the reaction kinetics may be accompanied by CO segregation, provided that surface CO diffusion is fast.

Recently, a LH model including "effective" attractive and repulsive CO_{ads} interactions was solved by the MFA [167]. However, it is well known that under this approximation, the effect of repulsive/attractive short range interactions is overestimated/underestimated, depending on the process [73]. This is because the surface is considered homogeneous and so, adsorbate-adsorbate correlations cannot be taken into account and average

lateral interactions and infinite diffusion rates are assumed [73]. On the other hand, different works have shown that surface diffusion of CO_{ads} and/or OH_{ads} may play a key role on the whole reaction dynamics [121,192–195,201,207,242,244,245,248,251–255]. First theoretical efforts to describe the effect of CO_{ads} diffusion on the reaction kinetic were made by Petukhov [223] and Koper *et al.* [72]. Both works simulated a simple LH model by the MFA and MCS to illustrate the role of CO_{ads} diffusion on the CO_{ads} oxidation. Afterwards, MC technique was also employed by other groups in order to simulate other aspects of the reaction [224–228,256]. For a review of MCS of catalytic reactions, see Refs.257, 258 and 259.

The goal of the present study is to analyze the effect of lateral adsorbate-adsorbate interactions and the role of OH_{ads} and CO_{ads} diffusion on the potential dependence of the rate constant of the CO oxidation. With this objective, a LH mechanism between adsorbed CO_{ads} and OH_{ads}, resulting from water dissociation, is solved by dynamic MCS (DMCS). The model fully incorporates the nearest neighbor (*nn*) lateral interactions and the correct time dependence of rate constants [74]. Although this model ignores higher order interactions, such as three-body interactions and long-ranged interactions, within a defined interaction model, the DMC results are accurate. Noting that this model is quite simple, we present only general results and do not try to interpret any experiment in detail. Simulated results are considered useful for an improved qualitative understanding of the kinetics of CO oxidation and in the general theory for other electrochemical LH reactions.

5.2 The reaction model

A simple model, ''A + B'' reaction, on a square lattice is proposed. In the case, of a triangular lattice, results are qualitatively the same but, quantitatively, the difference is related to the number of *nn* sites, being lower for the square lattice (4 vs. 6) [219]. Althoguh this model is definitely not sufficiently realistic to understanding the detailed structural aspects of CO adsorption at the metal/electrolyte interface, the model is able to provide some interesting insights into the importance of microscopic features such as mixing, lateral diffusion, and island formation, as it will be shown below. The basic features of our model are explained in the next paragraph, but a more detailed view of is described in Ref. 72.

As mentioned, Gilman model for the electrochemical CO oxidation is widely accepted [71]. In this scheme, the reaction is described in terms of a LH mechanism with participation of an adsorbed oxygen-containing species. The exact nature of this latter species is still somewhat controversial [189,195]. Traditionally, the two most likely candidates have been H_2O_{ads}, and OH_{ads}, but recently, atomic oxygen, O_{ads}, has also been suggested [232]. If so, it could imply a whole new paradigm for electro–oxidation reactions [232–234]. Anyway, because electrochemical measurements indicate that both reactions, the formation of the oxygen–containing species and CO oxidation, are potential dependent, in this work, OH_{ads} is assumed to be the oxidising species, resulting from water dissociation. Thus, the reaction model is given by Eqns. (4.1) and (4.2) [72].

Following past studies [167,189], an "*effective*" interaction energy between CO-CO molecules that occupy neighboring sites on the surface, ϵ_{CO-CO}, will be used, in order to keep the model as simple as possible, with a measurable physical meaning and close to observable phenomena. Strictly speaking, complete schemes of CO oxidation including

lateral interactions between adsorbed species should also include $\epsilon_{CO/OH}$, $\epsilon_{CO/W}$, $\epsilon_{OH/OH}$, $\epsilon_{OH/W}$ and $\epsilon_{W/W}$ parameters (with W stating for water molecules). However, these interactions are either unknown or poorly defined or too complicated to be fully described in theoretical models. For example, OH_{ads} formation on metal surfaces is a complex process [235], even in the case of mono-crystalline surfaces [179]. Density Functional Theory (DFT) calculations have shown that $\epsilon_{OH/OH}$, $\epsilon_{OH/W}$ and $\epsilon_{W/W}$ energies are highly directional interactions, *i.e.* they can be strongly repulsive or attractive depending on the surface angle between the new OH_{ads} molecule to be formed and the already adsorbed H_2O_{ads} and OH_{ads} [211].

Two types of lateral interactions are usually distinguished [189,219,260]. Adsorbate-adsorbate interactions, in an adsorbed state, and adsorbate-transition state interactions, in an activated state. An adsorbed state means an adsorbate sitting at an optimized adsorption site, whereas an activated state refers to an intermediate reaction at the transition state. Lateral interactions of the adsorbed state have a twofold influence on the local adsorbate configuration at the active site: (*i*) they change the coverage of different adsorbates and (*ii*) they introduce correlation among adsorbates. At the activated state, lateral interactions depend on the local adsorbate configuration at the active site and modify the transition state energy [261]. According to DFT calculations, the reaction may actually occur via two steps: first CO_{ads} and OH_{ads} react to form $COOH_{ads}$; then the latter species reacts to form CO_2. Hence, the structure of the corresponding transition state is close to that of the initial state and the difference of lateral interactions in transition and initial states is expected to be relatively small.

To investigate the effect of lateral interactions, the activation energy, E_a, is required to depend on the local adsorbate configuration i at the active site (only lateral interactions between nn sites are considered). This is included by assuming that every occupied nn site modifies E_a by the same amount. In this context, E_a is increased/decreased by an amount $n_{CO}(1-\gamma_2)\epsilon_{CO\text{-}CO}$ for adsorption reactions, while it is decreased/increased by $n_{CO}\gamma_2\epsilon_{CO\text{-}CO}$ for desorption processes. Where n_{CO} is the number of neighboring sites occupied by an CO_{ads} species and γ_2 is a kind of Brønsted factor specifying to which extent the transition state for adsorption/desorption is influenced by the interactions (in all our calculations, $\gamma_2 =0.5$). For the CO oxidation reaction, E_a is decreased/increased by an amount $n_{CO}\gamma_2\epsilon_{CO\text{-}CO}$, with n_{CO} the number of CO_{ads} occupying nn sites of the reacting CO_{ads}. The reaction rate constants are assumed to obey the Butler–Volmer law for electrochemical reactions [1]. Hence they are given by:

$$\mathrm{k_{OH,ads}} = k_1 = k_1^0 \exp\left(\frac{\beta_1 e_0 E}{k_B T}\right) \tag{5.1}$$

$$\mathrm{k_{OH,des}} = k_{-1} = k_{-1}^0 \exp\left(-\frac{(1-\beta_1)e_0 E}{k_B T}\right) \tag{5.2}$$

$$\mathrm{k_{CO_2,des}} = k_2 = k_2^0 \exp\left(\frac{\beta_2 F E}{RT}\right)\exp\left(n_{CO}' \frac{\gamma_2 e_0 E}{k_B T}\epsilon_{CO-CO}\right) \tag{5.3}$$

Where the β's are transfer coefficients (taken 0.5 in all that follows), E is the electrode potential, and e_0, k_B, and T have their usual meaning. In the following, the subscripts "1", "-1" and "2" refer to the reactions of OH adsorption, OH desorption and CO oxidation, respectively. The reaction rate constants k_1^0, k_{-1}^0 and k_2^0 are independent of the lateral interactions, have the dimension s^{-1} and are assumed to be constant. The rate constants k_1^0 and k_{-1}^0 include the concentrations of water and proton at the surface, respectively,

and k_2^0 is the rate constant corresponding to the low-coverage limit. The total current density due to these reactions is given by Faraday's law, Eqn. (4.10).

We consider the oxidation of a certain (submonolayer) amount of CO preadsorbed onto the surface, with no CO present in the solution, by a voltammetric potential scan or potential step. For CO adsorption on Pt(111) and Pt(100), the absolute saturation coverage is in the range between 0.6 and 0.7 per Pt site [196,237]. Instead, here and below the coverages are defined as the ratio of the absolute coverage to the absolute saturation coverage. Thus, the relative coverage used in calculations may be close to unity. In our simulations, coverage of 0.99 is considered as saturation coverage. In addition, similar to past works [72,167,224,227], rate constants for OH adsorption and desorption were chosen such that for 20 mV s^{-1} OH adsorption appears quite reversible and they are equal to 0.02 and 10 000 s^{-1}, respectively, and the CO+OH oxidation reaction can adopt different values, as indicated in the text. Hence the potential axis we use is to some extent arbitrary. Finally, lateral interactions values used range from +0.1 (repulsion) to -0.1 eV/atom (attraction), equivalent to ca. ±9.6 kJ/mol.

Regarding surface diffusion, in DMCS the rate of CO_{ads} and/or OH_{ads} surface diffusion is assumed to occur via the place exchange mechanism, *i.e.* the rate of CO_{ads} or OH_{ads} exchanging places with an "empty" (or H_2O_{ads}) neighboring site:

$$CO_{ads} + * \longrightarrow * + CO_{ads} \tag{5.4}$$

$$OH_{ads} + * \longrightarrow * + OH_{ads} \tag{5.5}$$

In our case, this "reaction" has a rate of D s^{-1} [72], corresponding to a surface diffusion coefficient of ~10^{-15} x D cm^2 s^{-1}. In the simulations, the parameter D is varied, in order to assess the influence of CO_{ads} and OH_{ads} surface diffusion on the overall electrochemical response. However, note that in the model, the rate and diffusion constants implicitly incorporate the role of the interfacial solvation, as detailed solvent structure at the Pt/solution interface is not considered. This rate may depend on the electrode potential, but this effect is expected to be weak compared to that of the reaction steps, because diffusion of CO_{ads}, or OH_{ads}, does not involve charge transfer. Thus, in our calculations, the jump rate constants are considered to be independent of the electrode potential. When lateral interactions are taken into account, considerations explained in previous paragraphs also apply to diffusion, so the rate constants were chosen such that detailed balance was satisfied:

$$k_{diff} = D \exp\left(-\frac{\zeta_{diff}\Delta N \varepsilon_{ij}}{k_B T}\right) \tag{5.6}$$

Where ς_{diff} = 0.5 is the Brønsted–Polanyi coefficient for diffusion and ΔN is the difference in the number of occupied *nn* neighbor shell sites before and after the hop.

Experimentally, at metal/gas phase interface CO_{ads} diffusion on Pt is known to be very fast (the activation barrier for this process is about 0.3 eV [239]) and it lies in the range of 10^{-9}–10^{-11} cm^2 s^{-1} at RT [238]. Under electrochemical conditions, CO_{ads} diffusion is expected to be slower due to the CO interaction with the solution. Accurate data for the latter regime are still lacking. Estimated values from potentiostatic transients reported a CO_{ads} diffusion coefficient above 1 x 10^{-11} cm^2 s^{-1} [192,193,194,201,206], while electrochemical nuclear magnetic resonance (EC–NMR) spectroscopy studies found significantly lower values, ~3.6 x 10^{-13} cm^2 s^{-1} [254]. In the case of OH_{ads}, diffusion is usually supposed very fast. However, recent works have suggested the formation of a

hydrogen bonded water/OH_{ads} network as the rate determining step (RDS) in the CO oxidation, because the CO_{ads} reaction occurs, at least in part, by the OH_{ads} diffusion through this network [67,121]. In the absence of strongly adsorbing anions on "ideal" platinum surfaces, this process is almost certainly fast and reversible, but in the presence of them instead, OH_{ads} adlayer formation may be somewhat slow.

Recently, fast OH_{ads} and CO_{ads} diffusion was suggested when comparing stripping voltammograms (SV) for CO stripping experiments on bare and Nafion® covered Pt(111) electrodes with theoretical SVs, calculated by a MFA model including attractive CO-CO interactions, similar to the model proposed here [167]. A discussion about the role of OH_{ads} diffusion in the current response during CO oxidation by either cyclic voltammetric or potential step chronoamperometric experiments, under a LH scheme has been done in a previous work [72]. In next sections, this discussion will be extended to the case when CO-CO lateral interactions between the species are considered.

5.2.1 Computational Methods

All DMC simulations were carried out with the program CARLOS. This is a general-purpose program for DMC simulations of surface reactions. Various possibilities and features of CARLOS are described in some detail in Ref. 75 and on CARLOS´s website [76]. The program accounts for time dependence of reaction rate constants in either cyclic voltammetry or potential step chronoamperometric simulations including lateral interactions between adsorbed species [72]. The simulations were performed on either a 128 x 128 or a 256 x 256 square lattice with periodic boundary conditions. Apart from a lower noise level on the larger lattice, there is not any observable difference between both lattices.

In all cases, the initial configuration was a random configuration created by the CARLOS program for each system including lateral interactions. Initially, CO particles are adsorbed on the lattice up to a desirable coverage (usually 0.99 ML, unless stated otherwise). Then, DMC steps of diffusion are performed in order to equilibrate the adsorbed overlayer. All voltammograms, potential step transients and snapshots to be presented below were carried out on the smaller lattice size. The temperature of the system was always fixed at 300 K.

5.3 Results and discussion

As mentioned above, CO oxidation through a LH scheme, including the role of surface CO_{ads} diffusion, has been properly discussed in the literature by DMC simulations and when lateral interactions between species are considered by both MC simulations and the MFA [72,167,189,223]. Features like peak shape and Tafel curves, in both cyclic voltammetric and potential–step chronoamperometric measurements, have been fully described in past works [72,167] and are not going to be recounted here. Nevertheless, a short discussion about the influence of the lateral diffusion and island formation during the CO oxidation, following the scheme represented by Eqns. (4.1) and (4.2), in absence of interactions among the particles is given below, as a starting point to understand the effect of adsorbate-adsorbate correlations in the system current response.

5.3.1 Non-Interacting System

In absence of diffusional effects, the shape of potential step current transients depends on the controlling process, Eqns. (4.1) or (4.2) [72,167]. If the CO_{ads} oxidation reaction is the fastest process, current transients are asymmetric, with a stepped current rise at the beginning and a fast decay after the current maximum is reached. In this case, the descending part of the peak is described by the OH_{ads} formation, Eqn. (4.2). These asymmetric transients cannot be described by the theory for Nucleation and Growth (N&G) processes, first derived by Bewick, Fleischmann and Thirsk (BFT) [262,263], because, as explained in a previous work [72], there is a breakdown of the Avrami theorem [264–266], since the reaction can occur on already existing "islands". Instead, if the CO_{ads} oxidation reaction is the slowest process, current transients could be properly described by either the BFT theory for a progressive nucleation [262,263], with an initial quadratic rise in current, or a MF simplified model, derived from Eqns. (4.1) and (4.2), and assuming a reversible, fast reaction for the oxygen–containing species, so that its coverage, θ_{OH}, is always proportional to $(1-\theta_{CO})$ [189,194,223].

Role of CO_{ads} and OH_{ads} surface mobility in absence of particle-particle interactions:
Figure 5-1 shows the logarithm of the current maximum time, log t_{max}, in the current evolution, *j–t* profile, as function of the final potential, E_f, for different combination of D_{CO} and D_{OH} values and two different sets of rate constants: A *fast* rate, where the CO oxidation constant rate is faster than OH adsorption, $k_2 = 8.234 \times 10^{-1}$ s^{-1}, and a *slow* rate, where the OH adsorption is faster than the CO oxidation, $k_2 = 8.234 \times 10^{-5}$ s^{-1}. In addition, Figure 5-2 depicts normalized current transients, j/j_{max}, after stepping from a potential at which a 0.99 CO ML is stable to E_f = (▲) 0.65, (●) 0.50 and (■) 0.35 V, for the *slow* set of rate constant. Normalizations are made for both scales, using j_{max} and its corresponding time, t_{max}. For the sake of comparison, simulated results under the MFA are also included in both figures.

Figure 5-1:   The logarithm of the time at the current maximum t_{max}, as function of the final potential, E_f. Lower curve: $k_2 = 8.234 \times 10^{-1}$ s^{-1} (◄, ►); upper curve: $k_2 = 8.234 \times 10^{-5}$ s^{-1} (■, ●, ▲, ▼). For the sake of comparison, simulated curves by MFA are also included (empty symbols).
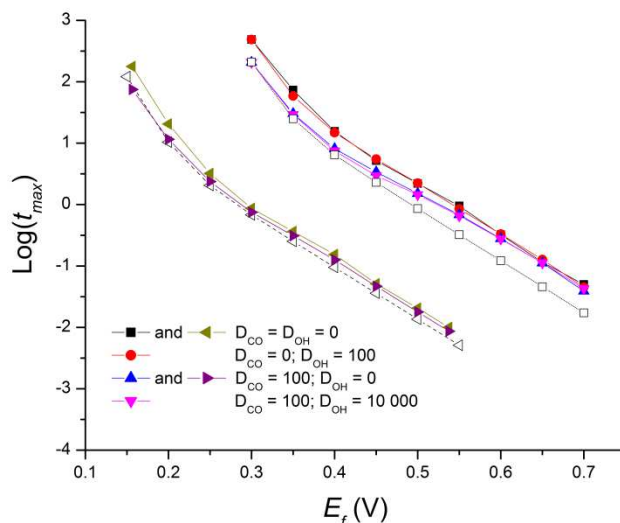
Suppressing adsorbate diffusion in the system dynamics, $D_{CO} = D_{OH} = 0$, enables island formation on the surface and, thus CO_{ads} molecules can be only oxidized at the perimeter

of existing holes [72]. In this case, both sets of rate constants, *fast* and *slow*, produce log t_{max} vs. E_f curves similar to the case when diffusional effects are not considered, with Tafel slopes of ≈ 40 mV at low E_f and ≈ 119 mV at high E_f values [72,167], but these curves are shifted upwards. The shift magnitude depends on k_2 and is greater for slower CO constant rates (Fig. 5–1). In addition, the shape of normalized current transients follows either a progressive nucleation mechanism for the *fast* set [72] or a instantaneous nucleation scheme [262,263], with an initial linear rise in current, for the *slow* set, regardless E_f (Fig. 5–2A). In both cases, current transients are quite different to those calculated by the MFA, under the same conditions [72,167]. Including OH_{ads} diffusion, D_{OH} = 0, does not change the system response (Figs. 5–1 and 5–2B).

Figure 5-2: Normalized DMC potential step current transients for $k_2 = 8.234 \times 10^{-5}$ s^{-1}, from a 0.99 CO ML at different final potentials: (▲) 0.65 V, (●) 0.50 V, (■) 0.35 V. For the sake of comparison, simulated curves under the MFA are also included (solid lines).
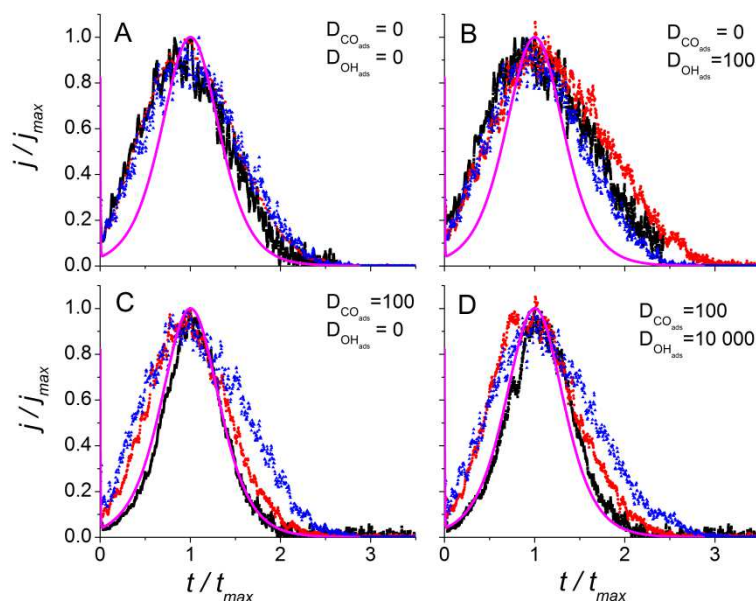
Including measurable CO_{ads} diffusion, D_{CO} = 100, enhances mixing and suppresses the formation of large holes. In addition, the holes also effectively diffuse and the OH_{ads} adsorption can take place at many different places, making more CO_{ads} available for attack by OH_{ads}. In this case, log t_{max} vs. E_f curves have an intermediate response (Fig. 5–1). At E_f > 0.6 V, j–t profiles are similar to D_{CO} = 0 curves [72], with Tafel slopes ~119 mV and, for the *slow* set, transients are described by an instantaneous nucleation mechanism (Figs. 5–2C and D). At E_f < 0.4 V, curves follow the MF dynamics, with Tafel slopes around 80–105 mV and current transients following a progressive nucleation scheme [72], Figs. 5–2C and D. In consequence, between 0.4 < E_f < 0.6 V, Tafel slopes are around 145 to 155 mV, and transients have an intermediate shape between both cases described (Figs. 5–2C and D at 0.50 V). The magnitude of the slope in this region depends on the D_{CO}/k_2 ratio.

Tafel slopes of ca. 60 to 80 mV have been found in different potentiostatic studies of CO oxidation [191,193,194,240,241]. It was suggested [240,241] that such Tafel slopes, close to 60 mV, might indicate the presence of a slow chemical step in the reaction scheme as RDS [267]. Here, Tafel slopes lower than 119 mV have been obtained in certain E_f ranges, without considering a chemical step in the mechanism. Additionally, a change from progressive to instantaneous nucleation at increasing E_f during the CO oxidation on

Pt surfaces has been also reported [191], together with Tafel slopes as high as 240 mV at high potentials [191,207]. Although such a high values are not reproduced in our simulations, Tafel slopes higher than 119 mV can be also obtained in narrow potential ranges at high E_f, by including the role of adsorbate diffusion during simulations. However, in this work, once the oxidation begins, the reactive OH can absorb in all generated empty sites. It is expected that with a fixed number of active sites, CO_{ads} and OH_{ads} diffusion will play a more important role.

From results explained above, it is concluded that the change in the transient shape with E_f is an effect of the relation between the "*effective*" molecular adsorbate mobility and the "*effective*" constant rate of the RDS on the LH scheme ($k_{diffusion}/k_{RDS}$). As it was explained [223], current transients, for a reaction following a LH scheme, are asymmetric at low "*effective*" adsorbate diffusion (instantaneous nucleation) and become more symmetric when the hopping rate (diffusion) is increased (progressive nucleation), compared to the constant rate of the RDS. Other works have also observed this crossover from a continuous to an instantaneous nucleation [268], even in dynamics with local barriers [269]. This change occurs when the diffusion length of the adsorbates is about the average cluster distance [268,269]. In the case shown in Figs. 5–2C and D, the crossover is understandable because the rate of the RDS, *i.e.* CO oxidation, changes with the potential, while the CO diffusion rate does not. Correspondingly, OH diffusion may be the driving force of the crossover between continuous and instantaneous nucleation if OH_{ads} adsorption is the RDS in the mechanism (see below).

5.3.2 System including lateral interactions

Attractive interactions: Typical stripping voltammograms for CO oxidation from a squared lattice calculated taking into account attractive lateral *nn* CO-CO interactions (negative $\epsilon_{CO–CO}$ values), and neglecting shifts of equilibrium positions of adsorbed particles, are shown in Figure 5-3 for different combination of D_{CO} and D_{OH}. In Figure 5-4, stripping voltammograms at different scan rates, *v*, for k_2 = 82.34 s^{-1} and ϵ_{CO-CO} = -0.1 eV are given, and Figures 5–5A and B plot E_p vs. log *v*, for different k_2 and ϵ_{CO-CO} combinations. Additionally, Figures 5–6A and B show typical equilibrium distributions of the species over the surface (snapshots), for different k_2 and $\epsilon_{CO–CO}$.

As expected, attractive interactions shift the CO oxidation peak, $E_{p,CO/OH}$, to higher potentials [167], proportional to their magnitude, *i.e.* greater $|\epsilon_{CO–CO}|$ values produce bigger shifts. However, MFA predicts faster reaction rates than DMCS, although the effect of attractive interactions is overestimated in this approach. This is consequence of the important role of surface diffusion on the oxidation dynamics, not taken into account into the MFA, but which also decrease the CO reaction rate (empty symbols, Fig. 5–3). Besides, while in the MFA the intensity and sharpness of $E_{p,CO/OH}$ increase at stronger attractions, in DMCS they depend on k_2 and D_{CO}/D_{OH} values. For example, at k_2 = 8.234x10^{-2} s^{-1} and despite D_{OH}, if D_{CO} = 0 $E_{p,CO/OH}$ is broad, regardless $\epsilon_{CO–CO}$. Contrary, if D_{CO} = 100 $E_{p,CO/OH}$ broadens and decreases in intensity when decreasing $\epsilon_{CO–CO}$ (Fig. 5–3). For strong attractions (-0.1 eV), the shape of $E_{p,CO/OH}$ for D_{CO} = 100 coincides with D_{CO} = 0 (Fig. 5–3D), even for k_2 = 8.234x10^{-1} s^{-1} (upper curve, Fig. 5–5A).

In contrast, for strong attractions and a fast CO constant rate, k_2 = 82.34 s^{-1}, including OH_{ads} diffusion may play a non–negligible role (Fig. 5–3D). In this case, the full–width half–maximum (FWHM) value of the peak slightly increases at faster *v*. At slow *v*, $E_{p,CO/OH}$ occurs in a potential region where OH desorption is the fastest reaction and so, the

"*effective*" OH_{ads} diffusion is high, even if $D_{OH} = 0$. Therefore, $E_{p,CO/OH}$ for $D_{CO}/D_{OH} = 100/0$ and 100/10000 are similar, though somewhat sharper in the latter case (Figs. 5–4A, B and C). At faster v, $E_{p,CO/OH}$ becomes broader and shifts to higher potentials if $D_{OH} = 0$, although it occurs in the same region where OH_{ads} adsorption occurs (Figs. 5–4D, E and F). Here, the "*effective*" adsorption/desorption OH reaction is not so fast to fill all the "holes" in the adlayer and OH_{ads} diffusion is fast enough to increase OH_{ads} concentration at the perimeter of the reaction front.

Figure 5-3: Stripping voltammograms at 50 mV s^{-1} and attractive lateral interactions ϵ_{CO-CO}, as indicated in figure. Initial CO coverage = 0.99 ML. $k_2 = 8.234 \times 10^{-2}$ s^{-1}, ($\blacksquare$) MFA; D_{CO}/D_{OH} 0/0 ($\blacktriangle$); 100/0 ($\blacktriangledown$). $k_2 = 82.34$ s^{-1}, ($\bullet$) MFA; 0/0 ($\blacktriangleleft$); 100/0 ($\blacktriangleright$); ($\star$) 100/10000. For the sake of comparison DMC curves in absence of interactions are also given (empty symbols).

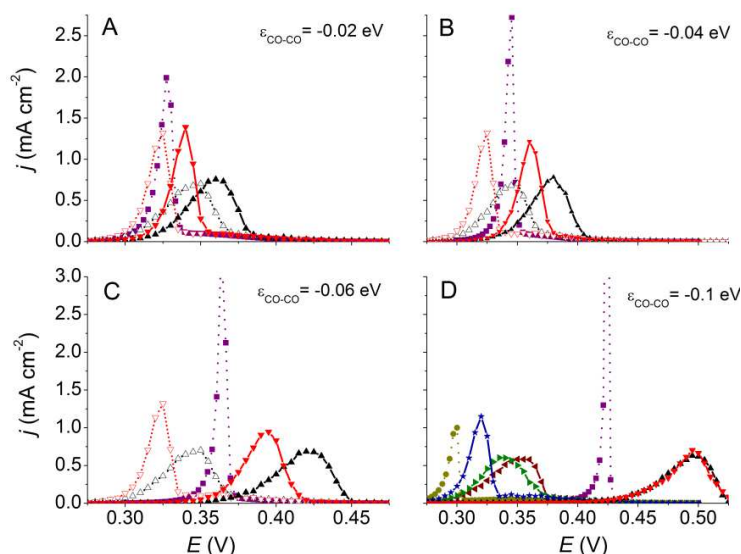**Figure 5-4:** Stripping voltammograms for $k_2 = 82.34$ s^{-1} and $\epsilon_{CO-CO} = -0.1$ eV at different sweep rates. Initial CO coverage = 0.99 ML. ($\blacksquare$) MFA; $D_{CO}/D_{OH} = 100/0$ ($\blacktriangle$); 100/10000 ($\blacktriangledown$); 0/100 ($\bullet$). For 50 mV s^{-1}, view Fig. 5–3D.
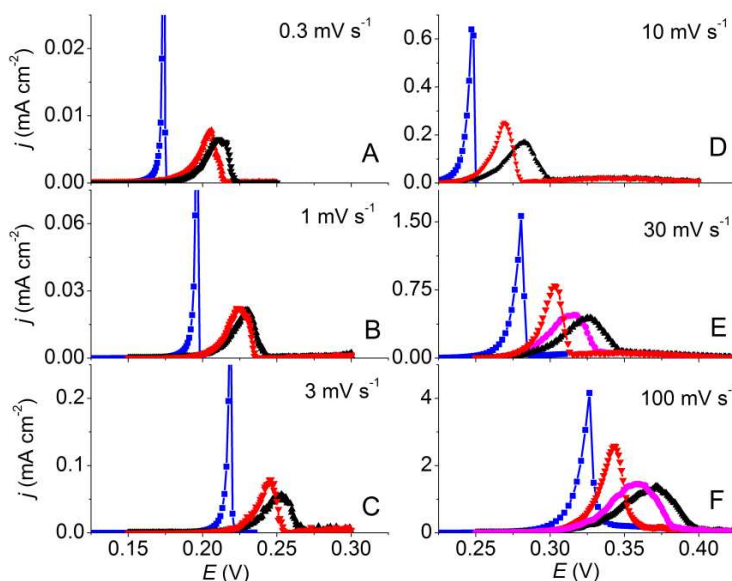
Figure 5-5: Peak potential $E_{p,CO/OH}$ as a function of the logarithm of the sweep rate v. k_2/ϵ_{CO-CO} = 8.234x10^{-1} s^{-1}/-0.1 eV (upper curve, A); 82.34 s^{-1}/-0.1 eV (lower curve, A); 8.234x10^{-1} s^{-1}/-0.02 eV (B); 8.234x10^{-4} s^{-1}/0.1 eV (C); 8.234x10^{-2} s^{-1}/0.1 eV (D). Empty symbols are calculated curves by the MFA.
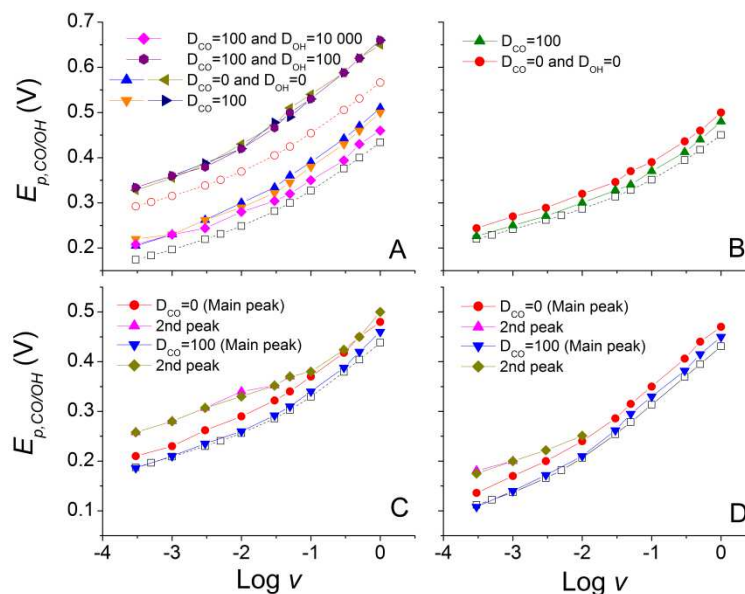
Figure 5-6: Snapshots of surface during stripping voltammetry in Figs. 5–3 and 5–9. Green: OH; Red: CO; Blue: empty site (H$_2$O$_{ads}$). A and B: ϵ_{CO-CO} = -0.1 eV; k_2 = 8.234x10^{-2} s^{-1} and D_{CO}/D_{OH} = 100/0 (A); 82.34 s^{-1} and 100/10000 (B). C, D, E and F: ϵ_{CO-CO} = 0.1 eV, k_2 = 8.234x10^{-4} s^{-1} and 100/0 (C) 8.234x10^{-2} s^{-1} and 0/0 (D); 100/0 (E); 0/100 (F).
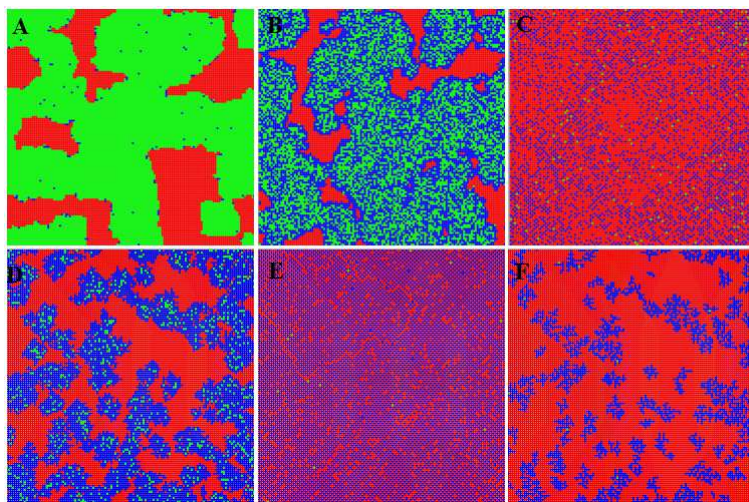
In consequence, OH$_{ads}$ diffusion only becomes significant in the mechanism if OH$_{ads}$ formation controls the reaction, all empty sites are available for adsorption, desorption and diffusion, and OH$_{ads}$ diffusion is faster than the "*effective*" adsorption/desorption rate. This can be clearly seen in Fig. 5–6. At strong attractive interactions, if the reaction rate is controlled by the CO oxidation rate, the OH$_{ads}$ adsorption is in quasi-equilibrium. Thus, large regions of CO$_{ads}$ can only be oxidized at the perimeter of the existing holes, which are fully occupied by OH$_{ads}$, impeding its diffusion (Fig. 5–6A). Instead, if the reaction is

controlled by OH_{ads} adsorption, there are empty regions around CO_{ads} islands towards which OH_{ads} can diffuse and increase the oxidation rate (Fig. 5–6B).

In all cases, again nonlinear plots are obtained, but slopes can be higher than values obtained in the non-interacting system, *i.e.* ≈ 40 mV at slow v (or low E_f) and ≈ 119 mV at fast v (or high E_f) [72, 167] (Figs. 5–5A and B). It depends on the complex dynamic inside the adlayer during the reaction, since at the beginning the CO oxidation rate is slower than at the end, not only because of the change in the applied potential, but also because the decrease in coverage as the reaction proceeds. At $v < 3$ mV s^{-1}, both simulations, MFA and DMC, predict slopes within 50 and 70 mV, while for $3 < v < 100$ mV s^{-1} slopes between 60 and 85 mV are obtained. At faster v, MFA predicts slopes between 107 and 111 mV, while DMCS report values higher than 130 mV.

Differences between MFA and DMCS are consequence of the inability of MFA to take into account surface heterogeneities, as the island formation, and the assumption of infinite adsorbate diffusion. Additionally, for attractive interactions, fast CO_{ads} diffusion may also facilitate island formation, contrary to the non-interacting case [167], and the average island size becomes bigger when ϵ_{CO-CO} decreases [189]. If the attraction is weak (Fig. 5–5B), the equilibration of the adlayer does not always keep up with the oxidation rate and diffusion does not compete with the reaction for adsorbed particles. The existing holes inside the adlayer effectively diffuse along domain boundaries of the islands, which in turns can reduce the formation of large holes and increases the CO oxidation rate. However, at strong attractive interactions, CO_{ads} diffusion is significantly faster than CO_{ads} reaction and islands are almost as large as in the case when $D_{CO} = 0$. In other words, attractive interactions suppress "hole" diffusion, important to make more CO_{ads} available for attack by OH_{ads}, as explained above [72].

Figure 5-7 shows normalized current transients, obtained by stepping from a potential with a stable 0.99 CO ML to different E_f, for two CO oxidation constants and negative ϵ_{CO-CO} values. Normalization is made for both scales against j_{max} and t_{max}. The log t_{max} vs. E_f, is plotted in Figure 5-8A. As can be appreciated, in all cases MFA again overestimates the CO oxidation rate (Fig. 5–8A) and their transients are quite different from DMC transients (Fig. 5–7), as in absence of lateral interactions and the *fast* set of rate constants [72]. In both cases, nonlinear Tafel plots are again obtained [72,167]. At slow CO_{ads} oxidation rates and moderate ϵ_{CO-CO}, curves are similar to Fig. 5–1 (upper curve, Fig. 5–8A). At fast CO oxidation constants and strong attractions (lower curve, Fig. 5–8A), at $E_f < 0.25$ V and at $0.25 < E_f < 0.45$ V slopes between 45–50 and 84–125 mV are calculated, respectively. At $E_f > 0.45$ V, Tafel slopes higher than 119 mV are observed for $D_{OH} = 100$, and ~119 mV for $D_{OH} = 0$.

Similar to results in Fig. 5–2, in some cases in Fig. 5–7 current transients apparently also show a change in the dynamics, from an instantaneous to a progressive nucleation at decreasing E_f, and transients become asymmetric at $E_f = 0.35$ V. Nevertheless, while for slow CO oxidation constants and moderate attraction the CO_{ads} diffusion is at the origin of the crossover (Figs. 5–7A, B and C), as in the case without interactions in Fig. 5–2, for fast CO_{ads} oxidation constants and strong attractive interactions (Figs. 5–7D, E and F) OH_{ads} diffusion is the driving force for the crossover. A simple explanation to understand this feature follows the same arguments discussed before. Additionally, transients with the initial quadratic current rise show an extended plateau, because at the beginning of the oxidation, OH_{ads} molecules replace CO_{ads} species (no empty sites) and the reaction rate is almost constant, similar to MF transients obtained in absence of interactions [167]. In

contrast, transients with an initial linear current rise have a small tailing in the descending part, especially at for slow CO oxidation constants and moderate attraction.

Figure 5-7: Normalized DMC potential step current transients. Initial CO coverage 0.99 ML. D_{CO}/D_{OH} = 0/0 (■); 0/100 (●); 100/0 (▲) and 100/10000 (▼). A, B and C: k_2/ϵ_{CO-CO} = 8.234×10^{-4} s^{-1}/-0.04 eV. D, E and F: 82.34 s^{-1}/-0.1 eV. For the sake of comparison calculated transients by MFA under the same conditions are also given (solid line).
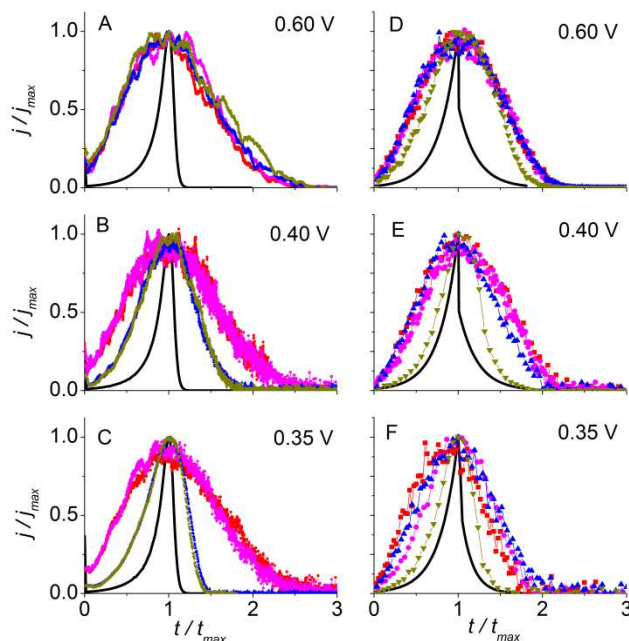
Figure 5-8: The logarithm of the time at the current maximum t_{max}, as function of the final potential, E_f. k_2/ϵ_{CO-CO} = 8.234×10^{-4} s^{-1}/-0.04 eV (upper curve, A); 82.34 s^{-1}/-0.1 eV (lower curve, A); 8.234×10^{-6} s^{-1}/0.02 eV (upper curve, B); 8.234×10^{-2} s^{-1}/0.1 eV (lower curve, B). Empty symbols are calculated curves by the MFA under the same conditions.
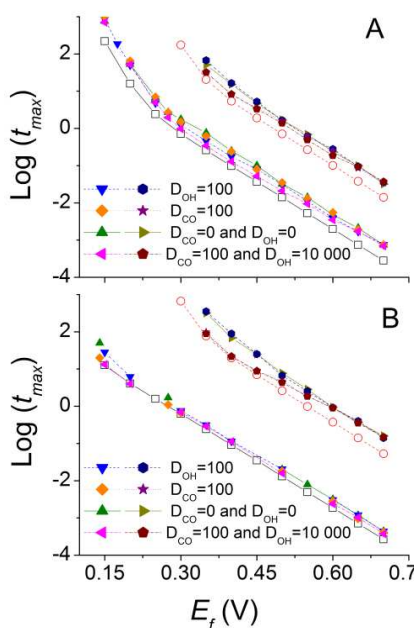
Negative interactions: **¡Error! La autoreferencia al marcador no es válida.** shows several stripping voltammograms when repulsive interactions are considered, while Figure 5-10 resumes SV at different scan rates, $0.3 < v < 100$ mV s^{-1} (for 50 mV s^{-1}, view Fig. 5–9B), for $k_2 = 8.234 \times 10^{-2}$ s^{-1} and $\epsilon_{CO-CO} = 0.1$ eV. Additionally, plots of $E_{p,CO/OH}$ as function of log v for cases B and C in Fig. 5–9 are presented in Figs. 5–5C and D, and typical equilibrium distributions of the species over the surface are given in Figs. 5–6C, D, E and F.

Figure 5-9:   Stripping voltammograms at 50 mV s^{-1} and repulsive lateral interactions ϵ_{CO-CO}. Initial CO coverage 0.99 ML. A and B: $k_2 = 8.234 \times 10^{-2}$ s^{-1}: MFA (■); $D_{CO}/D_{OH} = 0/0$ (▲); 100/0 (▼). C. 8.234×10^{-4} s^{-1}: MFA (●); 0/0 (◀); 100/0 (▶); 0/100 (★). For the sake of comparison DMC curves in absence of interactions are also given (empty symbols).
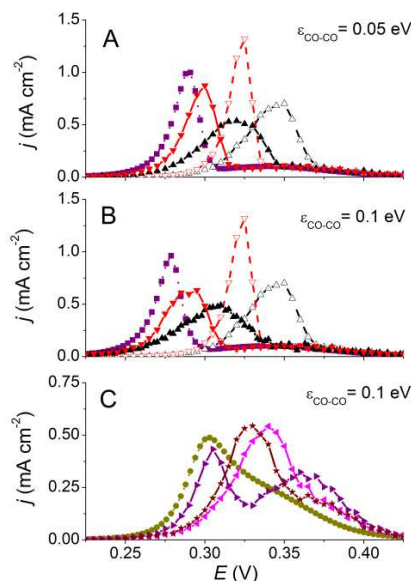
Figure 5-10: Stripping voltammograms for $k_2 = 8.234 \times 10^{-2}$ s^{-1} and $\epsilon_{CO-CO} = 0.1$ eV at different sweep rates. Initial CO coverage = 0.99 ML. MFA (■); $D_{CO}/D_{OH} = 0/0$ (▲); 100/0 (▼); 0/100 (●). For 50 mV s^{-1}, view Fig. 5–9B.
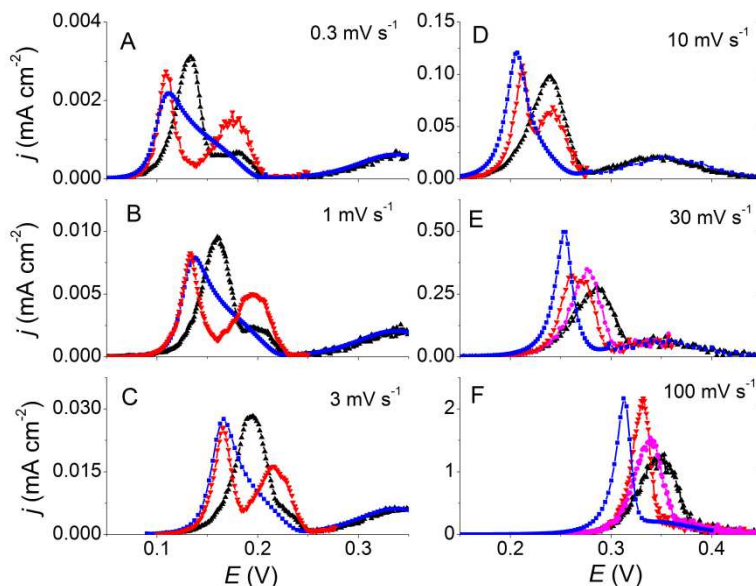
Repulsive interactions between CO molecules broaden and shift to lower potentials the CO oxidation peak, Fig. 5–9. However, MFA again overestimates the oxidation rate (overestimates repulsive interaction effect) and the $E_{p,CO/OH}$ negative shift is slightly higher than in DMCS. In contrast to attractive interactions, stronger repulsive interactions do not change significantly the SV (Figs. 5–9A and B), *i.e.* doubling ϵ_{CO-CO} only produces a small shift in height and position of $E_{p,CO/OH}$, bigger if $D_{CO} = 0$. Additionally, when $E_{p,CO/OH}$ occurs in a potential region where $OH_{ads}$ desorption is still important, OH_{ads} diffusion has little influence on the voltammetry (Fig. 5–10). This is because the CO_{ads} oxidation rate decreases during the reaction and thus, at the end of the oxidation, the entire reaction is usually controlled by the CO oxidation rate.

For comparatively strong repulsion (0.1 eV) and low CO constant rates, $k_2 = 8.234 \times 10^{-4}$ s^{-1}, MFA and DMCS with $D_{CO} = 0$ predict the existence of a shoulder in the positive side of the main peak [167]. Including CO_{ads} diffusion in DMCS leads to the appearance of two distinct peaks (Fig. 5–9C). This splitting of $E_{p,CO/OH}$ is also seen at slow v and faster k_2 (Fig. 5–10). Because of that, the FWHM value of the peak always increases at slower v. Faster scan rates produce only single and tailed peaks. As expected, if $D_{CO} = 100$ this transformation occurs at faster v than for $D_{CO} = 0$. In both cases, increasing v decreases the charge under the first peak and increases it under the second peak.

The presence of these two peaks in the SV is a consequence of the coexistence of two different domains inside the adlayer (Figs. 5–6C to F). The first peak represents domains with high packing density and a faster oxidation rate due to repulsive interactions between CO molecules. Contrarily, the second peak corresponds to low packing density domains, in which the reaction occurs without the effect of lateral interactions. Hence, its potential dependence does not change with D_{CO} (Figs. 5–5C and D). MFA is unable to predict two peaks in the SV because it cannot describe the non-random molecular distribution on the electrode surface

Interestingly, the maximum current in $D_{CO} = 100$ voltammograms is higher than in $D_{CO} = 0$ voltammograms only when $v > 30$ mV s^{-1} (Figs. 5–10A to D). This is because the *effective* oxidation rate also depends on OH_{ads} concentration and, if the CO oxidation constant rate is very high, the reaction may inhibit itself, *i.e.* at faster reaction rates, the consume of OH_{ads} is high, keeping almost zero its concentration in the adlayer and so, a slow reaction rate. At faster v, $E_{p,CO/OH}$ is shifted to higher potentials where the *effective* OH_{ads} formation rate is faster and the entire reaction rate increases. This fact highlights the complexity and interrelation of the processes inside the adlayer.

Finally, both approximations MFA and DMCS, including CO_{ads} diffusion, predict similar $E_{p,CO/OH}$ vs. log v plots at slow v (Figs. 5–5C and D), but curves deviate at faster v. Instead, for $D_{CO} = 0$ the curve is always shifted upward, because of poor mixing inside the adlayer. Similar to the case when attractive interactions are considered, slopes around 50 and 70 mV are obtained for $v < 30$ mVs^{-1}; but between $3 < v < 100$ mVs^{-1} slopes are higher and ca. ~90 to 110 mV. At $v > 100$ mV s^{-1}, if the oxidation rate is slower than OH_{ads} adsorption, the CO_{ads} diffusion is hindered and slopes higher than 145 mV s^{-1} can be obtained (Fig. 5–5C).

Figures 5–11 and 5–12 show normalized current transients for two CO oxidation constants and repulsive interactions, at different E_f. For a slow CO oxidation constant and low repulsive interactions, the change in shape of current transients with the applied potential (Fig. 5–11) and its potential dependence (upper curve, Fig. 5–8B) are quite similar to curves in absence of CO-CO interactions and slow CO oxidation constants,

when adsorbate diffusion is taken into account explicitly (Figs. 5–1 and 5–2), *i.e.* all current transients have an initial linear rise in current. However, at lower potentials if D_{CO} = 100, there is change and transients now presents an initial quadratic rise in current. Additionally, a tailing on the descending part of the transients is observed for all cases in both MF and DMC approximations.

Figure 5-11: Normalized DMC current transients for k_2 = 8.234x10^{-3} s^{-1} and ϵ_{CO-CO} = 0.02 eV, from a 0.99 CO ML. D_{CO}/D_{OH} = 0/0 (■); 0/100 (●); 100/0 (▲); 100/10000 (▼). For the sake of comparison calculated transients by MFA are also given (solid line).

Figure 5-12: Normalized DMC potential step current transients for k_2 = 8.234x10^{-2} s^{-1} and ϵ_{CO-CO} = 0.1 eV, from a 0.99 CO ML. D_{CO}/D_{OH} = 0/0 (■); 0/100 (●); 100/0 (▲); 100/10000 (▼). For the sake of comparison calculated transients by MFA are also given (solid line). Insets: CO coverages during step current transients.
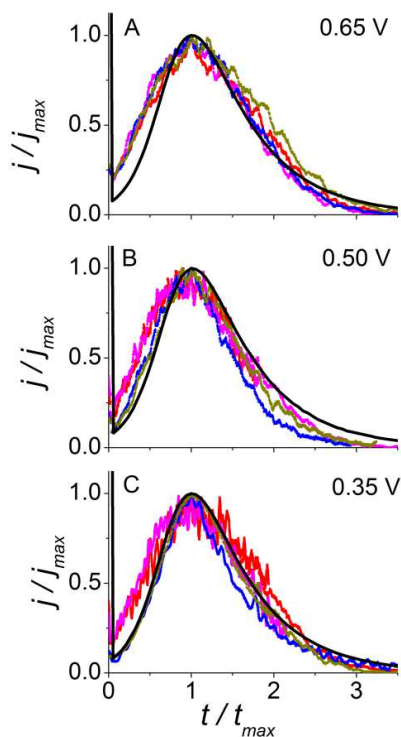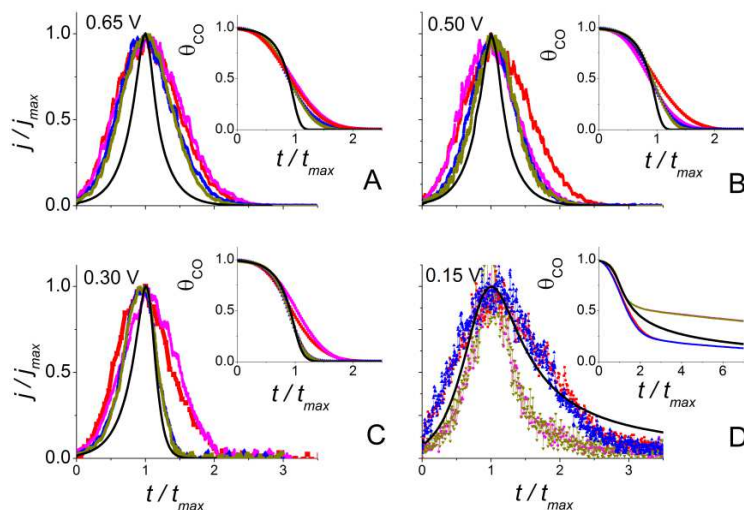
In the case of strong repulsive interactions and k_2 = 8.234x10^{-2} s^{-1} (Fig. 5–12), MFA predicts sharper transients than DMC simulations. At high potentials, all transients are almost symmetric, and DMC transients are similar between them, regardless D_{CO} or D_{OH}. When decreasing E_f, transients become sharper and if D_{CO} = 100, they are similar to MFA curves. However, if E_f is lower than $E_{p,OH}$, the CO_{ads} diffusion has now a negligible effect in the shape of current transients and is D_{OH} what determines it. In this case, transients are asymmetric and exhibit a tailing in the descending part (both MF and DMC transients). In this case, even when the current tends to zero, there is still a significant amount of CO_{ads} adsorbed on the surface, especially if $D_{OH} \neq 0$ (see insets to Fig. 5–12).

On the other hand, MFA and DMCS with D_{CO} = 0 almost predict the same log t_{max} vs. E_f curves, but in the latter case, it is shifted upward (Fig. 5–8B). Instead, if CO diffuses, curves show a mixed dynamics. At low E_f, DMCS follow the MFA curve, while at higher E_f, practically all the holes in the CO layer are immediately filled by OH_{ads}, leaving no room for CO_{ads} surface migration, and D_{CO} = 100 curves joint D_{CO} = 0 curves. In the transition region Tafel slopes higher than 119 mV can be obtained.

5.3.3 A brief comparison between theoretical and experimental results

In acidic medium, the most appealing features of SVs for CO oxidation on Pt(111) are the following [93,199,200]. At low coverages, when a significant fraction of the surface is free of CO_{ads} and available for hydrogen adsorption, H_{ads}, a single oxidation peak is observed. As CO_{ads} coverage increases, the intensity of this peak decreases and a second oxidation peak appears at higher potentials. Finally, at high coverages, where no sign of H_{ads} is detected, only the latter, sharp and narrow peak remains. In this case, similar dynamics have been also reported on Pt(100), the narrower the peak the greater the oxidation overpotential, with increasing FWHM at faster v, as in Fig. 5–4 and fast $D_{OH} \neq 0$, and Tafel slopes of 60 and 80 mV for Pt(100) and Pt(111), respectively [199]. These results were associated to the presence of two types of CO-arrangements [93,200], one easily oxidizable at low coverages, and a second one with compact CO_{ads} domains, more difficult to oxidize, at high coverages.

In addition to stripping results, temperature programmed desorption (TPD) [243], low energy electron diffraction (LEED) [198,243], *in situ* IR spectroscopy [91,111,203–205,237,243] and optical second harmonic generation (SHG) [243] studies have also related the adsorbate adlayer structure with the possible formation of CO_{ads} islands at high coverages, and the appearance of two peaks in the SVs with CO adsorbed in different surface sites. In consequence, an N&G kinetics during the oxidation [93,191,192,197,200–202], together with low CO surface mobility, has been assumed. Instead, symmetric current transients, that become slightly asymmetric at lower E_f (with tailing in the descending part), during potentiostatic studies on Pt(111) and its stepped surfaces, in both acidic [193,194] and alkaline media [242,244–246], have been interpreted as a clear indication of a LH mechanism including fast CO diffusion [72,193–195,206]. Notice, however, that, from simulations, these transients could be also reproduced with low k_2 and either moderate or low lateral interactions, both attractive (Fig. 5–7) and repulsive (Fig. 5–11).

In contrast, SVs in alkaline solution for Pt basal planes, between 5 < v < 500 mV s^{-1} [242,246,255], show a different dynamics, similar to those depicted in Fig. 5–10, and

results have been explained considering CO$_{ads}$ diffusional restrictions [242,245,251,252,255]. On Pt(110), similar to Fig. 5–10 for D_{CO} = 0, two peaks can be differentiated in the SV at slow v, that transform into one broad peak at faster v, with a slope of 99 mV for the plot of $E_{p,CO/OH}$ vs. log v. On Pt(111) [255], SVs shown a pre-wave, attributed to the presence of defects in the electrode, and a main peak with a small shoulder at low v. In this case, a slope of 67 mV has been reported. At last, on Pt(100) [242], $E_{p,CO/OH}$ does not exhibit shoulder or tail; however, in this case a detailed scan rate study is missing.

Experimental results in acidic medium at high coverages, both SV and current transients, can be described considering *effective* attractive CO-CO interactions. In this case, sharp and narrow peaks, with increasing FWHM at faster v, together with symmetric transients, are predicted from simulations, accompanied of island formation. The difference in physical properties of adsorbed molecules may give rise to these *effective* interactions, *i.e.* while water/OH species can form a stable network, owing its attractive interactions, CO-CO and CO-H$_2$O interactions are repulsive [93,120,196]. For low CO coverages, this balance cannot explain experimental results. In this case, it is proposed that CO$_{ads}$ and water molecules form a mixed phase in which CO$_{ads}$ and water occupy adjacent sites. As CO$_{ads}$ coverage increases, co-adsorbates segregate into incompressible islands containing only water and compressible, internally repulsive, patches with CO$_{ads}$ [120], with a small percentage of the surface covered by the mixed phase, given rise to two different SV peaks. At high CO coverages, the entire surface would be composed by water and CO$_{ads}$ islands.

Calculations based on DFT help to shed light on microscopic structures and processes. They indicate that chemical bonding in specific adsorption is hardly influenced by water, because of weak water-metal interactions. However, this is not necessarily true for reaction barriers in electrocatalytic reactions. Molecular simulations of water-metal interfaces at RT indicate that water molecules of the first layer at the interface remain rather localized, forming structures close to an ice-like layer [270]. For CO adsorption on Pt, UHV studies reported a $\left(\sqrt{3}x\sqrt{3}\right)$R30° superstructure on a triangular lattice at θ < 0.33. This structure, in which *nn* sites are unoccupied, indicates repulsive *nn* interactions, and, probably, attractive next-nearest-neighbor interactions [271]. It could be suggested that at low coverages (below ⅓), CO adsorbs preferably on the "holes" of the water ice-like structure, forming a mixed CO/water phase. Higher CO coverages disrupt water network and adsorbates now segregate in two phases (island formation). In agreement, different CO$_{ads}$/H$_2$O$_{ads}$ structures have been reported depending on CO$_{ads}$ coverage and the potential at which CO is adsorbed [272]. A full detailed simulation including all the interactions in the adlayer could clarify this point.

Interactions between co-adsorbates driving the CO$_{ads}$ reaction dynamics can explain the strong dependence of E_a for CO stripping on the CO adsorption potential [273]. It could also support, at least qualitatively, higher oxidation rates in alkaline than acidic solutions, and on stepped surfaces. For the OH-H$_2$O interaction on Pt(111), two different OH$_{ads}$ coverage regimes have been suggested: up to ⅓ ML, and above ⅓ ML [211]. Their origin is two-fold: OH-H$_2$O interaction is stronger than both OH-OH and H$_2$O-H$_2$O interactions, and hydrogen scrambling in these overlayers is very facile, *i.e.* the relaxation time for finding the most stable overlayer is fast. In alkaline solutions, weakening of the water/OH network, because of higher OH$_{ads}$ coverages, in turn could change "*effective*" interactions inside the adlayer from an attractive to a slightly repulsive character. For stepped surfaces, it is well know that defects and steps disturb the OH-H$_2$O network [232–234].

Hence, it could make "*effective*" interactions less attractive, especially for the more stepped surfaces, and affect the CO_{ads} packing density, as suggested from experiments [112,193,248,253,274]. Anyway, in these cases, the role of active sites for the reaction still remains, *i.e.* preferential surface sites where OH adsorption begins.

It is worth to mention that, in this work, rate constants for OH adsorption/desorption were chosen in such a way that at 20 mV s^{-1} OH_{ads} adsorption appears quite reversible; but at the same time, they have been kept deliberately low in order to avoid long simulation times, which may result from having very fast and very slow reactions in the same model. Higher OH_{ads} adsorption/desorption rate constants, as expected on Pt(111), will lead to sharper $E_{p,CO/OH}$ at moderate CO oxidation rates. In this case, even repulsive interactions can lead to sharp $E_{p,CO/OH}$, although its position would be shifted to lower potentials before OH_{ads} adsorption takes place. Additionally, as can be appreciated from Figs. 5–4 and 5–10, under simulated conditions $E_{p,CO/OH}$ may appear even at potentials as low as 0.2 V below the beginning of OH adsorption. Therefore, OH adsorption on stepped surfaces does not necessarily have to occur in the hydrogen adsorption/desorption region as suggested before [275].

Similarly, as discussed previously [167], experimental results on Rh(111) and its vicinal surfaces Rh[*n*(111)x(111)] could be also explained in light of repulsive interactions, especially in absence of CO diffusion. Features as tailings, pre and post-shoulders on voltammetric peaks [247,248], together with symmetric current transients that become slightly asymmetric at lower potentials, with a tailing in its descending part, and even the high amount of CO_{ads} remaining after a potential step at low E_f on sulfuric acid [248,249], can be observed from Figs. 5–9, 5–10, 5–11 and 5–12. In this case, "*effective*" repulsive interactions are expected, taking into account that average attractive CO-H_2O interactions have been reported [120]. Of course, this is not the whole picture, and other important phenomena also play an important role. However, results here, and from previous work [167], highlight the importance of "*effective*" interactions in the reaction kinetics and suggest that they should be taken into account when interpreting experimental data.

Finally, some words should be said regarding the role of surface diffusion on the CO electro-oxidation on Rh surfaces. Experimentally, less tailing of the main peak in perchloric than in sulphuric solutions, when comparing voltammetric and chronoamperometric data, has been interpreted as a higher CO_{ads} mobility in the former solution [248,249]. In contrast, DMC transients when $k_2 = 8.234 \times 10^{-2}$ s^{-1} and $\epsilon_{CO\text{-}CO} = 0.1$ eV evidence that those results could also be explained considering the role of OH_{ads} diffusion. For potentiostatic experiences, if $D_{CO} = 0$ and $E_f = 0.5$ V, transients have a more pronounced tailing if $D_{OH} = 0$ than if $D_{OH} = 100$ (Fig. 5–12B), and for $D_{CO} = 100$ and $E_f = 0.15$ V, transients have a more pronounced tailing if $D_{OH} = 0$ than if $D_{OH} = 10000$ (Fig. 5–12D). More experimental efforts are necessary to clarify this point.

5.4 Conclusions

In this paper, a lattice-gas modeling of the electrochemical CO oxidation through a LH scheme including "*effective*" lateral interactions between one of the adsorbates has been solved. The main aim was to underscore the importance of considering the molecular distribution of the reaction partners and their surface mobility. For this purpose, two methods: MFA and DMC simulations have been compared. In the MFA approach, average lateral interactions, which depend of the adsorbate coverages, are used.

Contrary, DMC simulation treats the distribution of the adsorbed species in an essentially exact way (provided a sufficiently large lattice is chosen), but requires a substantial amount of computer time to simulate high surface diffusion rates or strong lateral interaction.

For low CO oxidation reaction rates, repulsive interactions between CO_{ads} species may lead to multiple peaks in the voltammetry, especially if CO_{ads} mobility is high. These peaks are consequence of the existence of high and low packing CO_{ads} density domains inside the adlayer, each one of them having different "*effective*" CO_{ads} reaction rates. In this case, MFA approach only predicts one main oxidation peak either with a shoulder or an asymmetrical tail at its positive potential side.

Additionally, simulations show that some experimental results from the electrochemical CO_{ads} oxidation on various surface planes of Pt or Rh on acidic medium, by cyclic voltammetric and/or potential step chronoamperometric measurements, may actually be connected, not with low CO_{ads} surface mobility or a change in the kinetics mechanism, but rather they may be consequence of "*effective*" lateral adsorbate-adsorbate interactions between the species accompanied, or not, by island formation and rapid adsorbate diffusion. Similarly, on alkaline medium CO_{ads} oxidation on Pt(111) and its vicinal surfaces may be better described considering an increase in the inter-particle/intra-particle balance and low CO_{ads} diffusion. In particular, values of lateral interactions on different planes may be slightly different and could depend to some extent on potential. Simultaneously, the size of islands may depend on the way how the adsorbed overlayer is prepared and on the reaction conditions. All these factors may influence the overall reaction kinetics.

In summary, employing DMCS has been shown that including lateral interactions into the LH mechanism can reconcile different experimental results. In addition, results extend the conceptual framework for interpreting transient kinetics of CO_{ads} oxidation on Pt, and in general on metallic surfaces. In spite of the high level of simplicity, the model holds great promise in the understanding of electrocatalytic activity. However, the structural features of the real system are much more complex and it is necessary to continue refining the model.

6. Final Remarks

As discussed along this thesis, modified electrodes are a promising technology in electrode systems, with multiple and widespread applications in electrochemistry, such as chemical sensing, energy conversion and storage, and electrochromic displays. The interest in these systems arises both from the fundamental point of view of basic science, and because they are a central component in many electrochemical devices, in which a thin film covers the electrode surface. In any of these applications, a deep understanding of the structure and properties of the interfacial double layer is needed. However, the study of these systems is complex, and experimental techniques for examining the structure of these layers at molecular level are not available. In consequence, theoretical approaches are essential in order to progress in the comprehension of phenomena occurring at these electrified interfaces.

Within this idea, the main objective of this thesis was to give a contribution, from a fundamental basis, to the detailed knowledge of both the structure and properties of the electrical double layer and the charge transfer processes at electrode/membrane interfaces. With the hope that this information will help to improve our current understanding of the phenomena taking place on these interfaces and define the right approach toward an optimal catalyst utilization, advanced design and higher performance of these thin solid state devices and particularly in the case of Proton Exchange Fuel Cells (PEFCs).

In the first part of this thesis (Chapter 1), Nafion® coated Pt(111) electrodes were prepared and studied by cyclic voltammetry and *In situ* InfraRed Reflection Absorption Spectroscopy (IRRAS). The structure and properties of the electrical double layer in non-adsorbing electrolytes and some charge transfer processes, such as hydrogen adsorption/desorption, water dissociation and CO oxidation, were evaluated. Results shown a strong interaction between Pt(111) and Nafion® membrane, giving rise to a preferential orientation, electric field driven, of polymer molecular units, and the water inside the membrane, close to the electrode surface. Apparently, the membrane introduces a new charge transfer process, *pH*-dependent, around 0.50 V in the cyclic voltammogram (CV), compared to the bare electrode. However, the lack of a wavenumber blue-shift of both protonated and dissociated Nafion®'s sulfonic groups with increasing the electrode potential would suggest that sulfonate anions are not specifically adsorbed but populated in the double layer. A sudden change of system optical properties at the Pt(111)/membrane interface occurs at 0.9 V, which could be possibly due to clustering within the polymer.

Regarding the charge transfer, it is found that the hydrogen and OH adsorption/desorption regions are significantly blocked, probably because a fraction of the Pt(111) surface is covered by hydrophobic PTFE backbone and becomes electrochemically inactive. In contrast, CO stripping experiments revealed a modification on the CO-adlayer structure,

with only on–top adsorption and a higher wavenumber band that continuously increases with the potential, even during CO oxidation. In addition, the presence of the Nafion® film slows down the CO oxidation reaction, which occurs in a sharper peak, and shifted to higher potential values, than on bare Pt(111) electrodes. Apparently, the presence of the membrane promotes surface segregation of hydrophilic and hydrophobic molecules into surface islands.

Chapters 2 and 3 were devoted to develop an electrostatic model for the interface of solid polymer electrolyte (SPE) coated electrodes, in contact with a non-adsorbing electrolyte solution. The model considered the different mobility of the charge-carrier species inside the membrane, and includes a thermodynamic description of the acid/base chemical dissociation equilibrium of ionic polymer groups. Simulations showed a differential capacitance (C_T), as a function of the applied potential (E), depending on different factors, such as the dielectric and geometrical interface characteristics and membrane and solution properties. The model reproduces results from both the Mott-Schottky theory, for charge transfer near a semiconductor/metal interface, and the Gouy-Chapman-Stern model as limiting cases. Between these two limits, local maxima (or minima) in the C_T–E profiles may appear as consequence of the dissociation of the acid/base molecular species and differences in ions' mobility, although the film is localized at the Outer Helmholtz Plane.

When including coion membrane permeation and ion solvation energetic inside the membrane (Chapter 3), the model is able to reproduce experimental sharp peaks, close to the potential of zero charge (PZC), in the cyclic voltammogram reported for Nafion® coated single crystal electrodes. Capacitance maxima in C_T–E curves may appear not only due to the membrane acid/base dissociation process, but also because of the change with the applied potential in the total interaction energy that ions face when moving from the favorable, high dielectric, aqueous medium to the unfavorable, low dielectric, membrane environment. A low dielectric constant inside membrane pores, ε_P, can produce sharp peaks, which broaden, decrease in magnitude and shift to more positive potentials when increasing ε_P. These peaks can be even sharper if the capacitance at the Inner Helmholtz Plane, C_{IHP}, is large.

The most important conclusions of the three first chapters are:

- Capacitance maxima in C_T–E curves can also occur because of the membrane acid/base dissociation process or the change in the total interaction energy of charge-carriers, and not only due to the specific adsorption of membrane ionic units on the electrode surface.

- The structure of the polymer electrolyte close to the surface is different than that in the bulk and changes with the applied potential. In particular, this latter has a direct effect on ionic polymer units, *i.e.* the structure and size of the hydrophilic ion cluster region of the membrane.

- Considering the long time needed to reach a membrane structure in equilibrium (>20 min), differences between reported CVs under similar working conditions, may arrive due to quasi-irreversible, far from equilibrium, metastable states of Nafion films close to the interface, with a low hydration level induced or not by the electrode potential. The final structure of an ionomer membrane will depend on the method by which it is prepared and other applied procedures before taking the electrochemical measurements.

- In general, the presence of the membrane close to the electrode surface may inhibit the electron transfer rate (ETR) of electrochemical reactions (ECR) that strongly depend on the structure of the electrical double layer, either because it blocks some surface sites or because of the higher absolute value of the potential at the Outer Helmholtz Plane, ϕ_{OHP}. However, in some cases, the ETR can be enhanced.

- It is possible to improve the overall performance of catalytic layers of thin layer devices by a careful design, considering the membrane thickness and specific membrane characteristics according to the nature of reacting species.

The second part of this thesis was dedicated to indirectly study the effect of the membrane on the electron transfer rate of surface reactions of adsorbed species, as the electrochemical CO oxidation. In this sense, a Langmuir–Hinshelwood (LH) mechanism for the oxidation of pre-adsorbed CO by adsorbed OH coming from water dissociation, including "*effective*" lateral interactions between CO/CO molecules, was proposed. The model was solved by both the Mean Field Approximation (MFA) (Chapter 4) and Dynamic Monte Carlo (DMC) simulations (Chapter 5), in order to analyze the influence of island formation, adsorbate-adsorbate correlations and surface diffusion on the reaction kinetics and the electrochemical response, all these phenomena affected by the membrane's two-phase nature close to the electrode surface.

When "*effective*" attractive interactions between CO–CO molecules is considered, stripping voltammograms (SVs) usually contain highly asymmetric and sharp peaks, with a steep rise and an abrupt descend once j_{max}, at $E_{p,CO/OH}$ or t_{max}, is reached (Chapter 4). In this case, simulated curves increasing the magnitude of interactions are similar to the experimental curves obtained for bare and Nafion® covered Pt(111) electrodes. Hence, it is highly possible that Nafion® membrane modifies the "*effective*" interactions between CO_{ads}–CO_{ads}, CO_{ads}–OH_{ads} and OH_{ads}–OH_{ads} molecules inside the CO adlayer over Pt(111), making them more "attractive" than in the case of a bare electrode. Differences in physical properties of adsorbed molecules could give rise to these "*effective*" interactions, *i.e.* while H_2O_{ads}/OH_{ads} molecules form a stable network due to their attractive interactions, CO_{ads}–CO_{ads} and CO_{ads}–H_2O_{ads} interactions are repulsive.

On the other hand, similar to surface diffusion limitations, "*effective*" repulsive interactions between CO–CO molecules may produce tailing and shoulders in the main oxidation peak, or even multiple peaks, in SVs, especially if the difference between the CO rate constant and ϵ_{CO-CO} values is large enough, and CO_{ads} mobility is fast. These peaks are due to the existence of high and low packing CO_{ads} density domains inside the adlayer, each one of them with an "effective" CO_{ads} reaction rate. In order to differentiate merely diffusion limitations from "*effective*" repulsive interactions, a scan rate study could be performed. At low scan rates (v), latter effects are more pronounced, and the SV should exhibit an increasing tailing or the appearance of shoulders, or peaks, in the positive side of the main peak. Instead, under only diffusional effects, the SV should display pre-shoulders, or peaks, at slow v and single, wider peaks at faster v.

Simulations show that experimental results in current transients and CVs, observed on various surface planes of Pt or Rh and their vicinal surfaces in acidic medium, may actually be related, not only to diffusional effects, changes in the rate determining step or the reaction mechanism, but rather with specific features of the reaction kinetics, including, or not, a change in the "*effective*" adsorbate-adsorbate interactions inside the adlayer. Indeed, island formation is not only explained by low CO_{ads} surface mobility and a nucleation and growth (N&G) mechanism. It can also be explained by "effective" attractive

adsorbate–adsorbate interactions and rapid adsorbate diffusion. Of course, this is not the whole picture, and other important phenomena also play an important role. However, the results here highlight the importance of "*effective*" interactions in reaction kinetics and suggest that they should be taken into account when interpreting experimental data.

As final remark, it is important to stress once more the complexity of the studied system. The structure and properties of the electrical double layer, as well as the electrochemical response of charge transfer processes at metal/SPE interfaces depends on many factors such as the specific membrane properties, geometrical characteristics, chemical nature of reactant and product species, reaction mechanism, reaction kinetics and, in the case of surface reactions, "*effective*" adsorbate-adsorbate interactions inside the adlayer, among others. However, the findings of this research will certainly help to a better understanding of these phenomena.

References

1. Bard, A. J.; Faulkner, L. R. *Electrochemical Methods*, 2nd ed.; Wiley: New York, **2001**.
2. Tagliazucchi, M.; Calvo, E. J.; Szleifer I. *Langmuir* **2008**, *24*, 2869–2877.
3. Netz, R. R.; Andelman, D. In *Encyclopedia of Electrochemistry Vol. I*; Urbakh, M.; Giladi, E., Eds. Wiley–VCH: Weinheim, 2002; pp 282–322.
4. Dautzenberg, H.; Jaeger, W.; Kötz, B. P. J.; Seidel, C.; Stscherbina, D. *Polyelectrolytes: Formation, characterization and application*; Hanser Publishers: Munich, **1994**.
5. Carrette, L.; Friderich, K. A.; Stimming, U. *Fuel Cells* **2001**, *1*, 5–39.
6. Eikerling, M.; Kornyshev, A.; Kulikovsky, A. *The Fuel Cell Review* **2005**, *1*, 15–24.
7. Liu, J.; Selvan, M. E.; Cui, S.; Edwards, B. J.; Keffer, D. J.; Steele, W. V. *J. Phys. Chem. C* **2008**, *112*, 1985–1993.
8. Kreuer. K.D. *J. Membr. Sci.* **2001**, *185*, 29–39.
9. Modestino, M. A.; Paul, D. K.; Dishari, S.; Petrina, S. A.; Allen, F. I.; Hickner, M. A.; Karan, K.; Segalman, R. A.; Weber, A. Z. *Macromolecules* **2013**, *46*, 867−873.
10. Njau, K. N.; Woude, M.; Visser, G. J.; Janssen, L. J. J. *Chem. Ing. J.* **2001**, *79*, 187–195.
11. Ugo, P.; Cavalieri, F.; Rudello, D.; Moretto, L. M.; Argese, E. *Sensors* **2001**, *1*, 102–113.
12. Daud, N.; Yusof, N. A.; Tee, T. W.; Abdullah, A. H. *J. Electrochem. Sci.* **2012**, *7*, 175–185.
13. Opekar F.; Stulık, K. *Anal. Chim. Acta* **1999**, *385*, 151–162.
14. Yarusso, D. J.; Cooper, S. L. *Macromolecules* **1983**, *16*, 1871–1880.
15. Bandini, S.; Vezzani, D. *Chem. Eng. Sci.* **2003**, *58*, 3303–3326.
16. Bowen, W. R.; Welfoot, J. S. *Chem. Eng. Sci.* **2002**, *57*, 1121–1137.
17. Heitner-Wirguin, C. *J. Membr. Sci.* **1996**, *120*, 1–33.
18. Mauritz, K. A.; Moore, R. B. *Chem. Rev.* **2004**, *104*, 4535–4586.
19. Perry, M. I.; Fuller, T. F. *J. Electrochem. Soc.* **2002**, *149*, S59–S67.
20. Ayato, Y.; Kunimatsu, K.; Osawa, M.; Okada, T. *J. Electrochem. Soc.* **2006**, *153*, A203–A209.
21. Kanamura, K.; Morikawa, H.; Umegaki, T. *J. Electrochem. Soc.* **2003**, *150*, A193–A195.
22. Zeng, J.; Jean, D.-Im.; Ji, C.; Zou, S. *Langmuir* **2012**, *28*, 957–964.
23. Masuda, T.; Ikeda, K.; Uosaki, K. *Langmuir* **2013**, *29*, 2420−2426.
24. Wescott, J. T.; Qi, Y.; Subramanian, L.; Capehart, T. W. *J. Chem. Phys.* **2006**, *124*, 134702-1–134702-5.
25. Maruyama, J.; Inaba, M.; Katakura, K.; Ogumi, Z.; Takehara, Z. *J. Electroanal. Chem.* **1998**, *447*, 201–209.
26. Jiang, J.; Kucernak, A. *J. Electroanal. Chem.* **2004**, *567*, 123–137.
27. Jiang, J.; Kucernak, A. *J. Electroanal. Chem.* **2005**, *576*, 223–236.
28. Chu, Y.; Shul, Y. G.; Choi, W. C.; Woo, S. I.; Han, H. *J. Power Source* **2003**, *118*, 334–341.

29. Tu, W-.Y.; Liu, W-.J.; Cha, C-.S.; Wu, B-.L. *Electrochim. Acta* **1998**, *43*, 3731–3739.
30. Miyatake, K.; Omata, T.; Tryk, D. A.; Uchida, H.; Watanabe, M. *J. Phys. Chem. C* **2009**, *113*, 7772–7778.
31. Lawson, D. R.; Whiteley, L. D.; Martin, C. R.; Szentirmay, M. N.; Song, J. I. *J. Electrochem. Soc.* **1988**, *135*, 2247–2250.
32. Gottesfeld, S.; Raistrick, I. D.; Srinivasan, S. *J. Electrochem. Soc.* **1987**, *134*, 1455–1459.
33. Floriano, J. B.; Ticianelli, E. A.; Gonzalez, E. R. *J. Electroanal. Chem.* **1994**, *367*, 157–160.
34. Ayad, A.; Naimi, Y.; Bouet, J.; Fauvarque, J. F. *J. Power Source* **2004**, *130*, 50–55.
35. Zecevic, S. K.; Wainright, J. S.; Litt, M. H.; Gojkovic, S. J.; Savinell, R. F. *J. Electrochem. Soc.* **1997**, *144*, 2973–2982.
36. Yano, H.; Higuchi, E.; Uchida, H.; Watanabe, M. *J. Phys. Chem. B* **2006**, *110*, 16544–16549.
37. Ohma, A.; Fushinobu, K.; Okazaki, K. *Electrochim. Acta* **2010**, *55*, 8829–8838.
38. Osawa, M.; Nakane, T.; Ito, K.; Suetaka, W. *J. Electroanal. Chem.* **1989**, *270*, 459–464.
39. Malevich, D.; Li, J.; Chung, M. K.; McLaughlin, C.; Schlaf, M.; Lipkowski, J. *J. Solid State Electrochem.* **2005**, *9*, 267–276.
40. Wood III, D. L.; Chlistunoff, J.; Majewski, J.; Borup, R. L. *J. Am. Chem. Soc.* **2009**, *131*, 18096–18104.
41. Uribe, F. A.; Springer, T. E.; Gottesfeld, S. *J. Electrochem. Soc.* **1992**, *139*, 765–773.
42. Chlistunoff, J.; Uribe, F.; Pivovar, B. *ECS Trans.* **2006**, *1*, 137–146
43. Chlistunoff, J.; Uribe, F.; Pivovar, B. *ECS Trans.* **2007**, *2*, 37–46.
44. Itskovich, E. M.; Kornyshev, A. A.; Vorotyntsev, M. A. *Phys. Status Solidi A* **1977**, *39*, 229–238.
45. Kornyshev, A. A.; Vorotyntsev, M. A. *Electrochim. Acta* **1978**, *23*, 267–270.
46. Kornyshev A. A.; Vorotyntsev, M. A. *Electrochim. Acta* **1981**, *26*, 303–323.
47. Biesheuvel, P. M.; Franco, A. A.; Bazant, M. Z. *J. Electrochem. Soc.* **2009**, *156*, B225–B233.
48. Franco, A. A.; Schott, P.; Jallut, C.; Maschke, B. *Fuel Cells* **2007**, *7*, 99–117.
49. Franco, A. A.; Schott, P.; Jallut, C.; Maschke, B. *J. Electrochem. Soc.* **2006**, *153*, A1053–A1061.
50. Bonnefont, A.; Argoul, F.; Bazant, M. Z. *J. Electroanal. Chem.* **2001**, *500*, 52–61.
51. Bazant, M. Z.; Chu, K. T.; Bayly, B. J. *SIAM J. Appl. Math.* **2005**, *65*, 1463–1484.
52. Chu, K. T.; Bazant, M. Z. *SIAM J. Appl. Math.* **2005**, *65*, 1485–1505.
53. Markovic, N.; Gasteiger, H.; Ross, P. N. *J. Electrochem. Soc.* **1997**, *144*, 1591–1597.
54. Gancs, L.; Kobayashi, T.; Debe, M. K.; Atanasoski, R.; Wieckowski, A. *Chem. Mater.* **2008**, *20*, 2444–2454.
55. Saha, M. S.; Gulla, A. F.; Allen, R. J.; Mukerjee, S. *Electrochim. Acta* **2006**, *51*, 4680–4692.
56. Solla–Gullón, J.; Vidal–Iglesias, F. J.; Feliu, J. M. *Annu. Rep. Prog. Chem. Sect. C* **2011**, *107*, 263–297.
57. Sánchez–Sánchez, C. M.; Solla–Gullón, J.; Vidal–Iglesias, F. J.; Aldaz, A.; Montiel, V.; Herrero, E. *J. Am. Chem. Soc.* **2010**, *132*, 5622–5624.
58. Kinoshita, K. *J. Electrochem. Soc.* **1990**, *137*, 845–848.
59. Greeley, J.; Rossmeisl, J.; Hellman, A.; Nørskov, J. K. *Z. Phys. Chem.* **2007**, *221*, 1209–1220.

60. Honig, B. H.; Hubbell, W. L.; Flewelling, R. F. *Ann. Rev. Biophys. Biophys. Chem.* **1986**, *15*, 163–193.
61. Szymczyk, A.; Fievet, P. *J. Membr. Sci.* **2005**, *252*, 77–88.
62. Szymczyk, A.; Fatin-Rouge, N.; Fievet, P.; Ramseyer, C.; Vidonne, A. *J. Membr. Sci.* **2007**, *287*, 102–110.
63. Yaroshchuk, A. E. *Adv. Colloid Interface Sci.* **2000**, *85*, 193–230.
64. Yaroshchuk, A. E. *Sep. Purif. Technol.* **2001**, *22/23*, 143–158.
65. Subbaraman, R.; Strmcnik, D.; Stamenkovic, V.; Markovic, N. *J. Phys. Chem. C* **2010**, *114*, 8414–8419.
66. Subbaraman, R.; Strmcnik, D.; Paulikas, A. P.; Stamenkovic, V.; Markovic, N. *Chem. Phys. Chem.* **2010**, *11*, 2825–2833.
67. Gómez–Marín, A. M.; Berná, A.; Feliu, J. M. *J. Phys. Chem. C **2010**,* 114, 20130–20140.
68. Ahmed, M.; Morgan, D.; Attard, G. A.; Wright, E.; Thompsett, D.; Sharman, J. *J. Phys. Chem. C* **2011**, *115*, 17020–17027.
69. Ahmed, M.; Attard, G. A.; Wright, E.; Sharman, J. *Cat. Today* **2013**, *202*, 128–134.
70. Sonsudin, F.; Masuda, T.; Ikeda, K.; Naohara, H.; Uosaki, K. *Chem. Lett.* **2010**, *39*, 286–287.
71. Gilman, S. *J. Phys. Chem.* **1964**, *68*, 70–80.
72. Koper, M. T. M.; Jansen, A. P. J.; Van Santen, R. A. Lukkien, J. J.; Hilbers, P. A. J. *J. Chem. Phys.* **1998**, *109*, 6051–6062.
73. Hill, T. L. *An Introduction to Statistical Thermodynamics*; Dover, New York, U.S.A., **1960**.
74. Jansen, A.P.J. *Comput. Phys. Commun.* **1995**, *86*, 1–12.
75. Lukkien, J. J.; Segers, J. P. L.; Hilbers, P. A. J.; Gelten, R. J.; Jansen, A. P. J. *Phys. Rev. E* **1998**, *58*, 2598–2610.
76. CARLOS website: http://www.win.tue.nl/~johanl/projects/Carlos/ and http://www.win.tue.nl/~johanl/projects/nCarlos/. Last visit: 24th of May 2013.
77. Zhdanov, V. P.; Kasemo, B. *Electrochem. Commun.* **2006**, *8*, 561–564.
78. Malevich, D.; Zamlynny, V.; Sun, S. G.; Lipkowski, J. *Z. Phys. Chem.* **2003**, *217*, 513–525.
79. Broka, K.; Ekdunge, P. *J. Appl. Electrochem.* **1997**, *27*, 117–123.
80. Buzzoni, R.; Bordiga, S.; Ricchiardi, G.; Spoto, G.; Zecchina, A. *J. Phys. Chem.* **1995**, *99*, 11937–11951.
81. Ludvigsson, M.; Lindgren, J.; Tegenfeldt, J. *Electrochim. Acta* **2000**, *45*, 2267–2271.
82. Gruger, A.; Régis, A.; Schmatko, T.; Colomban, P. *Vib. Spec.* **2001**, *26*, 215–225.
83. Liang, Z.; Chen, W.; Liu, J.; Wang, S.; Zhou, Z.; Li, W.; Sun, G.; Xin, Q. *J. Membr. Sci.* **2004**, *233*, 39–44.
84. Basnayake, R.; Peterson, G. R.; Casadonte, D. J.; Korzeniewski, C. *J. Phys. Chem. B* **2006**, *110*, 23938–23943.
85. Basnayake, R.; Wever, W.; Korzeniewski, C. *Electrochim. Acta* **2007**, *53*, 1259–1264.
86. Korzeniewski, C.; Adams, E.; Liu, D. *Appl. Spec.* **2008**, *62*, 634–639.
87. Byun, C. K.; Sharif, I.; DesMarteau, D. D.; Creager, S. E.; Korzeniewski, C. *J. Phys. Chem. B* **2009**, *113*, 6299–6304.
88. Idupulapati, N.; Devanathan, R.; Dupuis, M. *J. Phys. Chem.* A **2010**, *114*, 6904–6912.
89. Webber, M.; Dimakis, N.; Kumari, D.; Fuccillo, M.; Smotkin, E. S. *Macromolecules* **2010**, *43*, 5500–5502.
90. Warren, D. S.; McQuillan, A. J. *J. Phys. Chem*. B **2008**, *112*, 10535–10543.
91. Iwasita, T.; Nart, F. C. *Prog. Surf. Sci.* **1997**, *55*, 271–340.
92. Iwasita, T.; Rodes, A.; Pastor, E. *J. Electroanal. Chem.* **1995**, *383*, 181–189.

93. Orts, J. M.; Louis, E.; Sander, L. M.; Feliu, J. M.; Aldaz, A.; Clavilier. J. *Surf. Sci.* **1998**, *416*, 371–383.

94. Clavilier, J.; Armand, D.; Sun, S. G.; Petit, M. *J. Electroanal. Chem.* **1986**, *205*, 267–272.

95. Berná, A.; Kuzume, A.; Herrero, E.; Feliu, J. M. *Surf. Sci.* **2008**, *602*, 84–89.

96. Berná, A.; Feliu, J. M.; Gancs, L.; Mukerjee, S. *Electrochem. Commun.* **2008**, *10*, 1695–1699.

97. Berná, A.; Climent, V.; Feliu, J. M. *Electrochem. Commun.* **2007**, *9*, 2789–2794.

98. Naegeli, R.; Redepenning, J.; Anson, F. C. *J. Phys. Chem.*, **1986**, *90*, 6227–6232.

99. Elliott, C. M.; Redepenning, G. G. *J. Electroanal. Chem.* **1984**, *181*, 137–152.

100. Ferry, L. *J. Macromol. Sci. Part A: Pure Appl. Chem.* **1990**, *27*, 1095–1107.

101. Allahyarov, E.; Taylor, P. L. *Phys. Rev. E* **2009**, *80*, 020801-1–020801-5.

102. Allahyarov, E.; Taylor, P. L.; Löwen, H. *Phys. Rev. E* **2010**, *81*, 031805-1–031805-12.

103. Ma, C.; Zhang, L.; Mukerjee, S.; Ofer, D.; Nair, B. *J. Membr. Sci.* **2003**, *219*, 123–136.

104. Spry, D. B.; Fayer, M. D. *J. Phys. Chem. B* **2009**, *113*, 10210–10221.

105. Hensley, J. E.; Way, J. D.; Dec, S. F.; Abney, K. D. *J. Membr. Sci.* **2007**, *298*, 190–201.

106. Wang, Z-T.; Wang, Z-S.; Xu, L.; Gao, Q-J.; Wei, G-Q.; Lu, J. *J. Power Source* **2009**, *186*, 293–298.

107. Lin, H-L.; Yu, T. L.; Han, F-H. *J. Polym. Research.* **2006**, *13*, 379–385.

108. Osawa, M.; Tsushima, M.; Mogami, H.; Samjeske, G.; Yamakata, A. *J. Phys. Chem. C.* **2008**, *112*, 4248–4256.

109. Sethuraman, V. A.; Weidner, J. W.; Haug, A. T.; Motupally, S.; Protsailo, L. V. *J. Electrochem. Soc.* **2008**, *155*, B50–B57.

110. Lachenwitzer, A.; Li, N.; Lipkowski, J. *J. Electroanal. Chem.* **2002**, *532*, 85–98.

111. Chang, S. C.; Weaver, M. J. *J. Chem. Phys.* **1990**, *92*, 4582–4587.

112. Lebedeva, N. P.; Koper, M. T. M.; Herrero, E.; Feliu, J. M.; Van Santen, R. A. *J. Electroanal. Chem.* **2000**, *487*, 37–44.

113. Furuya, N.; Motoo, S.; Kunimatsu, K. *J. Electroanal. Chem.* **1988**, *239*, 347–352.

114. Kitamura, F.; Takeda, M.; Takahashi, M.; Ito, M. *Chem. Phys. Lett.* **1987**, *142*, 318–321.

115. Rodes, A.; Pastor, E.; Iwasita, T. *J. Electroanal. Chem.* **1994**, *369*, 183–188.

116. Rodes, A.; Pastor, E.; Iwasita, T. *J. Electroanal. Chem.* **1994**, *373*, 167–172.

117. Rodes, A.; Pastor, E.; Iwasita, T. *J. Electroanal. Chem.* **1994**, *377*, 215–220.

118. Tornquist, W.; Guillaume, F.; Griffin, G. L. *Langmuir* **1987**, *3*, 477–482.

119. Hung, L. H.; Wieckowski, A.; Weaver, M. J. *J. Phys. Chem.* **1988**, *92*, 6985–6990.

120. Wagner, F. T.; Moylan, T. E.; Schmieg, S. J. *Surf. Sci.* **1988**, *95*, 403–428.

121. Kucernak, A. R.; Offer, G. J. *Phys. Chem. Chem. Phys.* **2008**, *10*, 3699–3711.

122. Netz, R. R.; Andelman, D. *Phys. Rep.* **2003**, *380*, 1–95.

123. Ahn, Y.; Saha, J. K.; Schatz, G. C.; Jang, J. *J. Phys. Chem. C* **2011**, *115*, 10668–10674.

124. Tagliazucchi, M.; Calvo, E. J.; Szleifer, I. *J. Phys. Chem. C* **2008**, *112,* 458–471.

125. Goujon, F.; Bonal, C.; Limoges, B.; Malfreyt, P. *J. Phys. Chem. B* **2010**, *114*, 6447–6454.

126. Filippini, G.; Israeli, Y.; Goujon, F.; Limoges, B.; Bonal, C.; Malfreyt, P. *J. Phys. Chem. B* **2011**, *115*, 11678–11687.

127. Chidsey, C. E. D.; Murray, R. W. *J. Phys. Chem.* **1986**, *90*, 1479–1484.

128.   Bowden, E. F.; Dautartas, M. F.; Evans, J. F. *J. Electroanal. Chem. Interfacial Electrochem.* **1987**, *219*, 49–69.
129.   Posadas, D.; Florit, M. I. *J. Phys. Chem. B* **2004**, *108*, 15470–15476.
130.   Lizarraga, L.; Andrade, E. M.; Florit, M. I.; Molina, F. V. *J. Phys. Chem. B* **2005**, *109*, 18815–18821.
131.   Léger, C.; Bertrand, P. *Chem. Rev.* **2008**, *108*, 2379–2438.
132.   Redepenning, J.; Anson, F. C. *J. Phys. Chem.* **1987**, *91*, 4549–4553.
133.   Laviron, E. *J. Electroanal. Chem.* **1979**, *100*, 263–270.
134.   Andrieux, C. P.; Savéant, J. M. *J. Phys. Chem.* **1988**, *92*, 6761–6767.
135.   Anson, F. C.; Blauch, D. N.; Savéant, J.-M.; Shu, C.-F. *J. Am.Chem. Soc.* **1991**, *113*, 1922–1932.
136.   Laviron, E. *J. Electroanal. Chem* **1980**, *112*, 1–23.
137.   Schottky, W., *Z Phys.* **1939**, *113*, 367–414.
138.   Mott, N. F. *Proc. Roy. Soc. (London)* **1939**, *A171*, 27–38.
139.   Zhdanov, V. P.; Kasemo, B. *Appl. Surf. Sci.* **2003**, *219*, 256–263.
140.   Ni, M.; Leung, M. K. H.; Leung, D. Y. C. *Fuel Cells* **2007**, *7*, 269–278.
141.   Gouy, L. G. *J. Phys. Theor. Appl.* **1910**, *9*, 457–468.
142.   Chapman, D. L. *Philos. Mag.* **1913**, *25*, 475–481.
143.   Stern, O. *Z. Electrochem.* **1924**, *30*, 508–516.
144.   Armstrong, R. D.; Horrocks, B. R. *Solid State Ionics* **1997**, *94*, 181–187.
145.   Smith, C.P.; White, H.S. *Langmuir* **1993**, *9*, 1–3.
146.   White, H. S.; Peterson, J. D.; Cui, Q.; Stevenson, K. J. *J. Phys. Chem. B* **1998**, *102*, 2930–2934.
147.   Smith, C. P.; White, H. S. *Anal. Chem.* **1992**, *64,* 2398–2405.
148.   Andreu, R.; Fawcett, W. R. *J. Phys. Chem.* **1994**, *98*, 12753–12758.
149.   Fawcett, W. R.; Fedurco, M.; Kovácová, Z. *Langmuir* **1994**, *10*, 2403–2408.
150.   Creager, S.E.; Weber, K. *Langmuir* **1993**, *9*, 844–850.
151.   Rowe, G. K.; Creager, S. E. *J. Phys. Chem.* 1994, *98*, 5500–5507.
152.   Andreu R.; Calvente J. J.; Fawcett W. R.; Molero M. *Langmuir* **1997**, *13*, 5189–5196.
153.   Rosendahl, S. M.; Burgess, I. J. *Electrochim. Acta* **2008**, *53*, 6759–6767.
154.   Bryant, M.; Crooks, R. M. *Langmuir* **1993**, *9*, 385–387.
155.   Burgess, I.; Seivewright, B.; Lennox, R. B. *Langmuir* **2006**, *22*, 4420–4428.
156.   Luque, A. M.; Mulder, W. H.; Calvente, J. J.; Cuesta, A.; Andreu, R. *Anal. Chem.* **2012**, *84*, 5778–5786.
157.   Xiao–Wei C. *J. Raman Spectrosc.* **2005**, *36*, 250–256.
158.   Ohshima, H.; Ohki, S. *Biophys. J.* **1985**, *47*, 673–678.
159.   Mauro, A. *Biophys. J.* **1962**, *2*, 179–198.
160.   Wang, D.; Nap, R. J.; Lagzi, I.; Kowalczyk, B.; Han, S.; Grzybowski, B. A.; Szleifer, I. *J. Am. Chem. Soc.* **2011**, *133*, 2192–2197.
161.   Kornyshev, A. A. *J. Phys. Chem. B* **2007**, *111*, 5545–5557.
162.   Sleightholme, A. E. S.; Kucernak, A. *Electrochim. Acta* **2011**, *56*, 4396–4402.
163.   Balan, B. K.; Unni, B.; Chaudhari, H. D.; Kharul, U. K.; Kurungot, S. *J. Mater. Chem.* A **2013**, *1*, 4265–4276.
164.   Hanawa, H.; Kunimatsu, K.; Watanabe, M.; Uchida, H. *J. Phys. Chem. C* **2012**, *116*, 21401–21406.
165.   Wang, J. X.; Adzic, R. R. *J. Electroanal. Chem.* **1998**, *448*, 205–210.
166.   Frumkin, A. *Z. Phys. Chem. Abst. A* **1933**, *164*, 121–133.
167.   Gómez–Marín, A. M.; Hernández-Ortíz, J. P. Chapter 4 in this thesis.
168.   Velázquez-Palenzuela, A.; Centellas, F.; Brillas, E.; Arias, C.; Rodríguez, R. M.; Garrido, J. A.; Cabot, P. L. *Int. J. Hydrogen Energy* **2012**, *37*, 17828–17836.

169.   Gómez–Marín, A. M.; Hernández-Ortíz, J. P. Chapter 3 in this thesis.
170.   Snyder, J. F.; Ratner, M. A.; Shriver, D. F. *Solid State Ionics* **2002**, *147*, 249–257.
171.   Gómez-Marín, A. M.; Hernández–Ortíz, J. P. Chapter 2 in this thesis.
172.   Donnan, F. G. *Chem. Rev.* **1924**, *1*, 73–90.
173.   Hussain, A. A.; Nataraj, S. K.; Abashar, M. E. E.; Al-Mutaz, I. S.; Aminabhavi, T. M. *J. Membr. Sci.* **2008**, *310*, 321–336.
174.   Debye, P.; Hückel, E. *Phys. Z.* **1923**, *24*, 185–206.
175.   Bockris, J. O'M.; Reddy, A. K. N. *Modern Electrochemistry*, Vol. 1, Plenum Press, New York, **1998**.
176.   Born, M. *Z. Phys.* **1920**, *1*, 45–48.
177.   Sabaté, J.; Labanda, J.; llorens, J. *J. Membr. Sci.* **2009**, *345*, 298–304.
178.   Latimer, W.M.; Pitzer, K. S.; Slansky, C. M. *J. Chem. Phys.* **1939**, *7*, 108–111.
179.   Gómez-Marín, A. M.; Clavilier, J.; Feliu, J. M. *J. Electroanal. Chem.* **2013**, *688*, 360–370.
180.   Climent, V.; García–Araez, N.; Herrero, E.; Feliu, J. M. *Russ. J. Electrochem.* **2006**, *42*, 1145–1160.
181.   Wakisaka, M.; Suzuki, H.; Mitsui, S.; Uchida, H.; Watanabe, M. *Langmuir* **2009**, *25*, 1897–1900.
182.   Herrero, E.; Feliu, J. M.; Wieckowski, A.; Clavilier, J. *Surf. Sci.* **1995**, *325*, 131–138.
183.   Wang, J. X.; Markovic, N. M.; Adzic, R. R. *J. Phys. Chem. B* **2004**, *108*, 4127–4133.
184.   Clavilier, J.; El Achi, K.; Rodes, A. *Chem. Phys.* **1990**, *141*, 1–14.
185.   Feldberg, S. W.; Rubinstein, I. *J. Electroanal. Chem.* **1988**, *240*, 1–15.
186.   Paul, D. K.; Karan, K.; Docoslis, A.; Giorgi, J. B.; Pearce, J. *Macromolecules* **2013**, dx.doi.org/10.1021/ma4002319.
187.   Dishari, S. K.; Hickner, M. A. *Macromolecules* **2013**, *46*, 413−421.
188.   Ohira, A.; Kuroda, S.; Mohamed, H. F. M. *ECS Trans.* **2012**, *50*, 993–1001.
189.   Zhdanov, V. P.; Kasemo, B. *Surf. Sci.* **2003**, *545*, 109–121.
190.   Villegas, I.; Weaver, M. J. *J. Chem. Phys.* **1994**, *101*, 1648–1660.
191.   Love, B.; Lipkowski, J. In: *Molecular Phenomena at Electrode Surfaces Chapter 33*, In: *ACS Symposium Series No 378*. Soriaga, M. (ed), 1988; pp 484–496.
192.   Maillard, F.; Eikerling, M.; Cherstiouk, O. V.; Schreier, S.; Savinova, E.; Stimming, U. *Faraday Discuss* **2004**, *125*, 357–377.
193.   Lebedeva, N. P.; Koper, M. T. M.; Feliu, J. M.; Van Santen, R. A. *J. Phys. Chem. B* **2002**, *106*, 12938–12947.
194.   Lebedeva, N. P.; Koper, M. T. M.; Feliu, J. M.; Van Santen, R. A. *J. Electroanal. Chem.* **2002**, *524–525*, 242–251.
195.   Koper, M. T. M.; Lebedeva, N. P.; Hermse, C. G. M. *Faraday Discuss* **2002**, *121*, 301–311.
196.   Marcovic, N. M.; Ross, P. N. *Surf. Sci. Rep.* **2002**, *45*, 117–230.
197.   Pozniak, B.; Mo, Y.; Scherson, D. A. *Faraday Discuss* **2002**, *121*, 313–322.
198.   Zurawski, D.; Wasberg, M.; Wieckowksi, A. *J. Phys. Chem.* **1990**, *94*, 2076–2082.
199.   Palaikis, L.; Zurawski, D.; Hourani, M.; Wieckowski, A. *Surf. Sci.* **1988**, *199*, 183–198.
200.   Feliu, J. M.; Orts, J. M.; Femandez–Vega, A.; Aldaz, A.; Clavilier, J. *J. Electroanal. Chem. Interfacial Electrochem.* **1990**, *296*, 191–201.
201.   Cherstiouk, O. V.; Simonov, P. A.; Zaikovskii, V. I.; Savinova, E. R. *J. Electroanal. Chem.* **2003**, *554–555*, 241–251.

202. Orts, J. M.; Louis, E.; Sander, L. M.; Clavilier, J. *Electrochim. Acta* **1998**, *44*, 1221–1227.
203. Korzeniewski, C. Severson, M. W., *Spectrochim. Acta* **1995**, *51A*, 499–518.
204. Korzeniewski, C. *Crit. Rev. Anal. Chem.* **1997**, *27*, 81–102.
205. Korzeniewski, C. In: *Interfacial electrochemistry Chap 20*, Wieckowski A (ed), Dekker, New York, 1999; pp 345–352.
206. Petukhov, A. V.; Akemann, W.; Friedrich, K. A.; Stimming, U. *Surf. Sci.* **1998**, *402–404*, 182–186.
207. Bergelin, M.; Herrero, E.; Feliu, J. M.; Wasberg, M. *J. Electroanal. Chem.* **1999**, *467*, 74–84.
208. Angelucci, C. A.; Herrero, E.; Feliu, J. M. *J. Phys. Chem. C* **2010**, *114*, 14154–14163.
209. Waszczuk, P.; Lu, G.; Wieckowski, A.; Lu, C.; Rice, C.; Masel, R. I. *Electrochim. Acta* **2002**, *47*, 3637–3652.
210. Park, S.; Wasilewski, S. A.; Weaver, M. J. *Electrochim. Acta* **2002**, *47*, 3611–3620.
211. Karlberg G. S.; Wahnstrom, G. *J. Chem. Phys.* **2005**, *122*, 194705-1–194705-6.
212. Armand, D.; Rosinberg, M. L., *J. Electroanal. Chem.* **1991**, 302, 191–206.
213. Hermse, C. G. M.; Van Bavel, A. P.; Koper, M. T. M.; Lukkien, J. J.; Van Santen, R. A.; Jansen, A. P. J. *Surf. Sci.* **2004**, *572*, 247–260.
214. Garcia–Araez, N.; Lukkien, J. J.; Koper, M. T. M.; Feliu, J. M. *J. Electroanal. Chem.* **2006**, 588, 1–14.
215. Frumkin, A. N. *Z. Phys*. **1926**, *35*, 792–802.
216. Conway, B. E.; Gileadi, E. *Trans. Faraday Soc.* **1962**, *58*, 2493–2509.
217. Gileadi, E.; Conway, B. E. *J. Chem. Phys.* **1963**, *39*, 3420–3430.
218. Conway B. E.; Angerstein–Kozlowska, H. *J. Electroanal. Chem. Interfacial Electrochem.* **1980**, *113*, 63–77.
219. Zhdanov, V. P.; Kasemo, B. *J. Chem. Phys.* **1996**, *104*, 2446–2452.
220. Koper, M. T. M. *J. Electroanal. Chem.* **1998**, *450*, 189–201.
221. Mitchell, S. J.; Rikvold, P. A. *Surf. Sci.* **2001**, *471*, 125–142.
222. Koper, M.T. M. *Z. Phys. Chem.* **2003**, *217*, 547–556.
223. Petukhov, A. V. *Chem. Phys. Lett.* **1997**, *277*, 539–544.
224. Koper, M. T. M.; Jansen, A. P. J.; Lukkien, J. J. *Electrochim. Acta* **1999**, *45*, 645–651.
225. Koper, M. T. M.; Lukkien, J. J.; Jansen, A. P. J.; Van Santen, R. *J. Phys. Chem. B* **1999**, *103*, 5522–5529.
226. Saravanan, C.; Markovic, N. M.; Head–Gordon, M.; Ross, P. N. *J. Chem. Phys.* **2001**, *114*, 6404–6412.
227. Korzeniewski, C.; Kardash, D. *J. Phys. Chem. B* **2001**, *105*, 8663–8671.
228. Saravanan, C.; Koper, M. T. M.; Markovic, N. M.; Head–Gordon, M.; Ross, P. N. *Phys. Chem. Chem. Phys.* **2002**, *4*, 2660–2666.
229. Gómez–Marín, A. M.; Hernández–Ortíz, J. P. Chapter 5 in this thesis.
230. Wang, H.; Jusys, Z.; Behm, R. J.; Abruña, H. D. *J. Phys. Chem. C* **2012**, *116*, 11040−11053.
231. Urchaga, P.; Baranton, S.; Coutanceau, C.; Jerkiewicz, G. *Langmuir* ***2012****, 28*, 13094–13104.
232. Van der Niet, M. J. T. C.; Den Dunnen, A.; Juurlink, L. B. F.; Koper, M. T. M. *Angew. Chem. Int. Ed.* **2010**, *49*, 6572–6575.
233. Björling, A.; Herrero, E.; Feliu, J. M. *J. Phys. Chem. C* **2011**, *115*, 15509–15515.
234. Gómez–Marín, A. M.; Feliu, J. M. *In preparation*.
235. Conway, B.E. *Prog. Surf. Sci.* **1995**, *49*, 331–452.
236. Rosca, V.; Koper, M. T. M. *Surf. Sci.* **2005**, *584*, 258–268.

237. Weaver, M. J.; Chang, S. –C.; Leung, L. –W.; Jiang, X.; Rubel, M.; Szklarczyk, M.; Zurawski, D.; Wieckowski, A. *J. Electroanal. Chem.* **1992**, *327*, 247–260.
238. Seebauer, E. G.; Allen, C. E. *Prog. Surf. Sci.* **1995**, *49*, 265–230.
239. Barth, J. V. *Surf. Sci. Rep.* **2000**, *40*, 75–149.
240. Santos, E.; Leiva, E. P. M.; Vielstich, W. *Electrochim. Acta* **1991**, *36*, 555–561.
241. Herrero, E.; Feliu, J. M.; Blais, S.; Radovic–Hrapovic, Z.; Jerkiewicz, G. *Langmuir* **2000**, *16*, 4779–4783.
242. Spendelow, J. S.; Lu, G. Q.; Kenis, P. J. A.; Wieckowski, A. *J. Electroanal. Chem.* **2004**, *568*, 215–224.
243. Akemann, W.; Friedrich, K. A.; Stimming, U. *J. Chem. Phys.* **2000**, *113*, 6864–6874.
244. García, G.; Koper, M. T. M. *J. Am. Chem. Soc.* **2009**, *131*, 5384–5385.
245. García, G.; Koper. M. T. M. *Phys. Chem. Chem. Phys.* **2009**, *11*, 11437–11446.
246. Spendelow, J. S.; Goodpaster, J. D.; Kenis, P. J. A.; Wieckowski, A. *J. Phys. Chem. B* **2006**, *110*, 9545–9555.
247. Housmans, T. H. M.; Feliu, J. M.; Koper, M. T. M. *J. Electroanal. Chem.* **2004**, *572*, 79–91.
248. Housmans, T. H. M.; Koper, M. T. M. *Electrochem. Commun.* **2005**, *7*, 581–588.
249. Housmans, T. H. M.; Koper, M. T. M. *J. Electroanal. Chem.* **2005**, *575*, 39–51.
250. Farias, M. J. S.; Tanaka, A. A.; Tremiliosi, G.; Feliu, J. M. *Electrochem. Commun.* **2011**, *13*, 338−341.
251. Herrero, E.; Chen, Q.-S.; Hernandez, J.; Sun, S.-G.; Feliu, J. M. *Phys. Chem. Chem. Phys.* **2011**, *13*, 16762−16771.
252. Farias, M. J. S.; Herrero, E.; Feliu, J. M. *J. Phys. Chem. C* **2013**, *117*, 2903−2913.
253. Lebedeva, N. P.; Rodes, A.; Feliu, J. M.; Koper, M. T. M.; van Santen, R. A. *J. Phys. Chem. B* **2002**, *106*, 9863–9872.
254. Kobayashi, T.; Babu, P. K.; Gancs, L.; Chung, J. H.; Oldfield, E.; Wieckowski, A. *J. Am. Chem. Soc.* **2005**, *127*, 14164–14165.
255. García, G.; Koper, M. T. M. *Phys. Chem. Chem. Phys.* **2008**, *10*, 3802–3811.
256. Housmans, T. H. M.; Hermse, C. G. M.; Koper, M. T. M. *J. Electroanal. Chem.* **2007**, *607*, 69–82.
257. Kang, H. C.; Weinberg, W. H. *Chem. Rev.* **1995**, *95*, 667–676.
258. Zhdanov, V. P. *Surf. Sci. Rep.* **2002**, *45*, 231–326.
259. Liu, Da–Jiang; Evans, J. W. *Model. Simul.* **2005**, *4*, 424–446.
260. Hellman, A.; Honkala, K. *J. Chem. Phys.* **2007**, 127, 194704-1–194704-6.
261. Anderson, A. B.; Neshev, N. M. *J. Electrochem. Soc.* **2002**, *149*, E383–E388.
262. Bewick, A.; Fleischmann, M.; Thirsk, H. R. *Trans. Faraday Soc.* **1962**, *58*, 2200–2216.
263. Schmickler, W. *Interfacial Electrochemistry*; Oxford University Press: New York, **1996**.
264. Avrami, M. *J. Chem. Phys.* **1939**, *7*, 1103–1112.
265. Avrami, M. *J. Chem. Phys.* **1940**, *8*, 212–224.
266. Avrami, M. *J. Chem. Phys.* **1941**, *9*, 177–184.
267. Zhu, Y.; Uchida, H.; Watanabe, M. *Langmuir* **1999**, *15*, 8757–8764.
268. Frank, S.; Roberts, D. E.; Rikvold, P. A. *J. Chem. Phys.* **2005**, *122*, 064705-1–064705-11.
269. Frank, S.; Rikvold, P. A. *Surf. Sci.* **2006**, *600*, 2470–2487.
270. Gohda, Y.; Schnur, S.; Groß, A. *Faraday Discuss.* **2008**, *140*, 233–244.
271. Petrova, N. V.; Yakovkin, I. N. *Surf. Sci.* **2002**, *519*, 90–100.

272.   Yan, Y.-G.; Yang, Y.-Y.; Peng, B.; Malkhandi, S.; Bund, A.; Stimming, U.; Cai, W.-B. *J. Phys. Chem. C* **2011**, *115*, 16378–16388.

273.   Rincón, A.; Pérez, M. C.; Cuesta, A.; Gutiérrez, C. *Electrochem. Commun.* **2005**, *7*, 1027−1032.

274.   Lebedeva, N. P; Koper, M. T. M.; Feliu, J. M.; van Santen, R. A. *Electrochem. Commun.* **2000**, *2*, 487–490.

275.   Van der Niet, M.J.T.C.; Garcia-Araez, N.; Hernandez, J.; Feliu, J. M.; Koper, M. T. M. *Cat. Today* **2013**, *202*, 105–113.